High Intensity Ultrasound Processing of AlNi (50 wt.% Ni) Particles for Electrocatalytic Water Splitting

---

DISSERTATION

zur Erlangung des akademischen Grades eines Doktors der

Naturwissenschaften (Dr. Rer. Nat.) in der Fakultät für Biologie,

Chemie und Geowissenschaften der Universität Bayreuth

vorgelegt von

Pavel V. Cherepanov

geboren in Engels

Bayreuth, 2015

This doctoral thesis was prepared at the department of Physical Chemistry II at the University of Bayreuth within the time period of January 2012 to June 2015 under supervision of Dr. Daria Andreeva-Bäumler.

This is the full reprint of the dissertation submitted to obtain the academic degree of Doctor of Natural Sciences (Dr. rer. nat.) and approved by the Faculty of Biology, Chemistry, and Geosciences of the University of Bayreuth.

Date of Submission: 29th June 2015

Date of Defense: 23rd October 2015

Acting Dean: Prof. Dr. Stefan Schuster

Doctoral Committee:

Dr. Daria Andreeva-Bäumler   (1st Reviewer)

Prof. Dr. Rhett Kempe   (2nd Reviewer)

Prof. Dr. Jürgen Senker   (Chairman)

Prof. Dr. Mukundan Thelakkat

"Поехали!"

Юрий Гагарин на старте Восток-1, первого в истории человечеста

космического корабля с человеком на борту

Космодром Байконур, СССР

12 апреля 1961

"נסענו!", *"Lass uns gehen!"*, *"Let's go!"*

Uttered by Yuri Gagarin during the launch of Vostok-1, the first in the history

of mankind spacecraft with a human onboard

Baikonur Cosmodrome, USSR

12 April 1961

Table of Contents

Summary

The present thesis is focused on the processing of metal alloy particles with ultrasound of high intensity (HIUS) for potential application in electrocatalytic water splitting process for hydrogen generation. During ultrasonic treatment of metal particles the changes in bulk (crystallite size, microstrain) and surface (composition, morphology) properties were monitored in order to unravel the fundamental aspects of acoustic cavitation and their effect on sonicated matter as well as to explain the enhancement of electrocatalytic performance of the initially inactive metal alloy catalysts.

Through the appropriate choice of sonication medium, concentration of sonicated particles suspension, and duration of the ultrasonic treatment it became possible to provide insights into the phenomenon of cavitation and associated physical (energy transfer, thermal impact, solid state atomic diffusion) and chemical (phase transformations, red-ox reaction) processes. As a result, by adjusting the ultrasound treatment conditions an AlNi based electrocatalyst with significantly improved properties (reduced overpotential, higher current output) toward hydrogen evolution reaction (HER) was fabricated.

A novel method for quantitative evaluation of energy transfer between collapsing cavitation bubbles and sonicated matter was developed. The method is based on analysis of crystallographic material parameters using powder X-ray diffraction technique. Upon monitoring of the crystallite sizes of Al_3Ni and Al_3Ni_2 intermetallic phases present in the alloy using the Scherrer and Williamson–Hall methods, it was revealed that a temperature gradient that propagates in sonicated metal particles, triggers atomic diffusion and leads to an increase in crystallites' sizes and reduction of microstrain in the system.

The method proposed here for the evaluation of the impact of cavitation on solids was applied for the estimation of the average minimum temperature ($\bar{T}_{particle}^{min}$) up to which the particle can be heated. The cavitation induced temperature gradient strongly depends on physical properties of the sonication medium such as vapor pressure and viscosity and increases in the row ethylene glycol < ethanol < water < decane. Furthermore, based on the obtained data it was estimated that the energy transfer from collapsing cavitation bubble to sonicated particle is ~ 17 % more efficient in decane than in ethylene glycol.

Simultaneously with solid state atomic diffusion in metal bulk, thermal, mechanical, and chemical impact of cavitation bubbles on the metal surface triggers the phase transformation reactions in a nm-thick interfacial layer. In collaboration with Prof. Dr. Juergen Senker from the department of Inorganic Chemistry III at the University of Bayreuth using ^{27}Al solid state NMR it has been demonstrated that even though the formation of the Al_3Ni_2 phase on the surface of AlNi alloys is kinetically restricted, collapsing cavitation bubbles heat the surface above 1124 K, triggering the near-surface transformation of the Al_3Ni phase into Al_3Ni_2. Furthermore, in collaboration with Prof. Muthupandian Ashokkumar from the School of Chemistry at the University of Melbourne and having performed the X-ray photoelectron spectroscopy (XPS) studies, it was found that use of a sonication medium such as ethanol or decane promotes the reduction processes on the surface of the treated alloy and, thus, affects the atomic ratio and chemical composition in metal alloys.

Gradient changes in phase composition and crystal size that HIUS produced in reductive media (ethanol/decane) lead to significant enhancement of electrocatalytic properties of AlNi alloys. After performing electrochemical test measurements (linear sweep voltammetry (LSV)) it was found that HIUS enables near-surface structuring of AlNi alloy particles toward electrocatalytic HER with significantly improved electrocatalytic properties such as reduced overpotential (η) and increased exchange current density (i_0). In particular, it has been shown that HIUS treatment in ethanol results in almost 146-fold increase in i_0 as compared to untreated alloy particles, placing sonochemical processing of metals/metal alloys is among the most promising methods for creation of an electrocatalytically active interface for hydrogen evolution. The experimentally determined electrocatalytic activity of the Al_3Ni_2 intermetallic phase was confirmed by means of density functional theory (DFT) calculations which were performed by Prof. Dr. Stephan Kuemmel from the department of Theoretical Physics at the University of Bayreuth. DFT calculations proved the concept proposed here of beneficial structuring of a catalytically active (Al_3Ni_2) phase with preferential orientation of the crystal planes (100) in the ultrasonically treated alloys for optimum hydrogen adsorption.

The obtained fundamental knowledge was successfully applied on development of materials with significantly enhanced electrocatalytic properties. Thus, with respect to formation of an electrocatalytically active interface, ultrasound treatment satisfies several requirements which are essential for the catalyst to be efficient. First, US treatment leads to overall structuring of HER active phases, namely their growth and exposure on the catalyst surface due to accelerated solid state atomic diffusion caused by the created temperature gradient. Second,

through the appropriate choice of the sonication medium it is possible to controllably avoid the formation of high surface area for prevention of hydrogen bubble trapping and associated increased electrolyte ohmic resistance. Additionally, sonication activates the catalyst surface, which is required for the achievement of the necessary hydrogen coverage. These steps may drastically reduce the applied overpotential for the HER process.

Overall, seemingly highly undesirable for industrial engineering applications the cavitation phenomenon (acoustically induced) has a great number of positive impacts in the area of catalytic materials formation. In other words, the method of ultrasound treatment is a perfect example of turning initially disadvantageous cavitation effects into highly beneficial ones. Thus, US treatment can be simply considered as a unique "one-pot" surface modification method which opens new prospective for inexpensive earth abundant metals such as aluminum and nickel to be used for fabrication of robust and highly efficient alternatives to platinum as electrocatalyst toward hydrogen evolution.

Zusammenfassung

Der Fokus der vorliegenden Doktorarbeit liegt auf der Verarbeitung von Partikeln aus einer Metalllegierung mit Hilfe von hoch intensivem Ultraschall (HIUS) für die potentielle Anwendung in elektrokatalytischer Wasserspaltungsreaktion für die Erzeugung von Wasserstoff. Während der Ultraschallbehandlung von Metallpartikeln wurden Veränderungen der Bulkeigenschaften (Kristallitgröße, Mikrospannung) und Veränderungen der Oberflächeneigenschaften (Zusammensetzung, Morphologie) studiert, um die fundamentalen Aspekte der akustischen Kavitation sowie ihre Effekte auf die ultraschallbehandelte Materie aufzudecken und die verbesserte elektrokatalytische Leistung des ursprünglich inaktiven Metalllegierungskatalysators zu erklären.

Durch die geeignete Wahl des Ultraschallmediums, der Konzentration der ultraschallbehandelten Partikel Suspension und der Dauer der Ultraschallbehandlung wurde es möglich, Einblicke in das Phänomen der Kavitation und der dazugehörigen physikalischen (Energieübertragung, thermische Auswirkung, Festkörper Atomdiffusion) und chemischen (Phasenumwandlung, Red-Ox. Reaktionen) Prozesse zu gewinnen. Infolgedessen wurde ein, auf AlNi basierender, Elektrokatalysator mit erheblich verbesserten Eigenschaften (reduzierte Überspannung, höherer Stromstärke Ausgabeleistung) für die Wasserstoffentwicklungsreaktion durch Einstellen der Parameter der Ultraschallbehandlung hergestellt.

Eine neue Methode zur quantitativen Bestimmung der Energieübertragung zwischen kollabierenden Kavitationsblasen und ultraschallbehandelter Materie wurde entwickelt. Die Methode basiert auf der Analyse kristallographischer Parameter des Materials mittels Röntgenpulverdiffraktogrammen. Durch die Überwachung der Kristallitgrößen der in der Legierung vorhandenen intermetallischen Phasen Al_3Ni und Al_3Ni_2 mit Hilfe der Scherrer und Williamson-Hall Methoden wurde gezeigt, dass der sich durch die ultraschallbehandelten Partikel ausbreitende Temperaturgradient die atomare Diffusion auslöst und zu einer Vergrößerung der Kristallitgrößen sowie zu einer Verringerung der Mikrospannung im System führt.

Die hier vorgeschlagene Methode zur Bewertung der Auswirkung der Kavitation auf Festköper wurde für die Abschätzung der durchschnittlichen Mindesttemperatur $\left(\overline{T}_{particle}^{min}\right)$, bis zu der die Partikel erhitzt werden können angewendet. Der durch die Kavitation induzierte Temperaturgradient ist stark von den physikalischen Eigenschaften wie Dampfdruck

und Viskosität des Ultraschallmediums abhängig, welche in der Reihenfolge Ethylenglykol < Ethanol < Wasser < Dekan ansteigen. Des Weiteren wurde anhand der erhaltenen Daten die Energieübertragung von der kollabierenden Kavitationsblase zum ultraschallbehandelten Partikel in Dekan abgeschätzt welche ~ 17 % effizienter ist als in Ethylenglykol.

Zeitgleich mit der Festkörper Atomdiffusion im Bulkmetall lösen thermische, mechanische und chemische Auswirkungen der Kavitationsblasen auf die Metalloberfläche die Phasenumwandlungsreaktionen in einer nm-dicken Grenzschicht aus. In Zusammenarbeit mit Prof. Dr. Juergen Senker vom Lehrstuhl Anorganische Chemie III an der Universität Bayreuth wurde mit Hilfe von ^{27}Al Festkörper NMR demonstriert, dass, obwohl die Bildung von Al_3Ni_2 Phase an der Oberfläche der AlNi Legierungen kinetisch eingeschränkt ist, kollabierende Kavitationsblasen die Oberfläche auf 1124 K erhitzen und eine oberflächennahe Umwandlung der Al_3Ni Phase in Al_3Ni_2 auslösen. Weiterhin wurde in Zusammenarbeit mit Prof. Muthupandian Ashokkumar von der School of Chemistry an der Universität Melbourne und mit den durchgeführten Röntgen-Photoelektronen-Spektroskopie (XPS) Messungen herausgefunden, dass die Verwendung von Ultraschallmedien wie Ethanol oder Dekan die Reduktionsprozesse an der Oberfläche der behandelten Legierung begünstigen und damit das Atomverhältnis sowie die chemische Zusammensetzung in den Metalllegierungen beeinflussen.

Veränderungen in der Phasenzusammensetzung und der Kristallgröße durch HIUS in reduzierenden Medien (Ethanol/Dekan) führen zur erheblichen Verbesserung der elektrokatalytischen Eigenschaften der AlNi Legierung. Durchelektrochemische Testmessungen (Lineare Voltametrie (linear sweep voltammetry (LSV)) wurde herausgefunden, dass HIUS die oberflächennahe Strukturierung von AlNi-Legierung-Partikeln für die elektrokatalytische Wasserstoffentwicklungsreaktion mit stark verbesserten elektrokatalytischen Eigenschaften wie reduzierte Überspannung (η) und erhöhte spezifische Austauschstromdichtewerte (i_0) ermöglicht. Im Besonderen wurde gezeigt, dass die Behandlung mit HIUS in Ethanol im Vergleich zu unbehandelten Legierungs-Partikeln zu einer fast 146-fachen Zunahme des i_0 Wertes führt, und somit die sonochemische Verarbeitung von Metallen/Metalllegierungen zu einer der vielversprechendsten Methoden in der Herstellung elektrokatalytisch aktiver Grenzflächen für die Wasserstoffgewinnung gehört. Die experimentell bestimmte elektrokatalytische Aktivität der intermetallischen Al_3Ni_2 Phase wurde durch Dichtefunktional Theorie (DFT) Berechnungen von Prof. Dr. Stephan Kuemmel vom Lehrstuhl Theoretische Physik an der Universität Bayreuth bestätigt. Die DFT Berechnungen beweisen das hier vorgeschlagene Konzept der vorteilhaften

Strukturierung der katalytisch aktiven (Al_3Ni_2) Phase mit Präferenz für die Wasserstoff Adsorptionsorientierung von Kristallebenen (100) in den ultraschallbehandelten Legierungen.

Das gewonnene fundamentale Wissen wurde erfolgreich in die Entwicklung eines Materials mit erheblich verbesserten elektrokatalytischen Eigenschaften einbezogen. Folglich erfüllt die Ultraschallbehandlung, mit Blick auf die Bildung einer elektrokatalytisch aktiven Grenzfläche, mehrere Voraussetzungen die für die Effizienz des Katalysators wesentlich sind. Erstens führt die Ultraschallbehandlung zu einer allgemeinen Strukturierung der für die Wasserstoffentwicklungsreaktion aktiven Phasen und zwar zu deren Wachstum und deren Freilegung an der Katalysatoroberfläche durch beschleunigte Festkörper Atomdiffusion, die durch den geschaffenen Temperaturgradienten verursacht wurde. Zweitens ist es durch die geeignete Wahl des Ultraschallmediums möglich, die Bildung einer großen Oberfläche kontrolliert zu vermeiden, um dem Einfangen von Wasserstoffblasen und der damit verbundenen Zunahme des Ohm'schen Widerstands des Elektrolyten vorzubeugen. Zusätzlich wird die Katalysatoroberfläche während der Ultraschallbehandlung aktiviert. Dies ist für das Erreichen der notwendigen Wasserstoffbedeckung erforderlich. Diese Maßnahmen könnten die angelegte Überspannung für die Wasserstoffentwicklungsreaktion drastisch senken.

Im Allgemeinen, hat das für industrielle Anwendungen scheinbar hoch unerwünschte (akustisch induziert) Kavitationsphänom eine große Anzahl an positiven Auswirkungen im Bereich der Entwicklung katalytischer Materialien. Mit anderen Worten, die Methode der Ultraschallbehandlung ist ein perfektes Beispiel für das Umkehren eines ursprünglich ungünstigen Kavitationseffektes in einen sehr nützlichen Effekt. Deshalb kann die Ultraschallbehandlung als eine einzigartige „Ein-Topf" Oberflächenmodifikationsmethode betrachtet werden, welche für auf der Erde reichlich vorkommende und preiswerte Metalle wie Aluminium und Nickel eine robuste und hoch effiziente Alternative zu dem Platin Elektrokatalysator für die Wasserstoffgewinnung eröffnet.

List of Publications / Awards

1. **Formation of polypyrrole/metal hybrid interfacial layer with self-regulation functions via ultrasonication.** Skorb, E.V.; Baidukova, O.; Andreeva, O.; Cherepanov, P.V.; Andreeva, D.V., *Bioinspired, Biomimetic and Nanobiomaterials*, **2**(3), 123-129 (2013)

2. **SERS Platforms of Plasmonic Hydrophobic Surfaces for Analyte Concentration: Hierarchically Assembled Gold Nanorods on Anodized Aluminum.** Tebbe, M.; Cherepanov, P.V.; Skorb, E.K.; Poznyak, S.K.; G. de Abajo, J.; Fery, A.; Andreeva, D.V.; Alvarez Puebla, R.A.; Pazos-Perez, N., *Particle and Particle Systems Characterization*, **31**(11), 1134-1140 (2014)

3. **Effect of high intensity ultrasound on Al_3Ni_2, Al_3Ni crystallite size in binary AlNi (50 wt.% of Ni) alloy.** Cherepanov, P.V.; Melnyk, I.; Andreeva, D.V., *Ultrasonics Sonochemistry*, **23**, 26-30 (2015)

4. **Ultrasound assisted formation of Al-Ni electrocatalyst for hydrogen evolution.** Cherepanov, P.V.; Ashokkumar, M.; Andreeva, D.V., *Ultrasonics Sonochemistry*, **23**, 142-147 (2015)

5. **Sonogenerated metal-hydrogen sponges for reactive hard templating.** Baidukova, O.; Möhwald, H.; Mazheika, A.S.; Sviridov, D.V.; Palamarciuc, T.; Weber, B.; Cherepanov, P.V.; Andreeva, D.V.; Skorb, E.V., *Chemical Communications*, **51**, 7606-7609 (2015)

6. **Up to which temperature ultrasound can heat the particle?** Cherepanov, P.V.; Kollath, A.; Andreeva, D.V., *Ultrasonics Sonochemistry*, **26**, 9-14 (2015)

7. **The use of ultrasonic cavitation for near-surface structuring of robust and low-cost AlNi catalysts for hydrogen production.** Cherepanov, P. V.; Melnyk, I,; Skorb, E. V.; Fratzl, P.; Zolotoyabko, E.; Dubrovinskaia, N.; Dubrovinsky, L.; Avadhut, Y.S.; Senker, J.; Leppert, L.; Kümmel, S.; Andreeva, D. V., *Green Chemistry*, **17**, 2745-2749 (2015)

8. **Controllable manipulation of crystallinity and morphology of aluminium surface using high intensity ultrasound.** Kollath, A.; Cherepanov, P.V.; Andreeva, D.V., accepted in *Applied Acoustics* (2015)

9. **Ultrasound-assisted Synthesis of Electrocatalysts for Hydrogen Production.** Cherepanov, P.V.; Andreeva, D.V., *Handbook of Ultrasonics and Sonochenistry* (Ed. Ashokkumar, M.), submitted (2015)

10. **Initiation of kinetically restricted phase transformations in AlNi (50wt.% of Ni) alloys using high intensity ultrasound.** Cherepanov, P.V.; Avadhut, Y.S.; Senker, J.; Andreeva, D.V., to be submitted in *ZAAC* (2015)

11. **Shape-dependent Interactions of Palladium Nanocrystals with Hydrogen.** Klinkova, A.; Cherepanov, P.V.; Ryabinkin, I.G.; Ashokkumar, M.; Andreeva, D.V.; Izmaylov, A.F.; Kumacheva, E., to be submitted in ACS Nano (2015)

Best oral presentation award at the 1st *Asia-Oceania Sonochemical Society* conference. Melbourne, Australia (2013)

List of Abbreviations and Symbols

α	symmetry coefficient
β	peak broadening
b	tafel slope
BET	Brunauer-Emmett-Teller analysis
DMA	dimethylamine
DMF	dimethylformamid
CNT	carbon nanotubes
ΔG_{H*}	free energy of hydrogen adsorption
ΔH	enthalpy of formation
D	effective crystallite size
DFT	density functional theory
ε	microstrain
EDS	energy dispersive spectroscopy
EPR	electron paramagnetic resonance spectroscopy
F	faraday constant
FWHM	full width at half maximum
γ	specific heat ratio
η	overpotential
HER	hydrogen evolution reaction
HIUS	high intensity ultrasound
HPUS	high power ultrasound
i_0, j_0	exchange current density
j	current density
k	shape factor
λ	wavelength
LSV	linear sweep voltammetry

MBSL	multibubble sonoluminescence
MGF	mesoporous graphene foam
NMR	nuclear magnetic resonance
NSAs	near-surface alloys
P	pressure
PIGE	paraffin impregnated graphite electrode
PXRD	powder X-ray diffraction
R	ideal gas constant
R	radius
Rmax	maximum radius
SEM	scanning electron microscopy
T	temperature
$\overline{T}_{particle}^{min}$	minimum average temperature of the metal particle
TEM	transmission electron microscopy
THF	tetrahydrofuran
V	applied potential
V_{cell}	unit cell volume
WH	Williamson – Hall method
XPS	X-ray photoelectron spectroscopy

1 Introduction

Hydrogen is an environmentally friendly energy carrier. Being the simplest molecule in our universe, yet it has the largest energy density over any other fuel [1] and is considered to be an excellent energy carrier [2, 3]. Over the last few decades it was successfully used as a fuel for propelling space ships and rockets into the orbit. Apart from rocket fuel and hydrogen fuel cells [4, 5], it is also widely used for ammonia production [6] which is later converted into fertilizers for agricultural needs. The majority (~95 %) of hydrogen is produced today by steam reforming of fossil fuel [7] such as natural gas, petroleum, and coal. The second most popular method of hydrogen production is electrolytic water splitting [8] which accounts only for about ~4 % of the total production, due to the high overpotential (-1.48 V) of the hydrogen evolution reaction (HER) [9]. The HER is a process of hydrogen production from various sources including water. Technologically, production of molecular hydrogen via water splitting is a "green" process that does not produce harmful side products and uses renewable energy (grid, wind, solar). Nowadays one of the major needs for efficient electrolysis is the development of low-cost, active, and stable catalysts [10].

In the last few decades there have been carried out extensive studies on the subject of finding efficient, robust, and low-cost catalysts for electrocatalytic water splitting, which could potentially replace the currently used Pt electrocatalysts [11-13]. Having found such a catalyst would make the overall process of highly pure hydrogen production by electrolysis preferable from the economical point of view in comparison to fossil fuel processing. Even though Pt is considered to be the most efficient material toward HER [14], it has two major disadvantages – low abundance in nature and extremely high cost. Thus, the attention of scientists was drawn into investigation of potentially as efficient, less expensive, and significantly more abundant materials [15].

It was shown that, for example, nanoalloys consisting of transition metals potentially can have excellent catalytic properties for hydrogen production [16]. However, up to now the efficiency of electrocatalysts that were prepared using nanoalloys was significantly lower comparing to Pt. The low efficiency of nanoalloys is probably related to the low accessibility of active centres for hydrogen. Thus it was proposed, that nanostructures with particular orientation

of the beneficial crystallographic planes that provide their maximum accessibility for hydrogen are desirable for an efficient electrocatalyst. For example, exposure of the (100) edge planes in MoS_2 for hydrogen adsorption leads to the significant enhancement of its electrocatalytic properties [17].

Recently, in order to enhance the efficiency of alloys for electrocatalysis, near-surface and surface alloys were proposed [18]. Near-surface alloys are characterized by different composition of surface layer and support. The electrocatalytic properties of such alloys were demonstrated for a few systems that were prepared by deposition-annealing using transition metals and the Pt (111) surface [19]. However, in many cases near-surface alloys require sophisticated and multistage preparation procedures. Furthermore, efficient structures are often sensitive to acidic or basic environment and change their surface composition upon hydrogen adsorption.

Nevertheless, recent achievements in structuring of inorganic materials demonstrated that they may become more attractive for industry if novel economically effective methods of manipulation of the metal surface at atomic level can be proposed. Most of them employ wet chemistry approaches, which can be quite sophisticated and lengthy. Among those are catalysts synthesized by means of carburization [20], solvothermal processing [21], microwave-assisted hydrothermal approach [22], ammonolysis [23], selenization [24] etc. Many of the synthesis pathways involve complex steps of nanoengineering to produce nanoparticles, nanosheets, or nanowires [22, 25, 26]. Some also include the catalyst incorporation on various supports, such as impregnation into carbon nanotubes, mesoporous graphene foams, reduced graphene oxide sheets etc. [27-29]. In addition to synthesis, the majority of the catalysts must be activated prior their use, which overall extends the preparation time significantly and requires additional power input. As a result, at the present time it seems unlikely to establish a simple method that could be used for creation of an electrocatalyst as efficient as Pt from earth abundant metals without utilizing rare elements or expensive precursors. Nevertheless, an unexpected solution of this issue may come from the area of acoustic chemistry, as this thesis will demonstrate.

High intensity ultrasound (HIUS) is a unique technological approach for the synthesis of metallic nanomaterials and solid-state processing of metals [30-32]. HIUS provides extreme conditions for both bottom-up [33, 34] and top-down [35] approaches to the design of nanomaterials. Sonochemistry is an area that has been developing over the last few decades [36].

It is mainly associated with the effect of cavitation [37, 38], that is known to occur naturally and is notorious for its destructive properties being a significant cause of wear in many engineering contexts [39]. Surprisingly, controlled acoustic cavitation can serve as a simple and powerful tool for the fabrication of HER active electrocatalysts.

In the present thesis, intensive studies on the subject of ultrasound processing of metal/metal alloys revealed numerous fundamental aspects such as the temperature impact of cavitation bubble implosion, solid-state atomic diffusion, morphological and compositional changes. The obtained fundamental knowledge was successfully implemented for development of materials with significantly enhanced electrocatalytic properties. Thus, with respect to formation of electrocatalytically active interfaces, ultrasound treatment satisfies several requirements that are important for the catalyst to be efficient.

Throughout the thesis it will be demonstrated that HIUS treatment leads to overall structuring of HER active phases, namely their growth and exposure on the catalyst surface due to accelerated solid-state atomic diffusion caused by the created temperature gradient. Second, through the appropriate choice of sonication medium it is possible to controllably avoid the formation of a porous surface for prevention of hydrogen bubble trapping and associated increased electrolyte ohmic resistance. Additionally, while sonicated, the catalyst surface is being activated, which is required for the achievement of the necessary hydrogen coverage. This step may drastically reduce the applied overpotential of the HER process.

Overall, US treatment can be simply considered as a unique and elegant "one-pot" surface modification method which opens new perspectives for inexpensive earth abundant metals such as aluminum and nickel to be used for fabrication of robust and highly efficient alternatives to platinum electrocatalysts toward hydrogen evolution.

References

[1] S. Dunn, Hydrogen futures: toward a sustainable energy system, Int. J. Hydrog. Energy, 27 (2002) 235-264.

[2] N. Armaroli, V. Balzani, The future of energy supply: Challenges and opportunities, Angew. Chem.-Int. Edit., 46 (2007) 52-66.

[3] L. Barreto, A. Makihira, K. Riahi, The hydrogen economy in the 21st century: a sustainable development scenario, Int. J. Hydrog. Energy, 28 (2003) 267-284.

[4] K.D. Kreuer, On the development of proton conducting polymer membranes for hydrogen and methanol fuel cells, J. Membr. Sci., 185 (2001) 29-39.

[5] T. Rostrup-Nielsen, Manufacture of hydrogen, Catal. Today, 106 (2005) 293-296.

[6] A. Klerke, C.H. Christensen, J.K. Norskov, T. Vegge, Ammonia for hydrogen storage: challenges and opportunities, J. Mater. Chem., 18 (2008) 2304-2310.

[7] J.D. Holladay, J. Hu, D.L. King, Y. Wang, An overview of hydrogen production technologies, Catal. Today, 139 (2009) 244-260.

[8] M. Carmo, D.L. Fritz, J. Merge, D. Stolten, A comprehensive review on PEM water electrolysis, Int. J. Hydrog. Energy, 38 (2013) 4901-4934.

[9] J.M. Ogden, Prospects for building a hydrogen energy infrastructure, Annu. Rev. Energ. Environ., 24 (1999) 227-279.

[10] Hydrogen production. Overview of technology options. Report of Freeadom Car Fuel Partnership (2009) https://www1.eere.energy.gov/hydrogenandfuelcells/pdfs/h2_tech_road map.pdf

[11] F. Harnisch, G. Sievers, U. Schroder, Tungsten carbide as electrocatalyst for the hydrogen evolution reaction in pH neutral electrolyte solutions, Appl. Catal. B-Environ., 89 (2009) 455-458.

[12] B. Hinnemann, P.G. Moses, J. Bonde, K.P. Jorgensen, J.H. Nielsen, S. Horch, I. Chorkendorff, J.K. Norskov, Biornimetic hydrogen evolution: MoS2 nanoparticles as catalyst for hydrogen evolution, J. Am. Chem. Soc., 127 (2005) 5308-5309.

[13] P.C. Chen, Y.M. Chang, P.W. Wu, Y.F. Chiu, Fabrication of Ni nanowires for hydrogen evolution reaction in a neutral electrolyte, Int. J. Hydrog. Energy, 34 (2009) 6596-6602.

[14] M.S. Faber, S. Jin, Earth-abundant inorganic electrocatalysts and their nanostructures for energy conversion applications, Energy Environ. Sci., 7 (2014) 3519-3542.

[15] It's elemental – the periodic table of elements. Jefferson Lab. http://education.jlab.org/itselemental

[16] E. Skulason, V . Tripkovic, M.E. Björketun, S. Gudmundsdottir, G. Karlberg, J. Rossmeisl, T. Bligaard, H. Jonsson, J.K. Norskov, Modeling the electrochemical hydrogen oxidation and evolution reactions on the basis of density functional theory calculations, J Phys Chem C, 114 (2010) 18182-18197.

[17] T.F. Jaramillo, K.P. Jørgensen, J. Bonde, J.H. Nielsen, S. Horch, I. Chorkendorff, Identification of active edge sites for electrochemical H_2 evolution from MoS_2 nanocatalysts, Science 317 (2007) 100-102.

[18] J. Greeley, M. Mavrikakis, Alloy catalysts designed from first principals. Nature Mater., 3 (2004) 810-815

[19] J. Knudsen, A.U. Nilekar, R.T. Vang, J. Schnadt, E.D.L. Kunkes, J.A. Dumesic, M. Mavrikakis, F. Nesenbacher, Cu/Pt near-surface alloy for water−gas shift satalysis, J. Am. Chem. Soc., 129 (2007) 6485-6490.

[20] P. Xiao, X. Ge, H. Wang, Z. Liu, A. Fisher, X .Wang, Novel Molybdenum Carbide–Tungsten Carbide Composite Nanowires and Their Electrochemical Activation for Efficient and Stable Hydrogen Evolution, Adv. Funct. Mater., 25 (2015) 1520-1526.

[21] J. Rajeswari, P.S. Kishore, B. Viswanathan, T.K. Varadarajan, Facile Hydrogen Evolution Reaction on WO3 Nanorods, Nanoscale Res. Lett., 2 (2007) 496-503.

[22] A. Phuruangrat, D.J. Ham, S.J. Hong, S. Thongtem, J.S. Lee, Synthesis of hexagonal WO3 nanowires by microwave-assisted hydrothermal method and their electrocatalytic activities for hydrogen evolution reaction, J. Mater. Chem., 20 (2010) 1683-1690.

[23] B. Cao, G.M. Veith, J.C. Neuefeind, R.R. Adzic, P.G. Khalifah, Mixed Close-Packed Cobalt Molybdenum Nitrides as Non-noble Metal Electrocatalysts for the Hydrogen Evolution Reaction, J. Am. Chem. Soc., 135 (2013) 19186-19192.

[24] D. Kong, H. Wang, Z. Lu, Y. Cui, CoSe2 Nanoparticles Grown on Carbon Fiber Paper: An Efficient and Stable Electrocatalyst for Hydrogen Evolution Reaction, J. Am. Chem. Soc. 136 (2014) 4897-4900.

[25] Z. Xing, Q. Liu, A.M. Asiri, X. Sun, Closely Interconnected Network of Molybdenum Phosphide Nanoparticles: A Highly Effi cient Electrocatalyst for Generating Hydrogen from Water, Adv. Mater., 26 (2014) 5702-5707.

[26] E.J. Popczun, J.R. McKone, C.G. Read, A.J. Biacchi, A.M. Wiltrout, N.S. Lewis, R.E. Schaak, Nanostructured Nickel Phosphide as an Electrocatalyst for the Hydrogen Evolution Reaction, J. Am. Chem. Soc., 135 (2013) 9267-9270.

[27] W.F. Chen, J.T. Muckerman, E. Fujita, Recent developmentsin transition metal carbides and nitrides as hydrogen evolution electrocatalysts, Chem. Commun., 49 (2013) 8896-8909.

[28] L. Liao, J. Zhu, X. Bian, L. Zhu, D.S. Scanlon, H.H. Girault, B. Liu, MoS_2 Formed on Mesoporous Graphene as a Highly Active Catalyst for Hydrogen Evolution, Adv. Funct. Mater., 23 (2013) 5326-5333.

[29] H. Tang, K. Dou, C.C. Kaun, Q. Kuang, S. Yang, MoSe2 nanosheets and their graphene hybrids: synthesis, characterization and hydrogen evolution reaction studies, J. Mater. Chem. A, 2 (2014) 360-364.

[30] E.V. Skorb, D.V. Andreeva, Bio-inspired ultrasound assisted construction of synthetic sponges, J. Mater. Chem. A., 1 (2013) 7547-7557.

[31] J.H. Bang, K.S. Suslick, Applications of Ultrasound to the Synthesis of Nanostructured Materials, Adv. Mater., 22 (2010) 1039-1059.

[32] E.V. Skorb, D.V. Andreeva, Surface nanoarchitecture for bio-applications: self-regulated intelligent interfaces, Adv. Func. Mater., 23 (2013) 4483-4506.

[33] K.S. Suslick, G.J. Price, Application of ultrasound to materials chemistry, Annu. Rev. Mater. Sci., 29 (1999) 295-326.

[34] K.S. Suslick, T. Hyeon, M. Fang, Nanostructured materials generated by high-intensity ultrasound: sonochemical synthesis and catalytic studies, Chem. Mater., 8 (1996) 2172-2179.

[35] S.J. Doktycz, K.S. Suslick, Interparticle collisions driven by ultrasound, Science, (1990) 1067-1069.

[36] M. Ashokkumar, T. Mason, Sonochemistry, in: Kirk-Othmer Encylcopedia of Chemical Technology, John Wiley & Sons, 2007.

[37] O.V. Abramov, High-Intensity Ultrasound, Gordon and Breach Science Publishers, 1998.

[38] M.A. Margulis, Sonochemistry and Cavitation, Gordon and Breach Publishers, 1995.

[39] H. Conrad, J. Narayan, On the grain size softening in nanocrystalline materials, Scripta Mater., 42 (2000) 1025-1030.

2   Theory / Status of the Field

The present chapter provides the theoretical basic background in the area of ultrasound in heterogeneous systems and electrocatalysis necessary for understanding this work. Initially, such terms as ultrasound and acoustic cavitation are introduced. Further, the nucleation, growth, and collapse of the cavitation bubble as well as the effects arising from the collapse are discussed. Additionally, a short overview of the electrocatalytic hydrogen production mechanism together with defined requirements for efficient catalyst fabrication and a summary of existing catalytic materials are provided. The chapter ends with the objectives of the thesis.

2.1   Ultrasound and Acoustic Cavitation in Heterogeneous Systems

An oscillating sound pressure wave with frequencies greater than 20 kHz is called ultrasound [1]. Such a pressure oscillation propagates in air or liquid with the speed of sound [2]. Ultrasound is inaudible for humans due to its frequency that lies beyond the human hearing range. Ultrasound irradiation of liquids results in the formation of vapor cavities (bubbles or voids) which are defined as acoustic cavitation [3, 4]. More precisely, acoustic cavitation can be described as formation, growth and subsequent collapse of ultrasonically induced bubbles [5, 6]. **Fig. 2.1** illustrates the common stages which a cavitation bubble undergoes after nucleation: oscillating growth (a), deformation (b), and implosion (collapse) (c) near the surface in heterogeneous systems where the size of particles suspended in sonication medium significantly exceeds the size of the cavitation bubble.


Oscillating Bubble growth   **Static pressure increase**   **Implosion of the bubble**

a   b   c
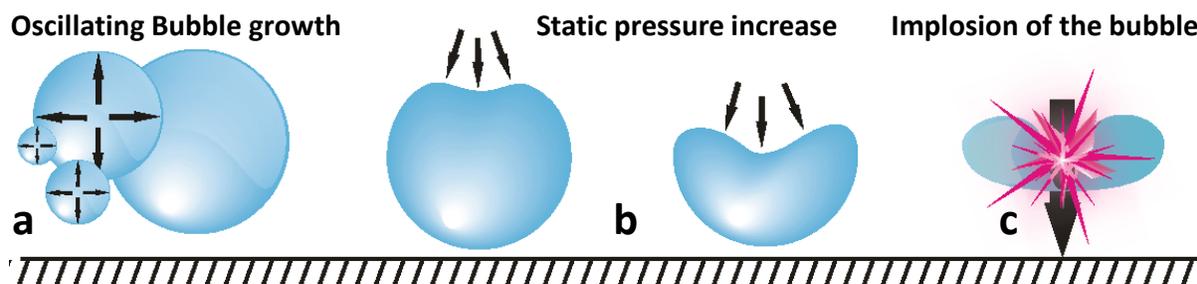
Fig. 2.1: *Schematic illustration of acoustic cavitation in liquid upon intense ultrasound irradiation.*

The mechanism of the overall process can be explained as following: once the acoustic wave pressure amplitude exceeds the atmospheric pressure, the so called instantaneous pressure becomes negative [7] and initiates cavitation bubble formation since air/gas cannot be dissolved in the liquid any longer under negative pressure. Meanwhile, the static pressure surrounding the newly formed cavitation bubble is increasing (opposite to boiling process), which results in its deformation and forcing its implosion/collapse [8].

2.2 Dynamics of the Cavitation Bubbles (Nucleation, Growth, and Lifetime) in Heterogeneous Systems

2.2.1 Nucleation of the Cavitation Bubble

There are several possibilities for nucleation of the cavitation bubble [9] which are summarized in **Fig. 2.2**. According to the first one, nucleation can occur at the surface of solids [10], especially at the crevices of motes or suspended particles.
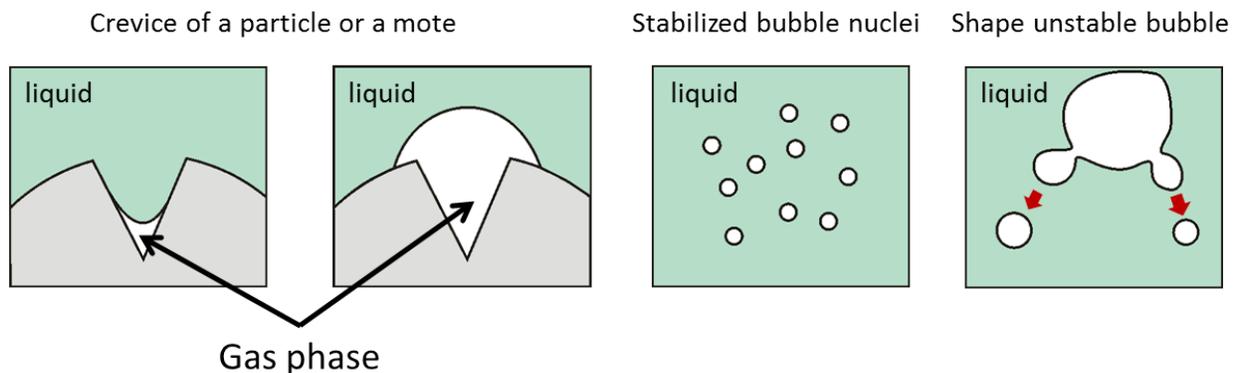
Fig. 2.2: *Various pathways for nucleation of the cavitation bubble.*

Stabilized against dissolution into liquid a gas pocket in the crevice (partial pressure in the gas pocket is lower than the partial pressure of dissolved gas) upon ultrasound irradiation expands due to diffusion of gas dissolved in the surrounding liquid. After several expansion/compression cycles, the cavitation bubble grows to its critical size [11]. The second possibility arises from the fact that the liquid initially contains tiny bubbles (few μm in size) [12], which might be stabilized by a surfactant present as impurity. Such stabilized nuclei are growing during ultrasound irradiation due to gas diffusion and/or by coalescence [9]. Last but no least nucleation can occur

during fragmentation of already active but shape unstable [13, 14] cavitation bubbles [15] or upon collapse, when the bubble simply initiates a jet of smaller ones [16]. In heterogeneous systems such as suspensions of metal particles with average size of more than 150 μm nucleation preferably occurs at surfaces that might contain a large amount of crevices.

2.2.2   *Growth of the Cavitation Bubble*

It is believed that cavitation bubbles grow according to two mechanisms: either by coalescence [17] of already existing bubbles or due to gas diffusion into newly nucleated bubble (rectified diffusion) [9, 18]. During rectified diffusion the rates of cavitation bubble growth are strongly dependent on amplitude and frequency of ultrasound irradiation [19, 20]. Even though the grow rate by coalescence is not quantified yet, it is known that bubbles coalesce due to either primary radiation force (primary Bjerknes force) or secondary attractive radiation force (secondary Bjerknes force) [21]. Specifically,the primary Bjerknes force drives the bubbles to the pressure antinode of a standing wave [22]. Both forces are known to originate from the pressure gradient across the bubble [22, 23]. It is important to note, that the first mechanism of cavitation bubble growth should be taken into account, if homogeneous systems are concerned. In case of heterogeneous systems cavitation bubble growth will be most likely caused by the rectified gas diffusion mechanism due to presence of a large number of bubbles newly nucleated in the crevices or motes.

2.2.3   *Size and Lifetime of the Cavitation Bubble*

To date, the cavitation bubble size [24] has been estimated with help of several available experimental techniques such as laser light diffraction [25], active cavitation detection [26], phase-Doppler [27], and multibubble sonoluminescence (MBSL) [28]. All reported data for the bubble sizes are in a good agreement with each other and represent comparable results. **Table 2.1** summarizes the experimentally measured reasonable radii at various frequencies, indicating a slight increase in cavitation bubble size upon decrease of the ultrasonic frequency. The lifetime of the cavitation bubble depends on its nature. Thus, according to general terminology, cavitation bubbles are classified either as stable (weakly and symmetrically oscillating bubbles) and active (transient) [29, 30].

Table 2.1: *Experimentally measured resonance bubble radii at various frequencies* [29]

Experimental technique	Frequency of US irradiation (kHz)	Experimental radius R_o (μm)
Active cavitation	1100	0.9 – 1.38
Pulsed MBSL	515	2.8 – 3.7
Laser diffraction	20	3.8
Phase-Doppler	20	5.0

Leighton [9] further suggested a more accurate classification with respect to the actual cavitation bubble collapse where transient cavitation should be identified as "fragmentary transient cavitation" and stable cavitation as "repetitive transient cavitation". Therefore, transient cavitation bubbles refer to high energy collapse followed by fragmentation and formation of the new cavitation nuclei with detected lifetime of about 100 -350 μs [31], while stable cavitation bubbles repetitively collapse several times extending their lifetimes to values of around ~17 ms or approximately 5000 acoustic cycles depending on the acoustic frequency [32]. Thus, based on the existing information about cavitation bubble size, during ultrasound processing of metal particle suspensions (particle size >150 μm) at 20 kHz frequency the bubble size is expected to lie in the range of 15 – 20 μm.

2.3   Effects Caused by Cavitation Bubble Collapse

Upon expanding to its critical size, acoustic cavitation bubbles strongly collapse (Rayleigh collapse) [33] and a bouncing radial motion is observed after the collapse. **Fig. 2.3a** represents the radius – time curve for a single acoustic cycle which is calculated with help of a modified Keller equation [34]. The collapse of acoustic cavitation bubbles is a quasi – adiabatic process, that is associated with extremely fast thermal conduction between surrounding medium and bubble interior [6, 35]. Such a near adiabatic collapse results in dramatic temperature (thousands of Kelvin) and pressure (hundreds of bars) increase inside the cavitation bubble. These extreme conditions are responsible for the formation of free radicals [36, 37], that are generated from the sonication medium vapor and oxygen inside the bubble. After the end of the collapse, the bubble emits shock waves [38] which are causing considerably strong turbulences in the surrounding medium.
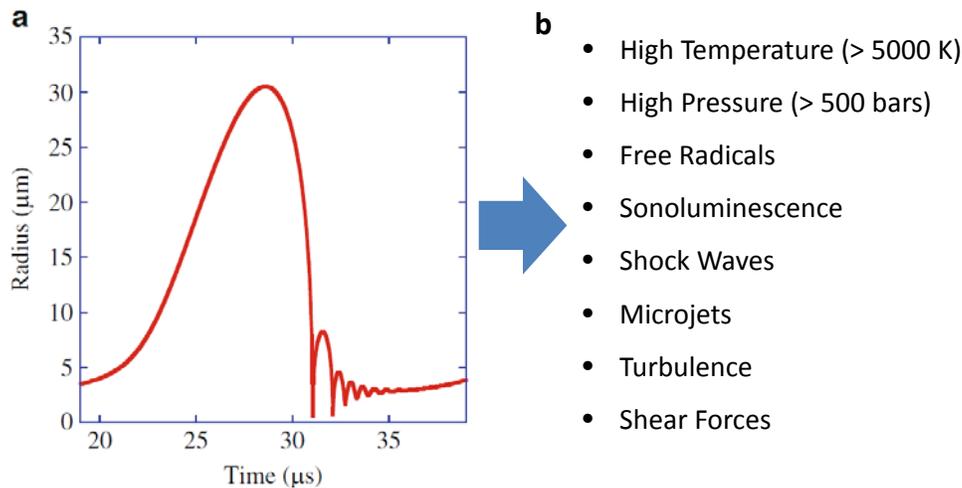
Fig. 2.3: *The calculated results for one acoustic cycle, when a bubble in water is irradiated by an acoustic wave (a) reprinted with permission from* [34]*; summary of the effects caused by cavitation bubble collapse (b).*

Additionally, the collapse of the bubble initiates microjet formation as well as the occurrence of shear forces [39] and sonoluminescence [40, 41] (**Fig. 2.3b**). In case of ultrasound treatment of metal particle suspensions [42], the effects resulting from the cavitation bubble collapse are expected to play an important role in the processes of compositional and morphological changes. Specifically, temperature and pressure impact, generation of reductive/oxidative species, shock wave and microjet occurrence are among the major contributors to changes of such systems.

2.3.1 Internal Temperature of the Collapsing Cavitation Bubble

At the end of the violent collapse the temperature inside the cavitation bubble dramatically increases [43]. The results calculated based on air bubble collapse as a model and use of a modified Keller equation show ,that the temperature may reach values of up to 6500 K (**Fig. 2.4a**) [34]. If the calculations are based on the model, that assumes isothermal bubble expansion and adiabatic compression phase, the maximum temperature within the bubble is estimated to be ~ 4600 K (**Fig. 2.4b**) [43].
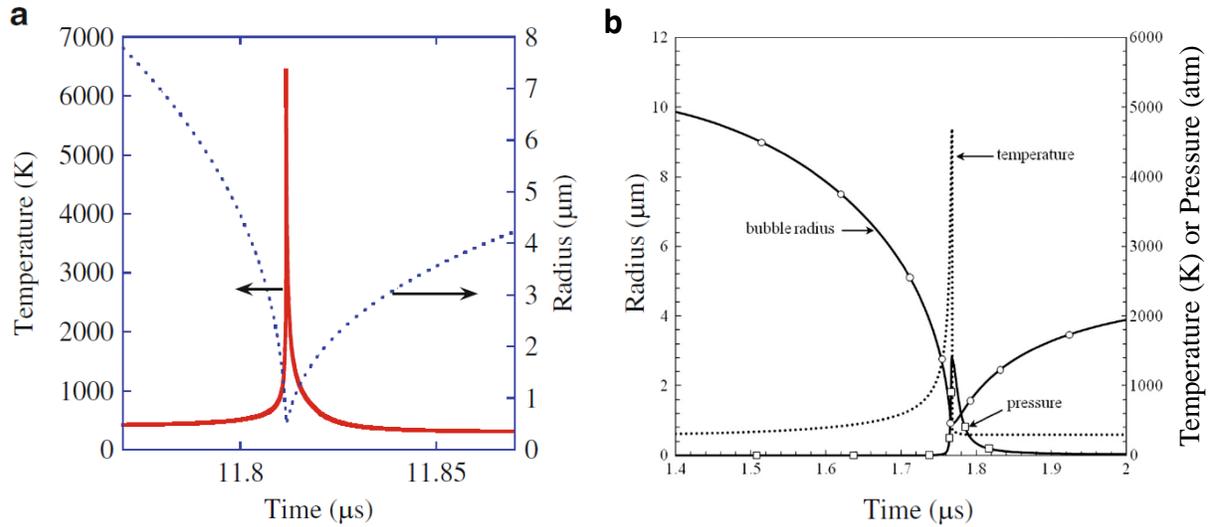
Fig. 2.4: *The calculated bubble radius and internal temperature (a) reprinted with permission from [34]; the calculated bubble radius, internal temperature and pressure (b) reprinted with permission from [43].*

Besides that, when taking into account a simple thermodynamic model for cavitation bubble collapse along with the assumption of adiabatic compression , the maximum theoretical temperature within the bubble can be estimated using the following equation [9]:

$$T_{max} = T_0 \left\{ \frac{P_m(\gamma - 1)}{P_v} \right\}$$

where T_0 is the ambient solution temperature, P_m is the pressure in the liquid (a sum the hydrostatic and acoustic pressures) $\gamma = c_p/c_v$ is the specific heat ratio of the gas-vapor mixture, and P_v is the pressure in the bubble at its maximum size, allowing to calculate the maximum theoretical temperature within the bubble (T_{max}). Thus, assuming $P_m = 2$ atm, for example, the theoretical (T_{max}) may reach a value of ~ 6150 K [44].

Experimentally, estimation of the temperature inside the cavitation bubble has been made by a number of research groups. Methods used for experimental temperature estimation and obtained temperature ranges are summarized in the **Table 2.2.** The experimentally determined temperature within collapsing cavitation bubbles varies depending on the method used. Nevertheless, the lowest possible temperature was estimated to be in the range of 1000 – 2000 K, while the highest is at least > 5000 K.

Table 2.2: *Experimentally estimated temperature within collapsing cavitation bubble*

Experimental approach	Temperature range (K)	Reference
Single bubble sonoluminescence (SBSL) spectra	5000 – 50 000	[6,9]
EPR spin-trapping studies	1000 – 4600	[45]
(sonolysis of H_2O/D_2O mixtures)		
Comparative rate thermometry	1900 – 5200	[46]
Sonolysis of methane in argon saturated water	1930 – 2720	[47]
Sonolysis of t-butanol in water	2300 – 3600	[48]
Methyl radical recombination (MRR)	3700 - 6200	[49, 50]

To clarify such a broad range, Suslick et al. [46] suggested ,that there are at least two distinct areas, which should be considered: (i) the high temperature area (> 5000 K) – a gas phase zone within the collapsing cavitation bubble, and (ii) a relatively low temperature area(~ 1900 K) – a thin liquid layer that is surrounding the collapsing cavity. Thus, the accuracy of temperature determination depends on the sensitivity of a particular method that is being used [51, 52]. Even though, there are numerous reports about the magnitude for local cavitation induced areas of high temperature, it is still unclear, how the thermal energy propagates from the point of collapse to the proximity of the sonicated particle cavitation bubble.

2.3.2   *Free Radical Formation (Sonochemistry)*

Under extreme conditions (high T, P) [53] resulting from adiabatic cavitation bubble compression, generation of free radicals is observed [36, 37]. If ethanol, for example, is used as a sonication medium, highly reactive H· and ·CH_2OH free radicals will be produced during cavitation bubble collapse, which is one of the main origins of sonochemical reactions [54], making the collapse itself an essential part in the area of sonochemistry [55, 56]. Due to high reactive ability and short life time of generated free radicals, the variety of sonochemical reactions [57] may occur upon cavitation bubble collapse. **Table 2.3** provides examples of possible free radical formation upon bubble collapse with respect to the vapors which are present within the bubble [37].

Table 2.3: *Possible types of free radicals formed in the sonolysis of organic liquids and water [37]*

Sonication medium	Radical type
n-alkanes	$\cdot CH_2R$, $\cdot CHR_1R_2$
n-alcohols	$\cdot CH_2R$, $\cdot CHR_1R_2$, $\cdot CH_2OR$
Toluene	$\cdot CH_2$-phenyl
Dioxane, THF	$\cdot CH_2R$, $\cdot CH_2OR$
DMF	$\cdot CH_3$, $\cdot N(CH_3)R$, $\cdot CH_2N(CH_3)C(O)H$
DMA	$\cdot CH_3$, $\cdot CH_2N(CH_3)C(O)CH_3$
Water	$\cdot H$, $\cdot OH$

Thus, newly formed free radicals may serve as strong oxidants initiating red-ox reactions with species or solid particles present in sonication media [58]. They also may undergo recombination processes leading to new reactive species formation. Additionally, **Table 2.4** provides the experimentally determined number of observed radicals, photons, ions in a single cavitation bubble in water [59].

Table 2.4: *Quantitative sonochemistry in a single cavitation bubble at 52 kHz* [59].

| Conditions	22°C	3°C
Rmax, µm	28.9	30.5
Number of $\cdot OH$ radicals per cycle	6.6×10^5	8.2×10^5
Number of photons per cycle	8.1×10^3	7.5×10^4
Number of NO_2^- ions per cycle	3.7×10^6	9.9×10^6

Initiated by free radicals sonochemical reactions may occur at three different sites [60, 61]. One of them is within the actual cavitation bubble (the area with the highest temperature), another at the cavitation bubble / sonication medium interface (lower temperature conditions), and in the liquid region far from cavitation bubble (ambient temperature) (**Fig. 2.5**)
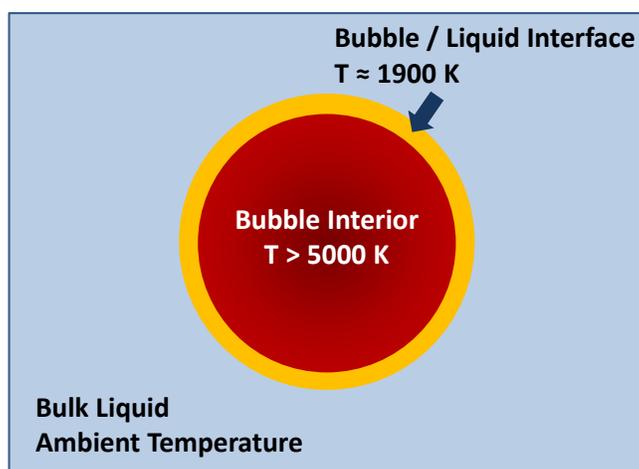
Fig. 2.5: *Sites within / around the cavitation bubble, where sonochemical reactions are taking place.*

2.4   Applications of Ultrasound

Depending on the frequency and power, acoustic irradiation can be used in various fields of research and industrial applications. For example, ultrasound in the megahertz frequency range can assist different sonochemical reactions. At the same time, the same ultrasound irradiation of lower power is ubiquitous for medical applications. **Fig. 2.6** schematically represents the main areas of ultrasound applications [62-72] such as chemical, surface processing, as well as medical and industrial (food).
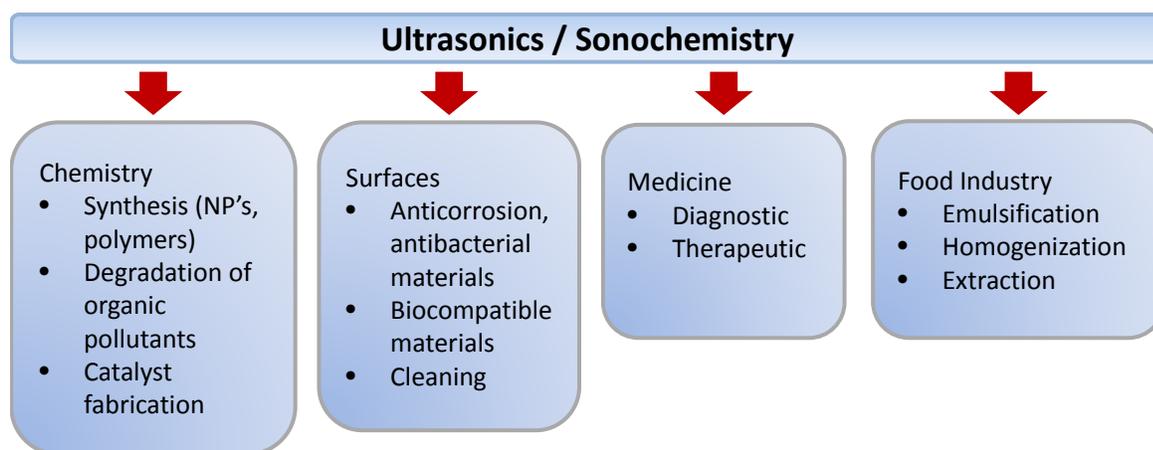

Fig. 2.6: *Major areas of ultrasound applications.*

2.5   Electrocatalytic Hydrogen Production

2.5.1   *Overview of the Electrocatalytic Hydrogen Formation Mechanism*

According to classical theory [73] the overall HER [74] on the metal electrocatalyst (M) surface in acidic media may proceed via several elementary steps (**Fig. 2.7**). First, a hydrogen-free surface of the electrocatalyst undergoes a primary discharge step defined as:

$$H_3O^+ + e^- \rightarrow M\text{-}H_{ads} + H_2O \qquad \text{(Volmer reaction)}$$

Generally, a primary discharged step leading to formation of adsorbed hydrogen (M-H_{ads}) is believed to be fast and followed by either a desorption step:

$$M\text{-}H_{ads} + H_3O^+ + e^- \rightarrow H_2 + M + H_2O \qquad \text{(Heyrovsky reaction)}$$

or a recombination step:

$$M\text{-}H_{ads} + M\text{-}H_{ads} \rightarrow H_2 + M \qquad \text{(Tafel reaction)}$$
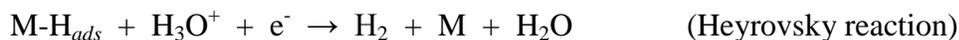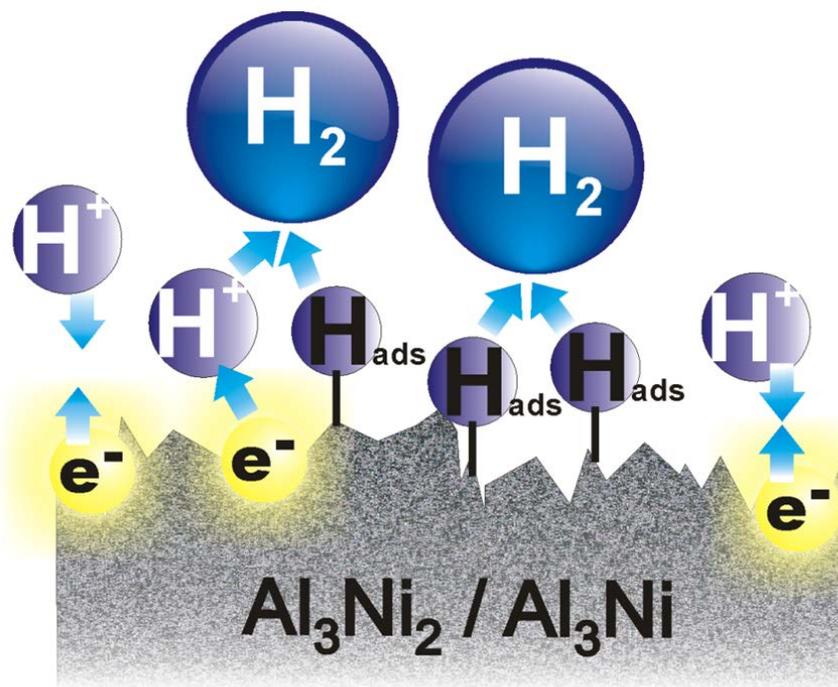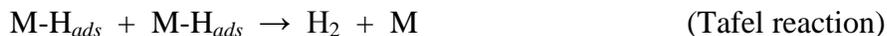
Fig. 2.7 *Schematic presentation of elementary steps involved in the electrocatalytic hydrogen formation process.*

Either one, Heyrovsky or Tafel reaction is considered to be a rate-limiting step. Thus, the HER mechanism may be represented as Volmer – Heyrovsky or Volmer – Tafel. Theoretically,the inherent property of the electrocatalyst such as the Tafel slope (b) arising from the Tafel equation:

$$\eta = b \log j + a,$$

where η is overpotential and j is current density, should be useful for revealing the actual rate-limiting step. Thus, evaluation of the linear part of the Tafel plot that fits to the Tafel equation should make it possible to determine the overall HER mechanism.

Tafel slope (b) for a primary discharge, desorption, and recombination steps are defined as following:

$$b = \frac{2.3RT}{\alpha F} \approx 120 \, mV \text{ (Volmer)}$$

$$b = \frac{2.3RT}{(1+\alpha)F} \approx 40 \, mV \text{ (Heyrovsky)}$$

$$b = \frac{2.3RT}{2F} \approx 30 \, mV \text{ (Tafel)}$$

where R is the ideal gas constant, T is the absolute temperature, α is the symmetry coefficient, and F is the Faraday constant. In principle, if analysis of the linear part of the Tafel plot results in the lower Tafel slope, this indicates that the electrocatalyst requires a lower overpotential to generate a reasonable current. Nevertheless, the Tafel plots should be interpreted cautiously, since the Tafel slope has a complex dependence on various parameters such as type of the catalyst, catalyst pre-activation, adsorption/desorption conditions to/from active sites, electrode modification, reaction pathway, etc. [75]. Another important parameter, which can be estimated from the Tafel plot, is the exchange current density (j_0), which is obtained from extrapolating the linear part of the Tafel plot to zero overpotential. (j_0) is an extremely valuable parameter representing the intrinsic rate of electron transfer between analyte and electrocatalyst [76].

2.5.2 Factors Defining the Efficiency of the Electrocatalytic Hydrogen Formation

Crystal Structure (Type and Orientation)

While developing the potential electrocatalytic system for water splitting, special attention should be given to its crystal structure and orientation on the surface (exposed edges). Based on the review of the existing electrocatalysts [77-81], the majority of the most promising materials, which could replace platinum, utilize trigonal/hexagonal crystal structure **Fig. 2.8**.
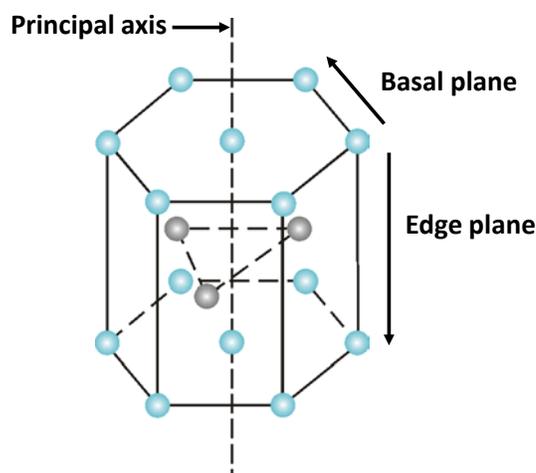
Fig. 2.8: *Hexagonal crystal system.*

It is well known that in a trigonal/hexagonal lattice system there is one unique axis (called principal axis) which allows distinguishing between edge (parallel to the principal axis) and basal (perpendicular to the principal axis) planes. It is believed that electrochemical reactions preferentially occur on the edge planes [82]. Based on the comprehensive reviews [83-86] much of the electrocatalytic activity is attributed to surface edge plane sites. Thus, it is highly recommended to consider the type of catalyst crystal structure as well as surface orientation of the active sites for creation of the electrocatalytically efficient HER material which could compete with platinum.

Surface Composition and Morphology

Undoubtedly, surface composition of the electrocatalyst plays a major role in defining its efficiency and potential use for HER. Formation/presence of any compounds which could possibly passivate the water splitting process is highly undesirable. For instance, earth abundant aluminum cannot be used for electrocatalysis simply due to the formation of a protecting/passivating layer of aluminum oxide/hydroxide [87]. Another issue, that can restrict an electrocatalyst from its use for HER, is the presence of an amorphous phase on its surface. An amorphous phase as being an irregular structure inhibits the process of hydrogen formation significantly [88]. Besides that, the surface of the prospective catalyst should preferably consist of stable/chemically inert compounds, which do not undergo oxidative dissolution or corrosion [89]. As a result, some initially promising electrocatalysts do not last and their efficiency drops drastically. In addition to surface composition, the morphology of the electrocatalyst is also one of the parameters that define the efficiency of hydrogen evolution. To date, there have been made numerous attempts to achieve the enhancement of the electrocatalytic water splitting process through the adjustment of catalyst's morphology [90-92]. Thus, the potential catalysts were synthesized in the form of nanoparticles, nanowires, or as a porous-like structure simply to increase the surface area of the active phase.

Even though it is believed that high surface area should enhance the catalytic activity of the material, in the area of electrocatalysis such an assumption may not be accurate. For example, the effective current output of a nickel nanowire based HER catalyst is lower than that of a planar nickel plate despite of its high surface area [90]. This can be explained in terms of limited HER active area. Clustered nanowire structures only allow vertical bubble escape which interferes with electrolyte inflow to the bottom of the nanowires. Therefore, hindered electrolyte transport significantly reduces the efficiency of the prospective electrocatalyst.

Additionally, porous structures may also inhibit the overall process of hydrogen production. In this case newly formed hydrogen bubbles are trapped within the pores and are considerably contributing to the electrolyte ohmic resistance, which results in noticeable catalytic HER activity loss [93]. With this in mind, it is important to consider full accessibility of the surface by an electrolyte rather than a high surface area, when creating an efficient electrocatalyst. This could be achieved, for instance, by impregnation of a prospective catalyst

in a well spread support that would prevent electrolyte inflow interruption or hydrogen bubble trapping.

Electrocatalyst Pre-Activation for Hydrogen Evolution

Often, as synthesized/fabricated catalytic materials do not perform well enough untill they are properly activated. Therefore, the process of activation is an important step in catalyst preparation, significantly increasing its catalytic ability. Many electrocatalysts require activation for efficient hydrogen production [94, 95].

According to the hydrogen evolution mechanism, the first step in HER is an adsorption of hydrogen to the surface of the electrocatalyst (Volmer discharge step). It is known that the first hydrogen bonds to the active site strongly, and cannot be easily removed as required by the HER mechanism. The phenomenon is taking place until the hydrogen coverage is reached (normally 0.25), specific for a particular catalyst [82]. Upon reaching the necessary coverage value, the free energy of adsorption is lowering allowing the rest of the hydrogen atoms to be able to adsorb with a significantly lower barrier, or, with respect to HER with a lower overpotential.

Thus, it would be desirable for a catalyst to possess the required hydrogen coverage before its use. This is normally achieved by purging hydrogen gas over the catalyst surface for an extended time of several hours, or sometimes even days [96]. Once activated and all requirements are met (crystal structure, surface composition, and morphology) the prospective catalyst should ideally perform at a lower overpotential and initiate a considerable current.

### 2.5.3   *Potential Electrocatalytically Active HER Systems*

Based on the results presented in the literature the most promising electrocatalysts are those that contain one or more transition metals such as molybdenum, tungsten, cobalt, and nickel. A summary of the existing electrocatalytically active hydrogen evolution reaction systems (compounds / composites / hybrids) is provided in **Table 2.5**.

Another class of compounds, which could be potentially active in the water splitting process, is nanoalloys [102-105]. However, up to now the efficiency of electrocatalysts that were prepared using nanoalloys was significantly lower as compared to Pt. Low efficiency of nanoalloys is most likely related to low accessibility of active centres for hydrogen.

Table 2.5: *Most common transition metal based catalysts for HER. The characteristics of Pt is given as a reference*

| Catalyst	Crystal structure/coordination	Exchange current density (i_0) mA/cm^2	Ref.
Pt	Cubic	2.2	[97]
MoS_2 nanoparticles on MGF	hexagonal	3.01×10^{-3}	[75]
Mo_2C nanoparticles on CNT	orthorhombic	0.014	[91]
MoP nanoparticles	hexagonal	0.086	[79]
Cu_2MoS_4	tetragonal	0.040	[98]
WC	hexagonal	6.8×10^{-4}	[78]
WO_3 nanorods	hexagonal	2.75×10^{-3}	[99]
WO_3 bulk	hexagonal	8.57×10^{-4}	[99]
WO_3 nanowires	hexagonal	6.61	[92]
WO_3 commercial	hexagonal	0.265	[92]
W2MoC	hexagonal	0.011	[77]
W4MoC	hexagonal	0.029	[77]
$CoSe_2$ nanoparticles on carbon fiber paper	cubic	4.9×10^{-3}	[97]
$CoSe_2$ film	cubic	5.9×10^{-5}	[97]
$Co_{0.6}Mo_{1.4}N_2$	trigonal/octahedral	0.23	[81]
$Co_{57}Ni_{43}$ alloy	-	0.048	[100]
$Co_{57.5}Ni_{36}Y_{6.5}$ alloy	-	0.067	[100]
$Co_{57}Ni_{35}Ce_8$ alloy	-	0.079	[100]
Ni nanowires	cubic	-	[90]
Ni_2P nanoparticles	hexagonal	0.49	[80]
NiS	hexagonal	-	[89]
Ni_3S_2	rhombohedral	-	[89]
Al_3Ni_2/Al_3Ni	hexagonal/orthorhombic	17	[101]

For this reason, recently, in order to enhance the efficiency of alloys for electrocatalysis, near-surface and surface alloys were proposed [106]. Near-surface alloys are characterized by different composition of surface layer and support [107-110]. Electrocatalytic properties of such alloys were demonstrated for a few systems that were prepared by the deposition-annealing procedure using transition metals and a Pt (111) surface [109]. **Fig. 2.9** provides an overview of near-surface alloys, for which interactions with hydrogen were quantified using density functional theory [106].
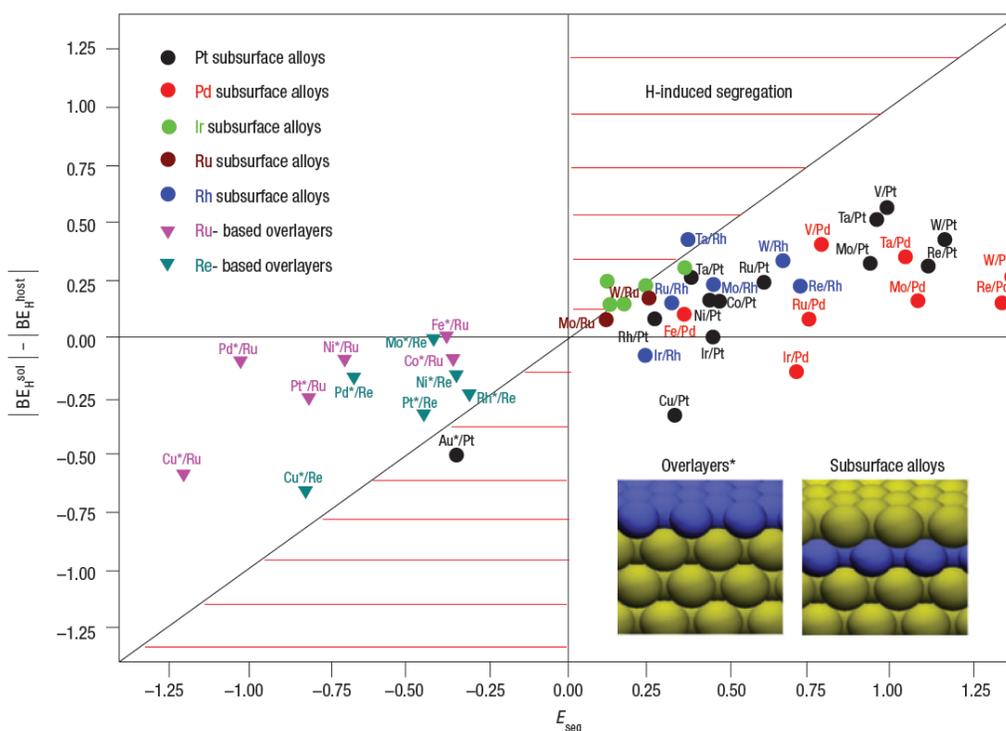
Fig. 2.9: *Stability of NSAs with respect to hydrogen-induced segregation. Metal alloys are denoted as solute/host pairs. The x axis indicates the energy (E_{seg}) for a single solute atom to move from the bulk to the surface layer of the host metal. The y axis denotes the difference between the magnitudes of the hydrogen binding energies (θ_H = 1/4 monolayer) on the pure solute ($|BE_H^{sol}|$) and on the pure host ($|BE_H^{host}|$) close-packed metal surfaces. Regions in which hydrogen-induced segregation is expected are hatched. The * symbol denotes overlayers; otherwise, subsurface alloys (see inset schematics) are present. The color code used for each class of NSAs, characterizing the host metal used for the class, is preserved in subsequent figures. Reprinted with permission from* [106]

The first attempts to avoid the use of expensive noble or rare transition metals for electrocatalyst fabrication were taken by Laisa et al. [111-113]. They have shown that heating of AlNi (50 wt.% Ni) (**Fig. 2.10**) powders above the melting point of Al increased the electrocatalytic activity of the samples due to stimulation of diffusion of Al into Ni. It has been also reported that the large surface roughness, grain sizes, and enrichment of hexagonal Al_3Ni_2 phase in the activated AlNi alloys could be responsible for the formation of efficient AlNi-based electrocatalysts, but this is still not well understood. In particular, as it can be seen from the Al-Ni binary alloy phase diagram [114], the composition of AlNi (50 wt.% Ni) is complex [115] and involves the presence of several phases: Al metal, Al_3Ni_2, and Al_3Ni intermetallics (**Fig. 2.10**).

Therefore, it is still debatable which phase or combination of phases is responsible for enhancement of electrocatalytic activity toward HER. Additionally, methods which were used for the catalyst activation (high temperature and pressure sintering, composite electrodeposition, and plasma spraying) are lengthy and complex.
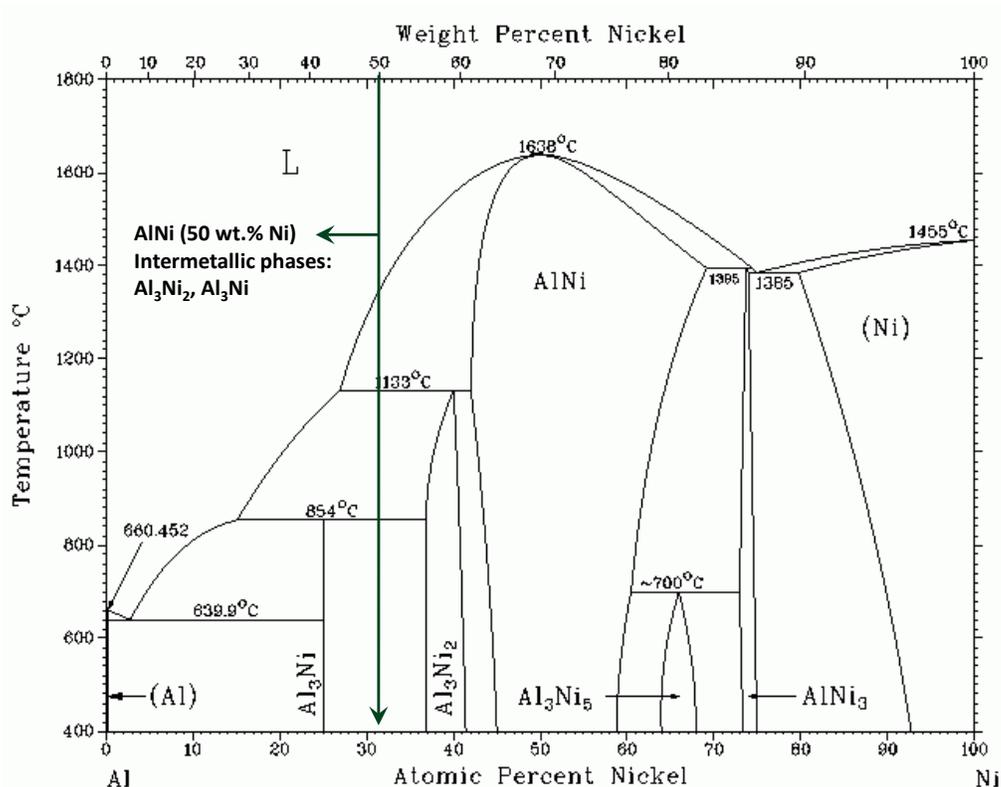

Fig. 2.10: *Al-Ni binary alloy phase diagram showing intermetallic composition at 50 wt.% Ni [114].*

Overall, there is a wide range of methods and materials that are used in order to fabricate/enhance the efficiency of electrocatalytic water splitting [77, 81, 92, 97, 99], except the sonochemical approach. Even though, the attempts to synthesize metal alloys using sonochemistry did take place [116], the resulting product could not be possibly used as electrocatalyst toward HER due to its amorphous structure. It is also known that the method of ultrasound treatment was used to assist various electrochemical reactions themselves [117-119], but untill now there have been no reports related to processing of metal alloys with high intensity ultrasound for enhancement of electrocatalytic properties toward HER.

2.6 Objectives of the Thesis

The flow chart below (**Fig. 2.11**) represents the key aspects, which are investigated during this study. Results reported here are focused on (i) compositional and morphological changes which solid matter (AlNi particles) undergoes during high intensity ultrasound treatment, (ii) providing insights into fundamental understanding of cavitation, and (iii) use of ultrasound treatment as a unique method for fabrication of the interface which possesses enhanced electrocatalytic properties for the water splitting process.
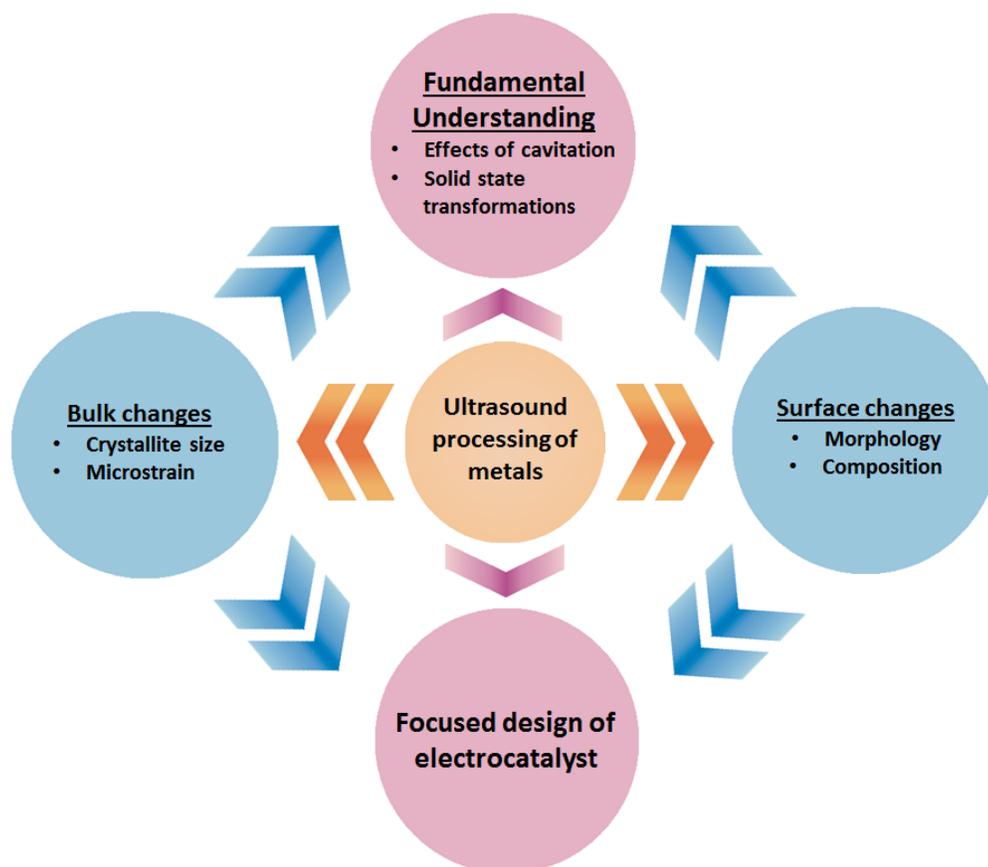
Fig. 2.11: *The flow chart representing key objectives of the thesis.*

Overall, the detailed evaluation of the ultrasonically driven bulk and surface changes in metal alloys is expected to provide essential fundamental knowledge on the phenomenon of cavitation and on the optimum electrocatalyst fabrication for hydrogen production.

References

[1] J.D.N. Cheeke, Fundamentals and applications of ultrasonic waves. , CRC Press, Boca Raton, 2002.

[2] L.E. Kinsler, A.R. Frey, A.B. Coppens, J.V. Sanders, Fundamentals of acoustics, Wiley, New York 1982

[3] O.V. Abramov, High-Intensity Ultrasound, Gordon and Breach Science Publishers, 1998.

[4] M.A. Margulis, Sonochemistry and Cavitation, Gordon and Breach Publishers, 1995.

[5] E.A. Neppiras, Acoustic cavitation, Physics Reports-Review Section of Physics Letters, 61 (1980) 159-251.

[6] F.R. Young, Cavitation, Imperial College, London, 1999.

[7] H. Maris, S. Balibar, Negative pressures and cavitation in liquid helium, Physics Today, 53 (2000) 29-34.

[8] K. Yasui, Fundamentals of Acoustic Cavitation and Sonochemistry, in: Pankaj, M. Ashokkumar (Eds.) Theoretical and Experimental Sonochemistry Involving Inorganic Systems, 2011, pp. 1-29.

[9] T.G. Leighton, The acoustic bubble, Academic Press, London 1994

[10] B.M. Borkent, M. Arora, C.-D. Ohl, N. De Jong, M. Versluis, D. Lohse, K.A. Morch, E. Klaseboer, B.C. Khoo, The acceleration of solid particles subjected to cavitation nucleation, Journal of Fluid Mechanics, 610 (2008) 157-182.

[11] S.I. Madanshetty, R.E. Apfel, Acoustic microcavitation – enhancement and applications, Journal of the Acoustical Society of America, 90 (1991) 1508-1514.

[12] D.E. Yount, E.W. Gillary, D.C. Hoffman, A microscopic investigation of bubble formation nuclei, Journal of the Acoustical Society of America, 76 (1984) 1511-1521.

[13] N. Bremond, M. Arora, S.M. Dammer, D. Lohse, Interaction of cavitation bubbles on a wall, Physics of Fluids, 18 (2006).

[14] E. Wang, W. Chen, M. Lu, R. Wei, Bubble oscillations driven by aspherical ultrasound in liquid, Journal of the Acoustical Society of America, 114 (2003) 1898–1904

[15] K. Yasui, Influence of ultrasonic frequency on multibubble sonoluminescence, Journal of the Acoustical Society of America, 112 (2002) 1405-1413.

[16] J. Lee, T. Tuziuti, K. Yasui, S. Kentish, F. Grieser, M. Ashokkumar, Y. Iida, Influence of surface-active solutes on the coalescence, clustering, and fragmentation of acoustic bubbles confined in a microspace, Journal of Physical Chemistry C, 111 (2007) 19015-19023.

[17] Y. Iida, M. Ashokkumar, T. Tuziuti, T. Kozuka, K. Yasui, A. Towata, J. Lee, Bubble population phenomena in sonochernical reactor: II. Estimation of bubble size distribution and its number density by simple coalescence model calculation, Ultrasonics Sonochemistry, 17 (2010) 480-486.

[18] O. Louisnard, F. Gomez, Growth by rectified diffusion of strongly acoustically forced gas bubbles in nearly saturated liquids, Physical Review E, 67 (2003).

[19] J. Lee, S. Kentish, M. Ashokkumar, Effect of surfactants on the rate of growth of an air bubble by rectified diffusion, Journal of Physical Chemistry B, 109 (2005) 14595-14598.

[20] L.A. Crum, Measurements of the growth of air bubbles by rectified diffusion, Journal of the Acoustical Society of America, 68 (1980) 203-211.

[21] R. Mettin, Bubble structures in acoustic cavitation, in: D.A. A. (Ed.) Bubble and particle dynamics in acoustic fields: modern trends and applications, Research Signpost, Trivandrum, 2005, pp. 1-36.

[22] H. Mitome, T. Kozuka, T. Tuziuti, L. Wang, Quasi acoustic streaming induced by generation of cavitation bubbles, 1997.

[23] R. Mettin, I. Akhatov, U. Parlitz, C.D. Ohl, W. Lauterborn, Bjerknes forces between small cavitation bubbles in a strong acoustic held, Physical Review E, 56 (1997) 2924-2931.

[24] K. Yasui, T. Tuziuti, J. Lee, T. Kozuka, A. Towata, Y. Iida, The range of ambient radius for an active bubble in sonoluminescence and sonochemical reactions, Journal of Chemical Physics, 128 (2008).

[25] F. Burdin, N.A. Tsochatzidis, P. Guiraud, A.M. Wilhelm, H. Delmas, Characterisation of the acoustic cavitation cloud by two laser techniques, Ultrasonics Sonochemistry, 6 (1999) 43-51.

[26] W.S. Chen, T.J. Matula, L.A. Crum, The disappearance of ultrasound contrast bubbles: Observations of bubble dissolution and cavitation nucleation, Ultrasound in Medicine and Biology, 28 (2002) 793-803.

[27] N.A. Tsochatzidis, P. Guiraud, A.M. Wilhelm, H. Delmas, Determination of velocity, size and concentration of ultrasonic cavitation bubbles by the phase-Doppler technique, Chemical Engineering Science, 56 (2001) 1831-1840.

[28] J. Lee, M. Ashokkumar, S. Kentish, F. Grieser, Determination of the size distribution of sonoluminescence bubbles in a pulsed acoustic field, Journal of the American Chemical Society, 127 (2005) 16810-16811.

[29] M. Ashokkumar, The characterization of acoustic cavitation bubbles - An overview, Ultrasonics Sonochemistry, 18 (2011) 864-872.

[30] R. Tronson, M. Ashokkumar, F. Grieser, Comparison of the effects of water-soluble solutes on multibubble sonoluminescence generated in aqueous solutions by 20-and 515-kHz pulsed ultrasound, Journal of Physical Chemistry B, 106 (2002) 11064-11068.

[31] D. Sunartio, M. Ashokkumar, F. Grieser, Study of the coalescence of acoustic bubbles as a function of frequency, power, and water-soluble additives, Journal of the American Chemical Society, 129 (2007) 6031-6036.

[32] R. Tronson, M. Ashokkumar, F. Grieser, Multibubble sonoluminescence from aqueous solutions containing mixtures of surface active solutes, Journal of Physical Chemistry B, 107 (2003) 7307-7311.

[33] M.P. Brenner, S. Hilgenfeldt, D. Lohse, Single-bubble sonoluminescence, Reviews of Modern Physics, 74 (2002) 425-484.

[34] K. Yasui, T. Tuziuti, M. Sivakumar, Y. Iida, Theoretical study of single-bubble sonochemistry, Journal of Chemical Physics, 122 (2005).

[35] K.S. Suslick, Ultrasound its Chemical Physical and Biological Effects, 1988.

36[] L. Stricker, D. Lohse, Radical production inside an acoustically driven microbubble, Ultrasonics Sonochemistry, 21 (2014) 336-345.

[37] V. Misik, P. Riesz, EPR study of free radicals induced by ultrasound in organic liquids .2. Probing the temperatures of cavitation regions, Ultrasonics Sonochemistry, 3 (1996) 25-37.

[38] R. Pecha, B. Gompf, Microimplosions: Cavitation collapse and shock wave emission on a nanosecond time scale, Physical Review Letters, 84 (2000) 1328-1330.

[39] K. S. Suslick, L.A. Crum, Sonochemistry and Sonoluminescence in: M.J. Crocker (Ed.) Encyclopedia of Acoustics, John Wiley & Sons, 1997, pp. 271-282.

[40] T.J. Matula, Inertial cavitation and single-bubble sonoluminescence, Philosophical Transactions of the Royal Society a-Mathematical Physical and Engineering Sciences, 357 (1999) 225-249.

[41] A. Henglein, R. Ulrich, J. Lilie, Luminescence and chemical action by pulsed ultrasound, Journal of the American Chemical Society, 111 (1989) 1974-1979.

[42] T. Prozorov, R. Prozorov, K.S. Suslick, High velocity interparticle collisions driven by ultrasound, Journal of the American Chemical Society, 126 (2004) 13890-13891.

[43] S. Merouani, O. Hamdaoui, Y. Rezgui, M. Guemini, Theoretical estimation of the temperature and pressure within collapsing acoustical bubbles, Ultrasonics Sonochemistry, 21 (2014) 53-59.

[44] M. Ashokkumar, T. Mason, Sonochemistry, in: Kirk-Othmer Encylcopedia of Chemical Technology, John Wiley & Sons, 2007.

[45] V. Misik, N. Miyoshi, P. Riesz, EPR spin-trapping of the sonolysis of H2O/D2O mixtures: probing the temperatures of cavitation regions, Journal of Physical Chemistry, 99 (1995) 3605-3611.

[46] K.S. Suslick, D.A. Hammerton, R.E. Cline, The sonochemical hot-spot, Journal of the American Chemical Society, 108 (1986) 5641-5642.

[47] E.J. Hart, C.H. Fischer, A. Henglein, Sonolysis of hydrocarbons in aqueous solution, Radiation Physics and Chemistry, 36 (1990) 511-516.

[48] A. Tauber, G. Mark, H.P. Schuchmann, C. von Sonntag, Sonolysis of tert-butyl alcohol in aqueous solution, Journal of the Chemical Society-Perkin Transactions 2, (1999) 1129-1135.

[49] M. Ashokkumar, F. Grieser, A comparison between multibubble sonoluminescence intensity and the temperature within cavitation bubbles, Journal of the American Chemical Society, 127 (2005) 5326-5327.

[50] J. Rae, M. Ashokkumar, O. Eulaerts, C. Von Sonntag, J. Reisse, F. Grieser, Estimation of ultrasound induced cavitation bubble temperatures in aqueous solutions, Ultrason. Sonochem. 12 (2005) 325–329.

[51] D. Radziuk, H. Moehwald, K. Suslick, Single bubble perturbation in cavitation proximity of solid glass: hot spot versus distance, Physical Chemistry Chemical Physics, 16 (2014) 3534-3541.

[52] K. Okitsu, T. Suzuki, N. Takenaka, H. Bandow, R. Nishimura, Y. Maeda, Acoustic multibubble cavitation in water: A new aspect of the effect of a rare gas atmosphere on bubble temperature and its relevance to sonochemistry, Journal of Physical Chemistry B, 110 (2006) 20081-20084.

[53] G.L. Chahine et al., Modeling of surface cleaning by cavitation bubble dynamics and collapse, Ultrasonics Sonochemistry. (2015), http://dx.doi.org/10.1016/j.ultsonch.2015.04.026

[54] S. Merouani, O. Hamdaoui, Y. Rezgui, M. Guemini, Computer simulation of chemical reactions occurring in collapsing acoustical bubble: dependence of free radicals production on operational conditions, Res Chem Intermed, 41 (2015) 881-897.

[55] K.S. Suslick, Mechanochemistry and sonochemistry: concluding remarks, Faraday Discussions, 170 (2014) 411-422.

[56] F. Grieser, M. Ashokkumar, J.Z. Sostaric, Sonochemistry and sonoluminescence in colloidal systems, in: L.A. Crum, T.J. Mason, J.L. Reisse, K.S. Suslick (Eds.) Sonochemistry and Sonoluminescence, 1999, pp. 345-362.

[57] T.J. Mason, Recent advances in sonochemistry and processing, Acta Physica Sinica-Overseas Edition, 8 (1999) S313-S318.

[58] J. Dulle, S. Nemeth, E.V. Skorb, T. Irrgang, J. Senker, R. Kempe, A. Fery, D.V. Andreeva, Sonochemical Activation of Al/Ni Hydrogenation Catalyst, Advanced Functional Materials, 22 (2012) 3128-3135.

[59] Y.T. Didenko, K.S. Suslick, The energy efficiency of formation of photons, radicals and ions during single-bubble cavitation, Nature, 418 (2002) 394-397.

[60] K. Yasui, Variation of liquid temperature at bubble wall near the sonoluminescence threshold, Journal of the Physical Society of Japan, 65 (1996) 2830-2840.

[61] J.P. Lorimer, T.J. Mason, Sonochemistry. Part 1-The physical aspects, Chemical Society Reviews, 16 (1987) 239-274.

[62] T.J. Mason, E.D. Cordemans, Ultrasonic intensification of chemical processing and related operations: A review, Chemical Engineering Research & Design, 74 (1996) 511-516.

[63] G. Price, Current Trends in Sonochemistry, RSC, Cambridge, UK, 1992.

[64] S. Muthukumaran, S.E. Kentish, G.W. Stevens, M. Ashokkumar, Application of ultrasound in membrane separation processes: A review, Reviews in Chemical Engineering, 22 (2006) 155-194.

[65] M. Ashokkumar, Sonochemical synthesis of inorganic nanoparticles, in: P.D. Cozzoli (Ed.) Advanced Wet-Chemical Synthetic Approaches to Inorganic Nanostructures, Transworld Research Network, 2008, pp. 107-131.

[66] T.J. Mason, C. Petrier, in: S. Parsons (Ed.), Advanced Oxidation Processes for Water and Wastewater Treatment, IWA Publishing, 2004, pp. 185–208.

[67] D.J. McClements, Advances in the applications of ultrasound in food analysis and processing, Trends in Food Science & Technology, 6 (1995) 293-299.

[68] F. Cavalieri, M. Zhou, M. Ashokkumar, The Design of Multifunctional Microbubbles for Ultrasound Image-Guided Cancer Therapy, Current Topics in Medicinal Chemistry, 10 (2010) 1198-1210.

[69] E.V. Skorb, O. Baidukova, O. Andreeva, P.V. Cherepanov, D.V. Andreeva, Formation of polypyrrole/metal hybrid interfacial layer with self-regulation functions via ultrasonication, Bioinspired, Biomimetic and Nanobiomaterials, 2(3) (2013) 123-129.

[70] J. Schaeferhans, S. Gomez-Quero, D.V. Andreeva, G. Rothenberg, Novel and Effective Copper-Aluminum Propane Dehydrogenation Catalysts, Chemistry-a European Journal, 17 (2011) 12254-12256.

[71] E.V. Skorb, H. Moehwald, T. Irrgang, A. Fery, D.V. Andreeva, Ultrasound-assisted design of metal nanocomposites, Chemical Communications, 46 (2010) 7897-7899.

[72] N. Pazos-Perez, J. Schaeferhans, E.V. Skorb, A. Fery, D.V. Andreeva, Ultrasound driven formation of metal-supported nanocatalysts, Microporous and Mesoporous Materials, 154 (2012) 164-169.

[73] B.E. Conway, B.V. Tilak, Interfacial processes involving electrocatalytic evolution and oxidation of H-2, and the role of chemisorbed H, Electrochimica Acta, 47 (2002) 3571-3594.

[74] W. Lubitz, B. Tumas, Hydrogen: an overview, Chemical Reviews, 107 (2007) 3900-3903

[75] L. Liao, J. Zhu, X. Bian, L. Zhu, M.D. Scanlon, H.H. Girault, B. Liu, MoS2 Formed on Mesoporous Graphene as a Highly Active Catalyst for Hydrogen Evolution, Advanced Functional Materials, 23 (2013) 5326-5333.

[76] Atkins P, Paula JD (2002) Atkins' Physical Chemistry , 7th Ed. Oxford University , UK

[77] P. Xiao, X. Ge, H. Wang, Z. Liu, A. Fisher, X. Wang, Novel Molybdenum Carbide-Tungsten Carbide Composite Nanowires and Their Electrochemical Activation for Efficient and Stable Hydrogen Evolution, Advanced Functional Materials, 25 (2015) 1520-1526.

[78] F. Harnisch, G. Sievers, U. Schroeder, Tungsten carbide as electrocatalyst for the hydrogen evolution reaction in pH neutral electrolyte solutions, Applied Catalysis B-Environmental, 89 (2009) 455-458.

[79] Z. Xing, Q. Liu, A.M. Asiri, X. Sun, Closely Interconnected Network of Molybdenum Phosphide Nanoparticles: A Highly Efficient Electrocatalyst for Generating Hydrogen from Water, Advanced Materials, 26 (2014) 5702-5707.

[80] E.J. Popczun, J.R. McKone, C.G. Read, A.J. Biacchi, A.M. Wiltrout, N.S. Lewis, R.E. Schaak, Nanostructured Nickel Phosphide as an Electrocatalyst for the Hydrogen Evolution Reaction, Journal of the American Chemical Society, 135 (2013) 9267-9270.

[81] B. Cao, G.M. Veith, J.C. Neuefeind, R.R. Adzic, P.G. Khalifah, Mixed Close-Packed Cobalt Molybdenum Nitrides as Non-noble Metal Electrocatalysts for the Hydrogen Evolution Reaction, Journal of the American Chemical Society, 135 (2013) 19186-19192.

[82] T.F. Jaramillo, K.P. Jorgensen, J. Bonde, J.H. Nielsen, S. Horch, I. Chorkendorff, Identification of active edge sites for electrochemical H-2 evolution from MoS2 nanocatalysts, Science, 317 (2007) 100-102.

[83] C.E. Banks, T.J. Davies, G.G. Wildgoose, R.G. Compton, Electrocatalysis at graphite and carbon nanotube modified electrodes: edge-plane sites and tube ends are the reactive sites, Chemical Communications, (2005) 829-841.

[84] J. Kibsgaard, T.F. Jaramillo, F. Besenbacher, Building an appropriate active-site motif into a hydrogen-evolution catalyst with thiomolybdate Mo3S13 (2-) clusters, Nature Chemistry, 6 (2014) 248-253.

[85] B. Hinnemann, P.G. Moses, J. Bonde, K.P. Jorgensen, J.H. Nielsen, S. Horch, I. Chorkendorff, J.K. Norskov, Biornimetic hydrogen evolution: MoS2 nanoparticles as catalyst for hydrogen evolution, Journal of the American Chemical Society, 127 (2005) 5308-5309.

[86] W. Yuan, Y. Zhou, Y. Li, C. Li, H. Peng, J. Zhang, Z. Liu, L. Dai, G. Shi, The edge- and basal-plane-specific electrochemistry of a single-layer graphene sheet, Scientific Reports, 3 (2013).

[87] P.V. Cherepanov, M. Ashokkumar, D.V. Andreeva, Ultrasound assisted formation of Al-Ni electrocatalyst for hydrogen evolution, Ultrasonics Sonochemistry, 23 (2015) 142-147.

[88] L. Mihailov, T. Spassov, M. Bojinov, Effect of microstructure on the electrocatalytic activity for hydrogen evolution of amorphous and nanocrystalline Zr-Ni alloys, International Journal of Hydrogen Energy, 37 (2012) 10499-10506.

[89] D.Y. Chung, J.W. Han, D.-H. Lim, J.-H. Jo, S.J. Yoo, H. Lee, Y.-E. Sung, Structure dependent active sites of NixSy as electrocatalysts for hydrogen evolution reaction, Nanoscale, 7 (2015) 5157-5163.

[90] P.-C. Chen, Y.-M. Chang, P.-W. Wu, Y.-F. Chiu, Fabrication of Ni nanowires for hydrogen evolution reaction in a neutral electrolyte, International Journal of Hydrogen Energy, 34 (2009) 6596-6602.

[91] W.-F. Chen, J.T. Muckerman, E. Fujita, Recent developments in transition metal carbides and nitrides as hydrogen evolution electrocatalysts, Chemical Communications, 49 (2013) 8896-8909.

[92] A. Phuruangrat, D.J. Ham, S.J. Hong, S. Thongtem, J.S. Lee, Synthesis of hexagonal WO3 nanowires by microwave-assisted hydrothermal method and their electrocatalytic activities for hydrogen evolution reaction, Journal of Materials Chemistry, 20 (2010) 1683-1690.

[93] D. Kiuchi, H. Matsushima, Y. Fukunaka, K. Kuribayashi, Ohmic resistance measurement of bubble froth layer in water electrolysis under microgravity, Journal of the Electrochemical Society, 153 (2006) E138-E143.

[94] S.M.A. Shibli, J.N. Sebeelamol, Development of Fe2O3-TiO2 mixed oxide incorporated Ni-P coating for electrocatalytic hydrogen evolution reaction, International Journal of Hydrogen Energy, 38 (2013) 2271-2282.

[95] C. Lupi, A. Dell'Era, M. Pasquali, In situ activation with Mo of Ni-Co alloys for hydrogen evolution reaction, International Journal of Hydrogen Energy, 39 (2014) 1932-1940.

[96] Y.-H. Chang, C.-T. Lin, T.-Y. Chen, C.-L. Hsu, Y.-H. Lee, W. Zhang, K.-H. Wei, L.-J. Li, Highly Efficient Electrocatalytic Hydrogen Production by MoSx Grown on Graphene-Protected 3D Ni Foams, Advanced Materials, 25 (2013) 756-760.

[97] D. Kong, H. Wang, Z. Lu, Y. Cui, CoSe2 Nanoparticles Grown on Carbon Fiber Paper: An Efficient and Stable Electrocatalyst for Hydrogen Evolution Reaction, J. Am. Chem. Soc. 136 (2014) 4897-4900.

[98] P.D. Tran, N. Mai, S.S. Pramana, A. Bhattacharjee, S.Y. Chiam, J. Fize, M.J. Field, V. Artero, L.H. Wong, J. Loo, J. Barber, Copper molybdenum sulfide: a new efficient electrocatalyst for hydrogen production from water, Energy & Environmental Science, 5 (2012) 8912-8916.

[99] J. Rajeswari, P.S. Kishore, B. Viswanathan, T.K. Varadarajan, Facile Hydrogen Evolution Reaction on WO3 Nanorods, Nanoscale Res. Lett., 2 (2007) 496-503.

[100] F. Rosalbino, S. Delsante, G. Borzone, E. Angelini, Electrocatalytic behaviour of Co-Ni-R (R = Rare earth metal) crystalline alloys as electrode materials for hydrogen evolution reaction in alkaline medium, International Journal of Hydrogen Energy, 33 (2008) 6696-6703.

[101] P.V. Cherepanov, I. Melnyk, E.V. Skorb, P. Fratzl, E. Zolotoyabko, N. Dubrovinskaia, L. Dubrovinsky, Y.S. Avadhut, J. Senker, L. Leppert, S. Kuemmel, D.V. Andreeva, The use of ultrasonic cavitation for near-surface structuring of robust and low-cost AlNi catalysts for hydrogen production, Green Chemistry, 17 (2015) 2745-2749.

[102] R. Ferrando, J. Jellinek, R.L. Johnston, Nanoalloys: From theory to applications of alloy clusters and nanoparticles, Chemical Reviews, 108 (2008) 845-910.

[103] B.M. Munoz-Flores, B.I. Kharisov, V.M. Jimenez-Perez, P.E. Martinez, S.T. Lopez, Recent Advances in the Synthesis and Main Applications of Metallic Nanoalloys, Industrial & Engineering Chemistry Research, 50 (2011) 7705-7721.

[104] B.Y. Xia, H.B. Wu, N. Li, Y. Yan, X.W. Lou, X. Wang, One-Pot Synthesis of Pt-Co Alloy Nanowire Assemblies with Tunable Composition and Enhanced Electrocatalytic Properties, Angewandte Chemie-International Edition, 54 (2015) 3797-3801.

[105] J. Wilcoxon, Optical Absorption Properties of Dispersed Gold and Silver Alloy Nanoparticles, Journal of Physical Chemistry B, 113 (2009) 2647-2656.

[106] J. Greeley, M. Mavrikakis, Alloy catalysts designed from first principles, Nature Materials, 3 (2004) 810-815.

[107] C. Chen, Y. Kang, Z. Huo, Z. Zhu, W. Huang, H.L. Xin, J.D. Snyder, D. Li, J.A. Herron, M. Mavrikakis, M. Chi, K.L. More, Y. Li, N.M. Markovic, G.A. Somorjai, P. Yang, V.R. Stamenkovic, Highly Crystalline Multimetallic Nanoframes with Three-Dimensional Electrocatalytic Surfaces, Science, 343 (2014) 1339-1343.

[108] V.R. Stamenkovic, B.S. Mun, K.J.J. Mayrhofer, P.N. Ross, N.M. Markovic, Effect of surface composition on electronic structure, stability, and electrocatalytic properties of Pt-transition metal alloys: Pt-skin versus Pt-skeleton surfaces, Journal of the American Chemical Society, 128 (2006) 8813-8819.

[109] V.R. Stamenkovic, B. Fowler, B.S. Mun, G. Wang, P.N. Ross, C.A. Lucas, N.M. Markovic, Improved oxygen reduction activity on Pt3Ni(111) via increased surface site availability, Science, 315 (2007) 493-497.

[110] Y. Mizukoshi, T. Fujimoto, Y. Nagata, R. Oshima, Y. Maeda, Characterization and catalytic activity of core-shell structured gold/palladium bimetallic nanoparticles synthesized by the sonochemical method, Journal of Physical Chemistry B, 104 (2000) 6028-6032.

[111] P. Los, A. Rami, A. Lasia, Hydrogen evolution reaction on Ni-Al electrodes, J. Appl. Electrochem., 23 (1993) 135-140.

[112] A. Rami, A. Lasia, Kinetics of hydrogen evolution on Ni-Al alloy electrodes, J. Appl. Electrochem., 22 (1992) 376-382.

[113] D. Miousse, A. Lasia, V. Borck, Hydrogen evolution reaction on Ni-Al-Mo and Ni-Al electrodes prepared by low-pressure plasma spraying, J. Appl. Electrochem., 25 (1995) 592-602.

[114] Y. Du, N. Clavaguera, Thermodynamic assessment of the Al-Ni system, Journal of Alloys and Compounds, 237 (1996) 20-32.

[115] A. Ilbagi, P.D. Khatibi, I.P. Swainson, G. Reinhart, H. Henein, Microstructural analysis of rapidly solidified aluminium-nickel alloys, Can. Metall. Q., 50 (2011) 295-302

[116] K.S. Suslick, T.W. Hyeon, M.M. Fang, Nanostructured materials generated by high-intensity ultrasound: Sonochemical synthesis and catalytic studies, Chemistry of Materials, 8 (1996) 2172-2179.

[117] A. Lindermeir, C. Horst, U. Hoffmann, Ultrasound assisted electrochemical oxidation of substituted toluenes, Ultrasonics Sonochemistry, 10 (2003) 223-229.

[118] V. Mancier, A.-L. Daltin, D. Leclercq, Synthesis and characterization of copper oxide (I) nanoparticles produced by pulsed sonoelectrochemistry, Ultrasonics Sonochemistry, 15 (2008) 157-163.

[119] B. Thokchom, K. Kim, J. Park, J. Khim, Ultrasonically enhanced electrochemical oxidation of ibuprofen, Ultrasonics Sonochemistry, 22 (2015) 429-436.

3 Overview of the Thesis

This thesis consists of four individual publications presented in chapters 4 – 7.

The first part (Chapter 4) reveals changes in the bulk properties of AlNi alloy particles caused by high intensity ultrasound treatment. Specifically, due to solid state atomic diffusion, changes in crystallographic parameters such as crystallite size and microstrain of the intermetallic phases present in the alloy particles are demonstrated.

Further, in the second part (Chapter 5), sonomechanical aspects of acoustic cavitation are explained. Namely, the energetic impact of collapsed cavitation bubbles with respect to physical properties (vapor pressure, viscosity) of the sonication media used during the alloy particle treatment is assessed. Additionally, the effect of acoustically induced interparticle collisions on bulk changes is demonstrated by varying the particle concentration, as well as a new term such as the average minimum temperature of the sonicated particle ($\overline{T}^{min}_{particle}$) is introduced.

Furthermore, ultrasound assisted surface morphology and compositional changes (red-ox reactions, phase transformations) are demonstrated in Chapters 6 – 7. The principles of fabrication of the desirable interface explained here is used to demonstrate the way in which acoustic cavitation can be successfully utilized for creation of robust and highly efficient electrocatalysts for hydrogen production.

The summary of the main results is presented below.

3.1 Evidence for Ultrasonically Induced Solid State Atomic Diffusion in Metal Alloys

The direct indication of solid state atomic diffusion in metals and metal alloys is crystallite growth and, accordingly, grain boundary area reduction [1]. Thus, at the first stage we evaluated the effect of HIUS on crystallographic properties such as crystallite size and microstrain. For that reason AlNi (50 wt.% Ni) alloy particles were treated with HIUS in ethanol and analyzed with help of powder X-ray diffraction and transmission electron microscopy.

Ethanol was chosen as a sonication medium to eliminate various possible effects of sonication such as particle fragmentation, change of surface roughness and surface composition. Analysis of PXRD patterns of initial and HIUS treated (in ethanol) AlNi alloy particles indicated no difference in terms of composition (**Fig. 3.1a**): Al_3Ni_2 and Al_3Ni intermetallic phases [2] are present in both samples. Nevertheless, it is clearly seen that the reflection peaks after sonication become sharper/ narrower, which serves as a direct indication of crystallite size change. To estimate the crystallite size of the intermetallic phases we applied two approaches to the analysis of the PXRD patterns: Scherrer and Williamson – Hall (WH) [3, 4]. Scherrer analysis is used to evaluate the crystallite size with respect to a particular reflecting plane, while the WH method allows estimation of the size as well as strain-induced peak broadening [5], that is arising from crystal imperfections and distortion.
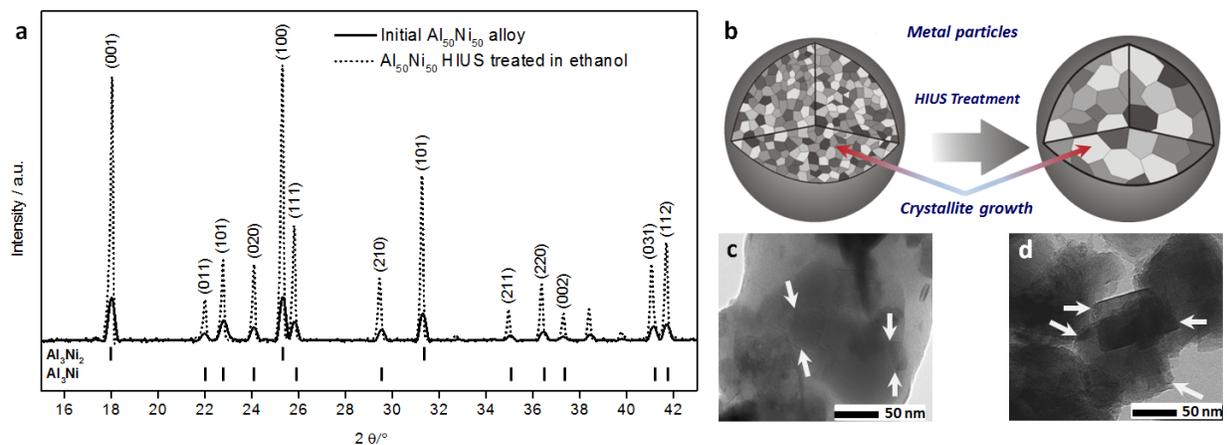
Fig. 3.1: *The XRD patterns of initial and HIUS treated (in organic solvents) AlNi (50wt% Ni) alloys (a); schematic representation of intermetallic crystallite growth (b); TEM images of initial (c) and HIUS treated (in ethanol) (d) AlNi (50wt% Ni) alloy.*

The obtained data from PXRD and TEM analysis indicate that intensive sonication of solid particles leads to Al_3Ni_2 and Al_3Ni crystallite growth as well as microstrain reduction (**Fig. 3.1b-d**). Thus, HIUS is capable of enhancing the process of solid state atomic diffusion within the metal alloy particles due to sonomechanical [6] (shock waves, interparticle collisions) effects of cavitation.

3.2 Regulation of Metal Alloy Bulk Microstructure by the Sonication Medium

Upon careful evaluation of PXRD patterns (Williamson – Hall analysis) for the ultrasonically treated samples we observed a gradual increase in crystallites size. Specifically, the crystallite size of Al_3Ni_2 intermetallic phase is increasing in the row: 95 nm (ethylene glycol) < 130 nm (ethanol) < 200 nm (water) < 225 nm (decane) (**Fig.3.2b**). Thus, an acoustically induced temperature gradient accelerates solid state atomic diffusion differently depending on the physical properties of sonication media such as vapor pressure and viscosity. These properties significantly affect the temperature inside the cavitation bubble and the strength of its collapse [7].
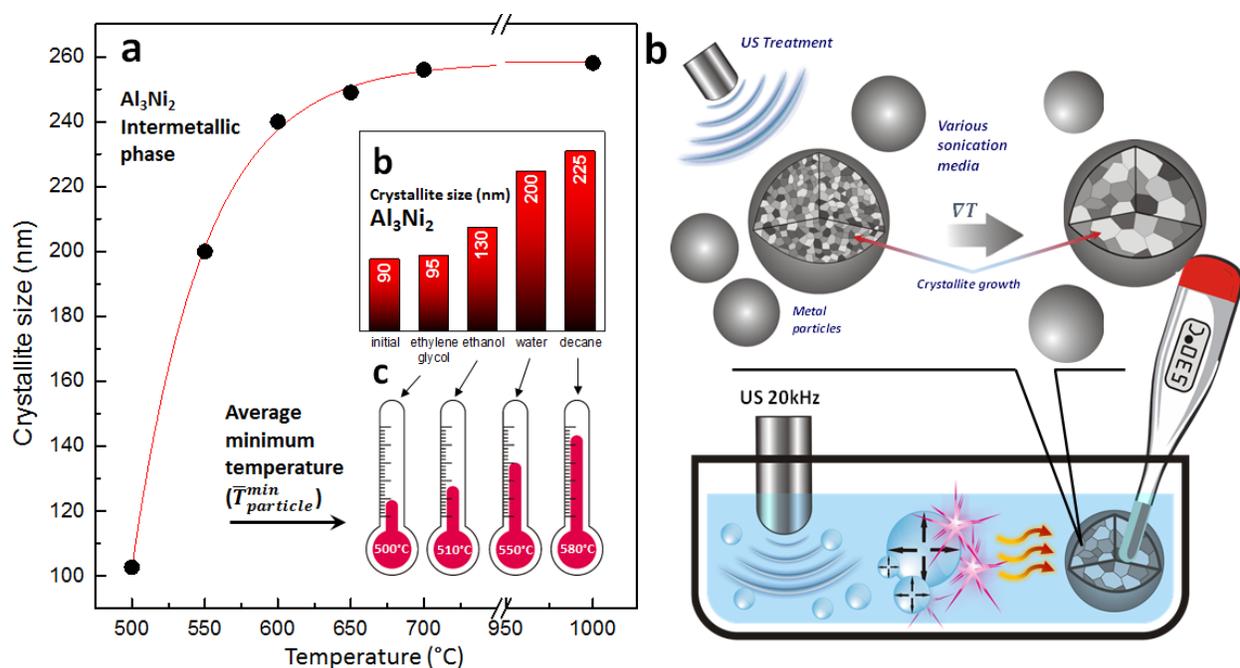
Fig. 3.2: *Al_3Ni_2 intermetallic phase crystallite size after annealing AlNi particles for 1 hour at different temperature (a). Al_3Ni_2 intermetallic phase crystallite size after 1 hour of HIUS treatment (b) and estimated ($\bar{T}^{min}_{particle}$) (c) in various sonication media. Schematic representation of Al_3Ni_2 crystallite change in AlNi particles upon HIUS treatment and energy transfer between collapsing cavitation bubbles and sonicated matter (d).*

Therefore, the thermal effect of cavitation bubble collapse on sonicated matter varies according to sonication medium. In order to calibrate the thermal effect of acoustic cavitation the metal particles were annealed for 1 hour at various temperatures and their crystallite size was calculated (**Fig. 3.2a**). Using a crystallite size vs. temperature plot as a calibration curve we

estimated the minimum average temperature up to which HIUS can heat the particle $(\bar{T}^{min}_{particle})$. In the row ethylene glycol < ethanol < water < decane $(\bar{T}^{min}_{particle})$ is increasing (**Fig. 3.2c**). This indicates that the temperature gradient created by the collapsed cavitation bubble is much larger in decane than in ethylene glycol, and, therefore, the process of solid state atomic diffusion is faster which results in bigger Al_3Ni_2 crystallites. Additionally, energy transfer between collapsed cavitation bubble and sonicated matter is estimated to be ~ 17 % more efficient in decane than in ethylene glycol and ~ 13 % than in ethanol. Overall, the bulk microstructure of metal particles can be regulated by the choice of the appropriate sonication medium at fixed time of HIUS treatment and concentration of sonicated particles.

3.3   Regulation of Metal Alloy Bulk Microstructure by Concentration of Sonicated Particles and Sonication Time

Apart from the appropriate choice of sonication medium, the metal alloy bulk microstructure can be controlled by adjustment of the concentration of sonicated particles and the duration of HIUS treatment. Our results show that for sonicated suspensions with metal particle loadings of up to 10 wt.% the crystallite growth is mainly caused by HIUS accelerated atomic diffusion   (**Fig. 3.3a**).
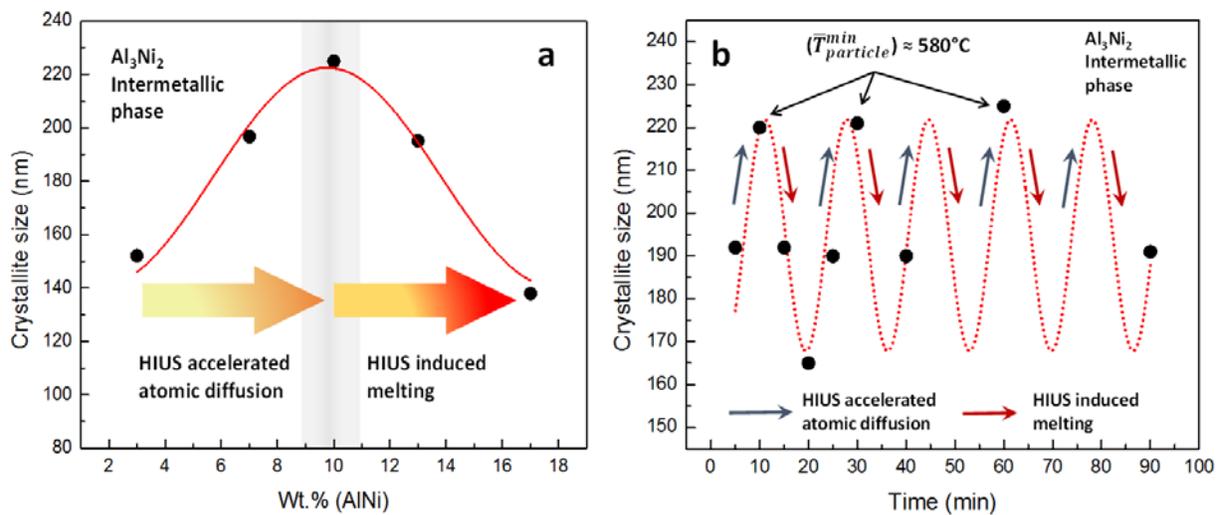
Fig. 3.3: *Plot of Al₃Ni₂ intermetallic phase crystallite size depending on the concentration of AlNi particles in decane suspensions for HIUS treatment (a); Plot of Al₃Ni₂ intermetallic phase crystallite size depending on duration of HIUS treatment of 10 wt.% AlNi particle suspension in decane (b).*

At the same time for the suspensions with metal particle loadings of more than 10 wt.%, we observed a gradual decrease of crystallite size with increasing particle concentration. Thermodynamically, the process of crystallite reduction can only occur upon re-melting of metal particles and their subsequent solidification [8]. Therefore, HIUS treatment of more concentrated suspensions due to more frequent interparticle collisions results in significant increase of ($\bar{T}_{particle}^{min}$) that should exceed the melting point of particle in the Al_3Ni_2 intermetallic phase (1683 °C). When AlNi particles were subject to variable sonication time, we also observed the phenomenon of crystallite size decrease which can serve as an additional proof of possible re-melting (**Fig. 3.3b**). Interestingly, a cyclic change of crystallite size confirms the periodic nature of cavitation bubble collapse, where energy must be repeatedly spent on the accumulation of their necessary amount, resulting in repeating of accelerated atomic diffusion/re-melting processes. Additionally, sonication-time dependent experiments confirmed that ($\bar{T}_{particle}^{min}$) might reach the value of ~ 580 °C during ultrasound treatment and repeatedly exceed it up to the value of 1638 °C or higher. Thus through the adjustment of HIUS duration and sonicated particle concentration for a given sonication medium it is possible to control the energy intake by sonicated matter for achievement of the desired bulk microstructure.

3.4   Surface Changes in Metal Alloy Caused by High Intensity Ultrasound

Upon HIUS treatment, AlNi alloy particles undergo well pronounced morphological and compositional changes. The SEM images (**Fig. 3.4a, b**) clearly show roughening and structuring of the ultrasonically treated metal surface as compared to the relatively smooth and unstructured one before treatment. Additionally, electron diffraction patterns (**Fig. 3.4a, b (insets)**) demonstrate the tendency of intermetallic crystal growth and material's enhanced crystallinity. The evidence for compositional changes was obtained by recording ^{27}Al solid state NMR spectra for AlNi alloys before and after HIUS treatment (**Fig 3.4g, h**). The results indicate that the process of phase redistribution takes place; specifically, we observed enrichment in the Al_3Ni_2 phase content on the surface, while the content of the Al_3Ni phase is slightly decreasing. This phenomenon serves as an indication of slow transformation of Al_3Ni intermetallic phase into the thermodynamically more stable Al_3Ni_2 phase [9] during ultrasonication according to the following phase transformation reaction equation ($\mathbf{Al_3Ni} \xrightarrow{\mathbf{1124K}} \mathbf{Al_3Ni_2 + L_{15,3\ at.\ \%\ Ni}}$) [10].
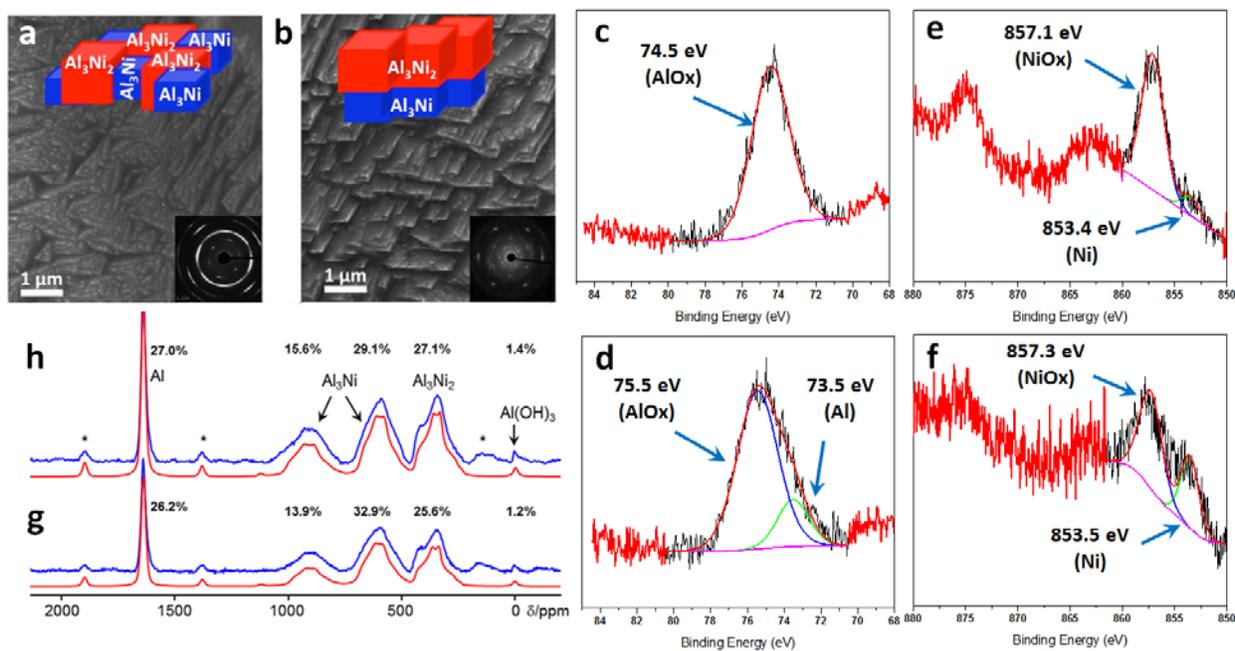
Fig. 3.4: *Scanning electron microscopy images taken from the surface of AlNi (50 wt.% Ni) before (a) and after (b) ultrasonication, as well as electron diffraction patterns (insets); the Al 2p and Ni 2p XPS spectra for the initial (c, e), HIUS treated (in ethanol) (d, f) AlNi (50 wt.% Ni) alloy particles; ^{27}Al MAS NMR spectra (blue) of initial AlNi (g) as well as sonicated (in ethanol) (h) and their corresponding simulated spectra (red), the asterisks denote spinning sidebands.*

Additional proof of surface compositional changes during HIUS treatment was obtained upon analysis of the XPS spectra (**Fig. 3.4c-f**). We observed the reduction of AlO_x to Al^0, as well as reduction of NiO_x to Ni^0, if ethanol was used as a reducing sonication medium [11]. Thus, upon using ethanol as a sonication medium we enriched the surface of the AlNi alloy with Al_3Ni_2 intermetallic phase and avoided for the electrocatalytic purposes undesirable metal (Al, Ni) oxidation.

3.5 Use of Synergetic Effects of Bulk and Surface Changes Caused by HIUS for Electrocatalytic Applications

The combination of tunable bulk and surface changes in AlNi metal alloy particles caused by HIUS treatment can be used for fabrication of robust and efficient electrocatalytic materials. Thus, we used HIUS for formation of a catalyst toward electrocatalytic hydrogen production. **Fig. 3.5a** represents a schematic illustration of the catalyst preparation procedure. An

AlNi alloy particle suspension (10 wt. %) was sonicated in ethanol for 1 h at 20 kHz frequency and intensity of 140 Wcm^{-2}. Such processing results in the following changes advantageous for electrocatalysts: (i) phase redistribution/transformation; (ii) crystal growth; (iii) crystal preferential orientation; (iv) surface structuring; (v) surface reduction. After that the modified particles are dried and deposited on the electrode for electrocatalytic activity toward hydrogen evolution evaluation.
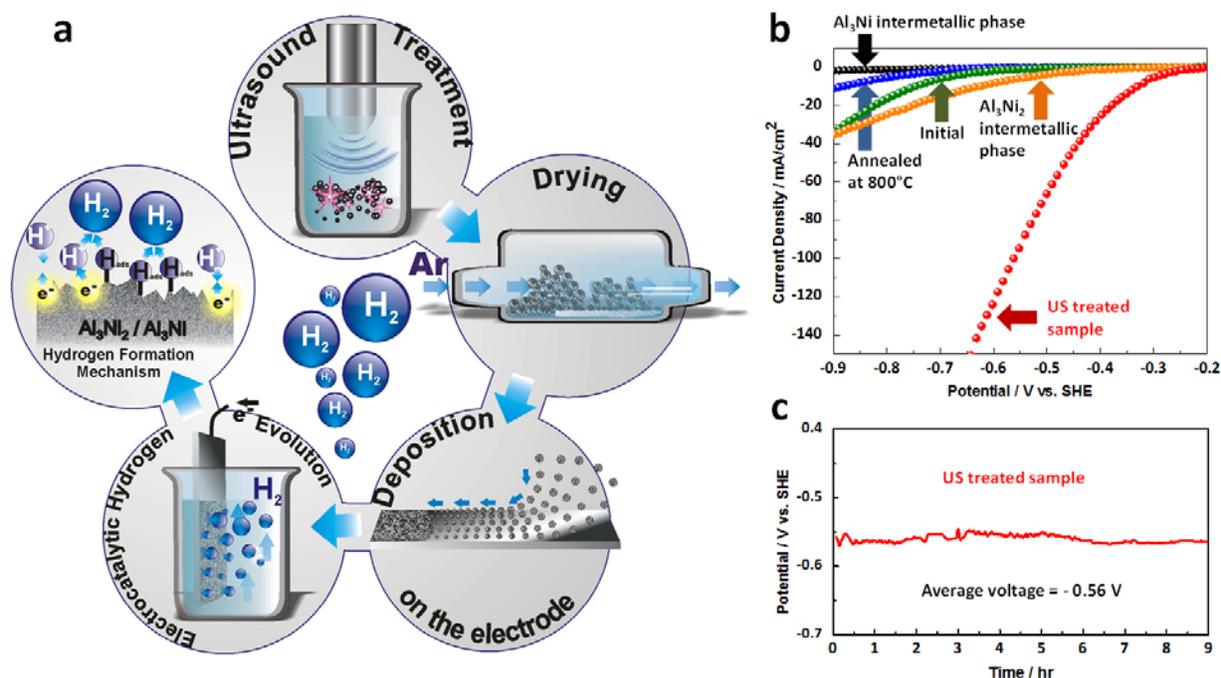
Fig. 3.5: *Schematic illustration of the catalyst preparation procedure and its electrocatalytic activity evaluation (a); HER current – potential profiles for the initial and ultrasonically modified AlNi (50 wt.% Ni) alloys, bulk commercial Al₃Ni and Al₃Ni₂ phases, as well as AlNi alloy annealed at 1173K (b). Galvanostatic HER profile for an ultrasonically modified AlNi (50 wt.% Ni) alloy (c).*

Electrochemical tests (**Fig. 3.5b**) demonstrated significantly improved behavior of HIUS treated AlNi alloy particles toward hydrogen evolution. Namely, the ultrasonically treated samples possess much lower onset overpotential, as well as greater current output as compared to untreated alloy or pure intermetallic phases. Moreover, as fabricated electrocatalyst demonstrates excellent stability which can be seen from the recorded galvanostatic profiles (**Fig. 3.5c**) – no loss in hydrogen evolution catalytic activity was observed for the time period of 9 hours. Overall, HIUS processing of metal alloys can serve as an improved alternative to existing methods of HER efficient electrocatalyst fabrication.

51

3.6 Individual Contributions to Joint Publications

The results presented in this thesis were obtained in collaboration with others. In the following, the contributions of each co-author are specified. The asterisks denote the corresponding authors.

Chapter 4

This work was published in *Ultrasonics Sonochemistry* 2015, **23**, 26-30 under the title:

"Effect of high intensity ultrasound on Al$_3$Ni$_2$, Al$_3$Ni crystallite size in binary AlNi (50 wt.% of Ni) alloy"

by Pavel V. Cherepanov*, Inga Melnyk, and Daria V. Andreeva.

I performed most of the experiments, calculations, and wrote the manuscript. Inga Melnyk assisted with sample preparation and was involved in scientific discussions. Daria V. Andreeva supervised the project, was involved in scientific discussion, data analysis and corrected the manuscript.

Chapter 5

This work was published in *Ultrasonics Sonochemistry* 2015, **26**, 9-14 under the title:

"Up to which temperature ultrasound can heat the particle?"

by Pavel V. Cherepanov*, Anna Kollath, and Daria V. Andreeva.

I performed most of the experiments, calculations, and wrote the manuscript. Anna Kollath assisted with sample preparation, calculations, and was involved in scientific discussions. Daria V. Andreeva supervised the project, was involved in scientific discussion, data analysis and corrected the manuscript.

Chapter 6

This work was published in *Green Chemistry* 2015, **17**, 2745-2749 under the title:

"The use of ultrasonic cavitation for near-surface structuring of robust and low-cost AlNi catalysts for hydrogen production"

by Pavel V. Cherepanov, Inga Melnyk, Ekaterina V. Skorb, Peter Fratzl, Emil Zolotoyabko, Natalia Dubrovinskaia, Leonid Dubrovinsky, Yamini S. Avadhut, Juergen Senker, Linn Leppert, Stephan Kuemmel, and Daria V. Andreeva*.

I performed electrochemical measurements, calculations, data analysis, and wrote the manuscript. Inga Melnyk prepared the samples. Ekaterina V. Skorb and Peter Fratzl were involved in data analysis. Emil Zolotoyabko, Natalia Dubrovinskaia, and Leonid Dubrovinsky assisted in crystallographic studies and their analysis. Yamini S. Avadhut and Juergen Senker conducted ^{27}Al solid state NMR measurements, Linn Leppert and Stephan Kuemmel performed DFT calculations. Daria V. Andreeva supervised the project, analyzed data and wrote the manuscript. All authors were involved in scientific discussions and manuscript correction.

Chapter 7

This work was published in *Ultrasonics Sonochemistry* 2015, **23**, 142-147 under the title:

"**Ultrasound assisted formation of Al-Ni electrocatalyst for hydrogen evolution"**

by Pavel V. Cherepanov, Muthupandian Ashokkumar, and Daria V. Andreeva.*

I performed most of the experiments, calculations, and wrote the manuscript. Muthupandian Ashokkumar assisted with XPS measurements, data analysis, and was involved in scientific discussion. Daria V. Andreeva supervised the project, was involved in scientific discussion, data analysis and corrected the manuscript.

References

[1] H. Conrad, J. Narayan, On the grain size softening in nanocrystalline materials, Scripta Mater., 42 (2000) 1025-1030.

[2] S.B. Jung, Y. Minamino, T. Yamane, S. Saji, Reaction-diffusion and formation of Al_3Ni and Al_3Ni_2 phases in the Al–Ni system, J. Mater. Sci. Lett. 12 (1993) 1684–1686.

[3] A.K. Zak, W.H.A. Majid, M.E. Abrishami, R. Yousefi, X-ray analysis of ZnO nanoparticles by Williamson–Hall and size-strain plot methods, Solid State Sci. 13 (2011) 251–256.

[4] A.W. Burton, K. Ong, T. Rea, I.Y. Chan, On the estimation of average crystallite size of zeolites from the Scherrer equation: a critical evaluation of its application to zeolites with one-dimensional pore systems, Microporous Mesoporous Mater. 117 (2009) 75–90.

[5] K. Venkateswarlu, A.C. Bose, N. Rameshbabu, X-ray peak broadening studies of nanocrystalline hydroxyapatite by Williamson–Hall analysis, Physica B 405 (2010) 4256–4261.

[6] S.J. Doktycz, K.S. Suslick, Interparticle collisions driven by ultrasound, Science 247 (1990) 1067–1069.

[7] J. Rae, M. Ashokkumar, O. Eulaerts, C. von Sonntag, J. Reisse, F. Grieser, Estimation of ultrasound induced cavitation bubble temperatures in aqueous solutions, Ultrason. Sonochem. 12 (2005) 325–329.

[8] A. Ilbagi, P.D. Khatibi, I.P. Swainson, G. Reinhart, H. Henein, Microstructural analysis of rapidly solidified aluminium-nickel alloys, Can. Metall. Q., 50 (2011) 295-302.

[9] D.M. Shi, B. Wen, R. Melnik, S. Yao, T.J. Lia, First-principles studies of Al-Ni intermetallic compounds, J. Solid State Chem., 182 (2009) 2664-2669.

[10] D. Batalu, G. Cosmeleata, A. Aloman, Critical Analysis of Al-Ni Phase Diagrams, Metal. Int., 8 (2006) 36-45.

[11] J.W. Phillis, A.Y. Estevez, M.H. O'Regan, Protective effects of the free radical scavengers, dimethyl sulfoxide and ethanol, in cerebral ischemia in gerbils, Neurosci. Lett. 244 (1998) 109–111.

4 Effect of high intensity ultrasound on Al$_3$Ni$_2$, Al$_3$Ni crystallite size in binary AlNi (50 wt.% of Ni) alloy

Pavel V. Cherepanov*, Inga Melnyk, and Daria V. Andreeva

Physical Chemistry II, University of Bayreuth, DE-95440 Bayreuth, Germany

*Corresponding author e-mail: pavel.cherepanov@uni-bayreuth.de

Abstract

Crystallite size of the intermetallics is one of the most important parameters that can influence kinetics of catalytic reactions. Analysis of the crystallite sizes of Al$_3$Ni and Al$_3$Ni$_2$ intermetallic phases using Scherrer and Williamson–Hall methods reveals that the sonomechanical impact of ultrasound on suspensions of AlNi particles in ethanol results in crystallites growth and microstrain reduction.

4.1 Introduction

Aluminum–nickel alloys have gained significant amount of interest among researchers after Raney has introduced activated AlNi (50 wt.% Ni) as a catalyst for hydrogenation [1] of vegetable oils. Shortly after, AlNi (50 wt.% Ni) became very popular in industrial applications, particularly as a reagent or a catalyst in organic synthesis due to its high catalytic activity [2, 3]. However, active Raney Ni is difficult to handle. It is pyrophoric and should be stored under distilled water in a special place. Recently, we proposed that AlNi alloys could be activated by treatment of aqueous suspensions of AlNi particles [4]. Ultrasonic modification of the metal particles in aqueous media leads to a partial oxidation of metal and formation of porous morphology of the catalyst. Furthermore, we observed that after sonication AlNi particles still have metallic skeleton [5]. Increased accessibility of active metal centers for substrate molecules was achieved by distribution of Al$_3$Ni and Al$_3$Ni$_2$ intermetallics [6] in the porous metal oxide matrix. Due to porous morphology, high surface area and high accessibility of active centers

and metal/metal oxide composition ultrasonically activated AlNi catalyst has high catalytic activity and high stability in contrast to Raney nickel. However, the mechanism of the activation of alloys via ultrasonication has a number of open questions. One of them is how the crystal structure of metals is affected by ultrasonication.

Crystallographic parameters such as crystal system, orientation of crystallites and their size, as well as microstrain [7–9] are among the most important parameters that can influence kinetics and efficiency of catalytic reactions. Therefore, catalytic activity of ultrasonically activated AlNi alloy is to a high extent defined by presence of intermetallic compounds such as hexagonal (P-3m1) Al_3Ni_2 and orthorhombic (Pnma) Al_3Ni. We suggest that additionally to surface chemistry and morphology of AlNi particles high intensity ultrasound (HIUS) can also affect crystal structure of the intermetallics. Suslick et al. showed that due to effects of shock waves generated in ultrasonic field and intense interparticle collisions interfacial regions of metal particles can melt [10]. Thus, HIUS can provide enough energy to metals and stimulate rapid diffusion of metal atoms and cause changes of crystallite sizes as well as microstrain.

Here we report on investigation of HIUS effect on size and strain of the Al_3Ni_2 and Al_3Ni intermetallic compounds in AlNi (50 wt.% of Ni) alloy. The structural determination of Al_3Ni_2 and Al_3Ni phases after ultrasonic treatment was performed by Rietveld refinement. Crystallite size with respect to the specific reflection planes was evaluated using Scherrer approach [11, 12], while mean crystallite size and strain calculations were estimated by modified form of Williamson–Hall (WH) method [13–15] such as uniform deformation model (UDM).

4.2 Experimental section

Aluminum – Nickel (50 wt.% Ni) alloy powder with average particle size of 140 μm was purchased from Fluka as well as anhydrous ethanol. All chemicals were the highest purity grade available and were used as received without further purification.

Al/Ni alloy powder (4 g) was dispersed in (40 mL) of ethanol or ethylene glycol and sonicated for 60 min with a Hielscher UIP1000hd, (Ultrasonics GmbH, Germany) operated at 20 kHz with a maximum output power of 1000 W. The apparatus was equipped with an ultrasonic horn BS2d22 (head area of 3.8 cm^2) and a booster B2-1.8. The maximum intensity was calculated to be 140 W cm^{-2} at mechanical amplitude of 106 μm. To avoid overheating during sonication the experiment was carried in a homemade thermostatic cell connected to a thermostat (Huber GmbH, Germany). The temperature was monitored during the treatment and

kept at 298 K After HIUS treatment metal particles were separated from supernatant by centrifugation at a speed of 10 000 rpm for 1 hr and washed with absolute ethanol followed by drying under vacuum at room temperature.

Powder X – ray diffraction (PXRD) analysis of the samples was performed using Stoe STADI P X – ray transmission diffractometer (CuKα radiation from the copper target using an in built nickel filter, λ = 1.54056 Å).

Crystallographic parameters such as crystallite size and microstrain were calculated using Scherrer and Williamson-Hall methods.

Scherrer method relies on utilizing the following equation:

$$D = \frac{k\,\lambda}{\beta_D \cos\theta} \qquad (1)$$

where k is shape factor (a constant equals to 0.94), λ is the X-ray wavelength (1.54056 Å for CuK$_\alpha$ radiation), β_D is the instrumental corrected peak width at half-maximum intensity, θ is the peak position, and D is the effective crystallite size normalized to the reflecting planes. It is important to note that to avoid any misleading; only not overlapping peaks were chosen for data processing.

According to WH method strain-induced broadening arising from crystal imperfections and distortion are related by:

$$\varepsilon \approx \frac{\beta_s}{\tan\theta} \qquad (2)$$

Assuming that the size and strain contributions to the line broadening are independent of each other, the observed line breadth can be written as the sum of the two terms:

$$\beta_{hkl} = \beta_s + \beta_D \qquad (3)$$

Substitution of Eq. (1) and Eq. (2) into Eq. (3) results in the following:

$$\beta_{hkl} = \left(\frac{k\lambda}{D\cos\theta}\right) + (4\varepsilon\tan\theta) \qquad (4)$$

After rearranging, Eq.(4) becomes:

$$\beta_{hkl}\cos\theta = \left(\frac{k\lambda}{D}\right) + (4\varepsilon\sin\theta) \qquad (5)$$

The WH equation represents uniform deformation model (UDM) where the strain is assumed to be uniform in all crystallographic directions, thus considering the isotropic nature of the crystals, where all the material properties are independent of the direction along which they are measured. Plotting values of $\beta_{hkl}cos\theta$ as a function of $4\varepsilon sin\theta$ allows estimating microstrain ε (slope of the fitted line) and the average crystallite size D (y-intercept of the fitted line).

Transmission electron microscopy (TEM) was performed on LEO 922 EFTEM operating at 200 kV.

4.3 Results and discussion

In order to maximize the influence of HIUS on crystallites' sizes and exclude other possible effects of sonication e.g. particle fragmentation, change of surface roughness, formation of metal oxides / hydroxides 140 μm initial AlNi (50 wt.% Ni) particles were sonicated in presence of ethanol. Especially, presence of metal oxides / hydroxides in the material can significantly complicate interpretation and evaluation of PXRD patterns. Indeed, the size and the morphology of the particles did not change after sonication in ethanol. Ethanol serves as a scavenger of OH radicals [16]. Its use as a sonication media can prevent partial oxidation of metals and, therefore, allow accurate monitoring of crystallite sizes' changes upon sonication. We used fixed sonication time of 60 min. Our previous works demonstrated that 60-min sonicated samples exhibited the best catalytic properties [4].

Effect of HIUS on the size of the crystallites can be seen in transmission electron spectroscopy (TEM) images in **Fig. 4.1**. The size of the crystallites in the ultrasonically treated samples has significantly increased. The crystallites are highlighted by the arrows in the images. Additional evaluation of the crystallites' sizes was done by applying of Scherrer and Williamson-Hall approaches to powder X-ray diffraction (PXRD) patterns.
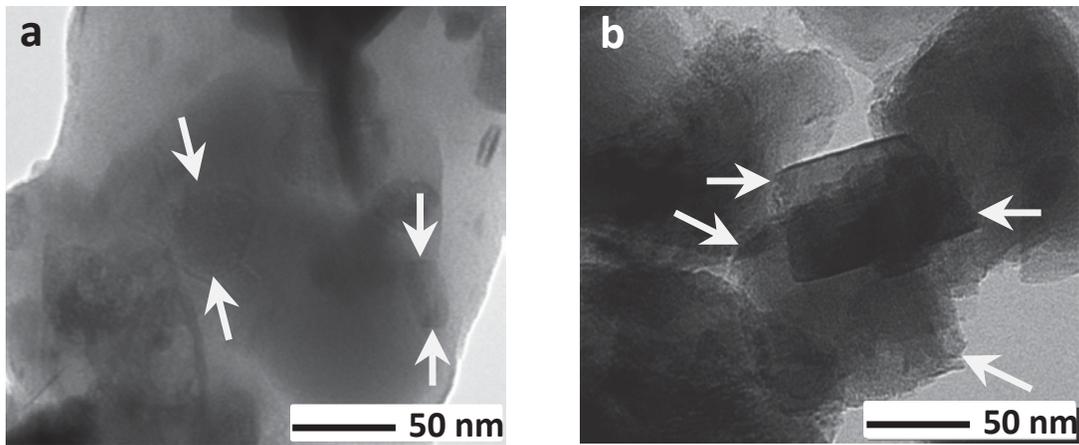
Fig. 4.1: *TEM images of initial (a) and HIUS treated in ethanol (b) AlNi (50 wt.% Ni) alloy.*

The PXRD patterns of initial and HIUS treated in presence of ethanol AlNi (50 wt.% Ni) alloys are shown in **Fig. 4.2**. All detectable peaks could be indexed as either Al_3Ni_2 or Al_3Ni intermetallic phases found in the standard reference data (JCPDS: 00-014-0648) and (JCPDS: 00-002-0416).
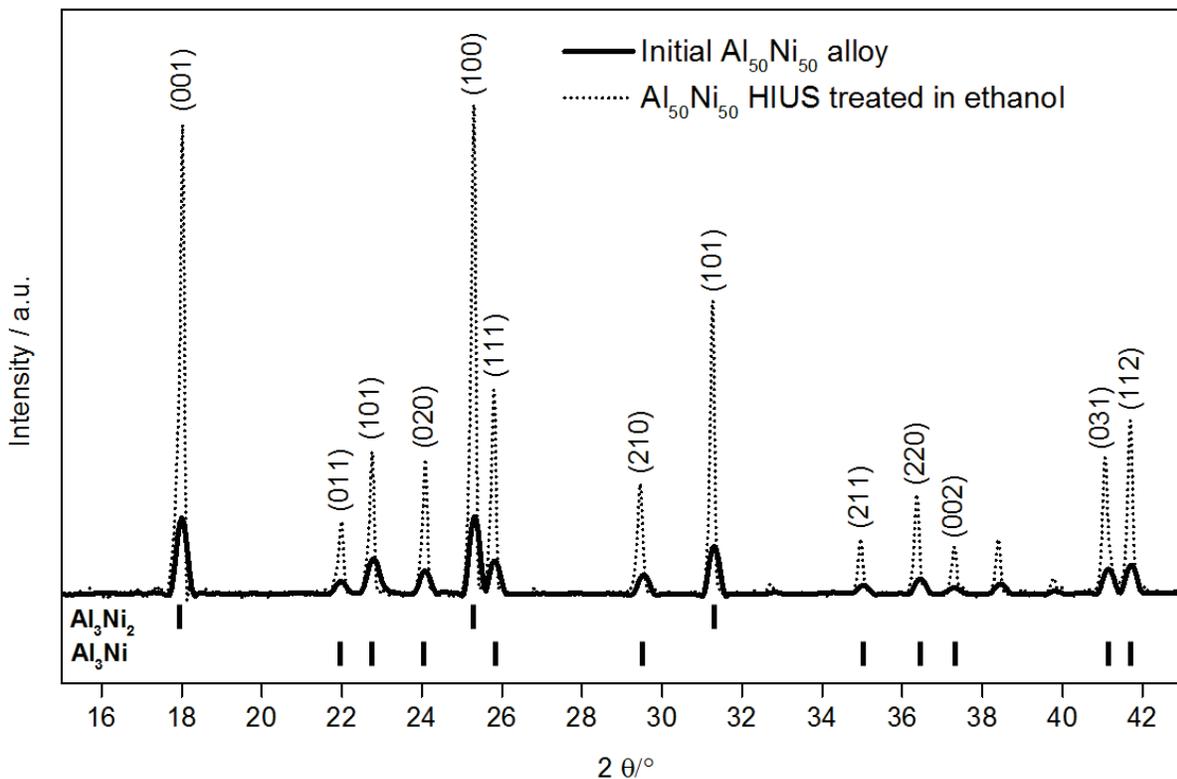
Fig.4.2: *The XRD patterns of initial and HIUS treated in organic solvents AlNi (50 wt.% Ni) alloys.*

The patterns in **Fig. 4.2** indicate that the materials before and after modification have absolutely identical XRD patterns. However, it is clearly seen that the reflection peaks became sharper after ultrasound treatment of AlNi alloy, indicating the crystallite size's change. The crystallite sizes of both Al_3Ni_2 and Al_3Ni intermetallic phases were determined by X-ray line broadening.

Scherrer analysis was used to evaluate crystallite size of Al_3Ni_2 and Al_3Ni intermetallics with respect to corresponding reflecting planes. The crystallographic parameters obtained from the Scherrer method are summarized in **Table 4.1** and **4.2**. The values indicate that HIUS treatment of AlNi alloy results in gradual Al_3Ni_2 and Al_3Ni crystallite sizes' increase in all crystallographic directions including edge - (100), (020) and basal - (001), (002) planes. Thus, the average crystallite growth for Al_3Ni_2, as well as Al_3Ni intermetallics was calculated to be ~ 40 % with respect to specific crystallographic plane. Although, Scherrer method does not provide any information in the case when in addition to size broadening strain-induced broadening occurs. For this reason we applied Williamson-Hall (WH) method for XRD reflection peak analysis.

Table 4.1: *Structure and geometric parameters of Al₃Ni₂ intermetallic phase in initial and HIUS treated in ethanol AlNi (50 wt.% Ni) alloy.*

Intermetallic Phase	2θ	(*hkl*)	Scherrer method D (nm)		Williamson - Hall method (UDM) D (nm)	
			Initial	Ethanol	Initial	Ethanol
Al_3Ni_2	18.0	(001)	79.6	125.8	87.8	131.7
(trigonal)	25.3	(100)	95.5	126.4		
P-3m1	31.3	(101)	102.4	141.0	ε (-0.56892×10⁻⁴)	ε (0.15315×10⁻⁴)
$V_{cell}(0.0721nm^3)$	62.7	(103)	114.0	142.5		

Table 4.2: *Structure and geometric parameters of Al₃Ni intermetallic phase in initial and HIUS treated in ethanol AlNi (50 wt.% Ni) alloy.*

Intermetallic Phase	2θ	(*hkl*)	Scherrer method D (nm)		Williamson - Hall method (UDM) D (nm)	
			Initial	Ethanol	Initial	Ethanol
Al_3Ni	22.0	(011)	80.8	117.1	56.3	113.2
(orthorh.)	22.8	(101)	60.7	123.2		
Pnma	24.1	(020)	84.8	123.1	ε (-8.19925×10⁻⁴)	ε (-0.87570×10⁻⁴)
V_{cell}	29.5	(210)	95.1	110.8		
$(0.2329nm^3)$	37.3	(002)	81.8	124.2		

The WH analysis of Al_3Ni_2 XRD reflection peaks is shown in **Fig. 4.3(a-c)**. Great scatter of the points on **Fig. 4.3a** for the untreated sample is a direct indication of uneven microstrain distribution in grain boundaries throughout the sample. Nevertheless, the scattering of the points away from the linear fit is becoming less after HIUS treatment. Interestingly, along with scattering decrease for ultrasonically treated phases microstrain ε value (**Table 4.1**) is found to be closer to zero as oppose to untreated phases. These results indicate overall microstructuring and strain relaxation in grain boundaries. Further, the average crystallite size for all phases was estimated from the y-intercept **Fig. 4.3(c)**. The values are in a good agreement with those obtained for the Al_3Ni_2 reflection planes using Scherrer method with the same tendency observed: crystallite size is increasing after ultrasound treatment. Similar analysis was carried out for Al_3Ni intermetallic compound present in AlNi alloy and is shown in **Fig. 4.4(a-c)**. As in case of Al_3Ni_2 intermetallic phase, the obtained data are in a good agreement with ones obtained using Scherrer method. The scattering became less after HIUS treatment along with closer to zero microstrain ε values (**Table 4.2**). Thus, both Al_3Ni_2 and Al_3Ni intermetallic phases underwent strain relaxation and crystallites became approximately twice larger in size.
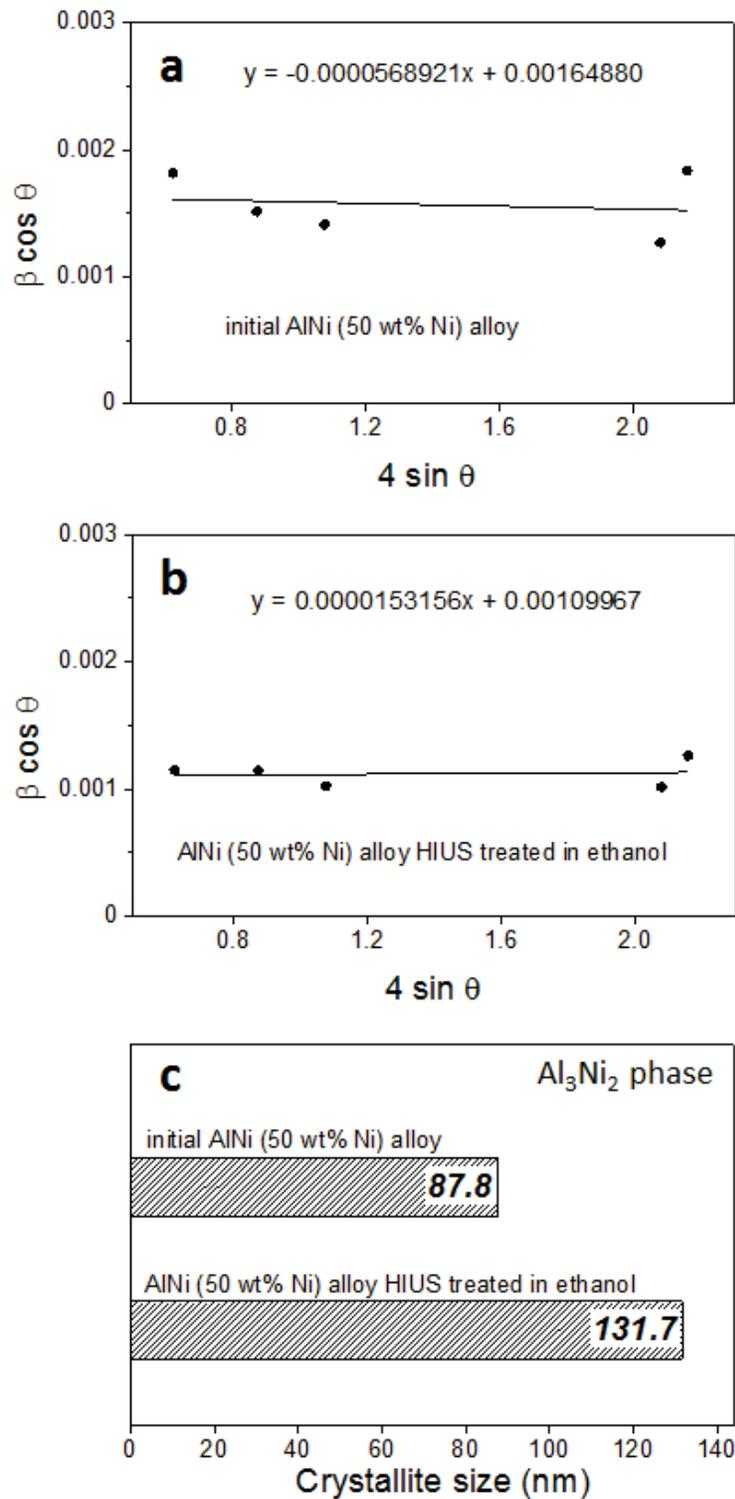
Fig. 4.3: *The Williamson – Hall analysis of Al_3Ni_2 intermetallic phase present in initial and HIUS treated in ethanol AlNi (50 wt.% Ni) alloys assuming UDM. Fit to the data, the strain (ε) is extracted from the slope and the crystallite size D is extracted from the y – intercept of the fit (a, b). Bar plot of Al_3Ni_2 intermetallic crystallite size (c).*
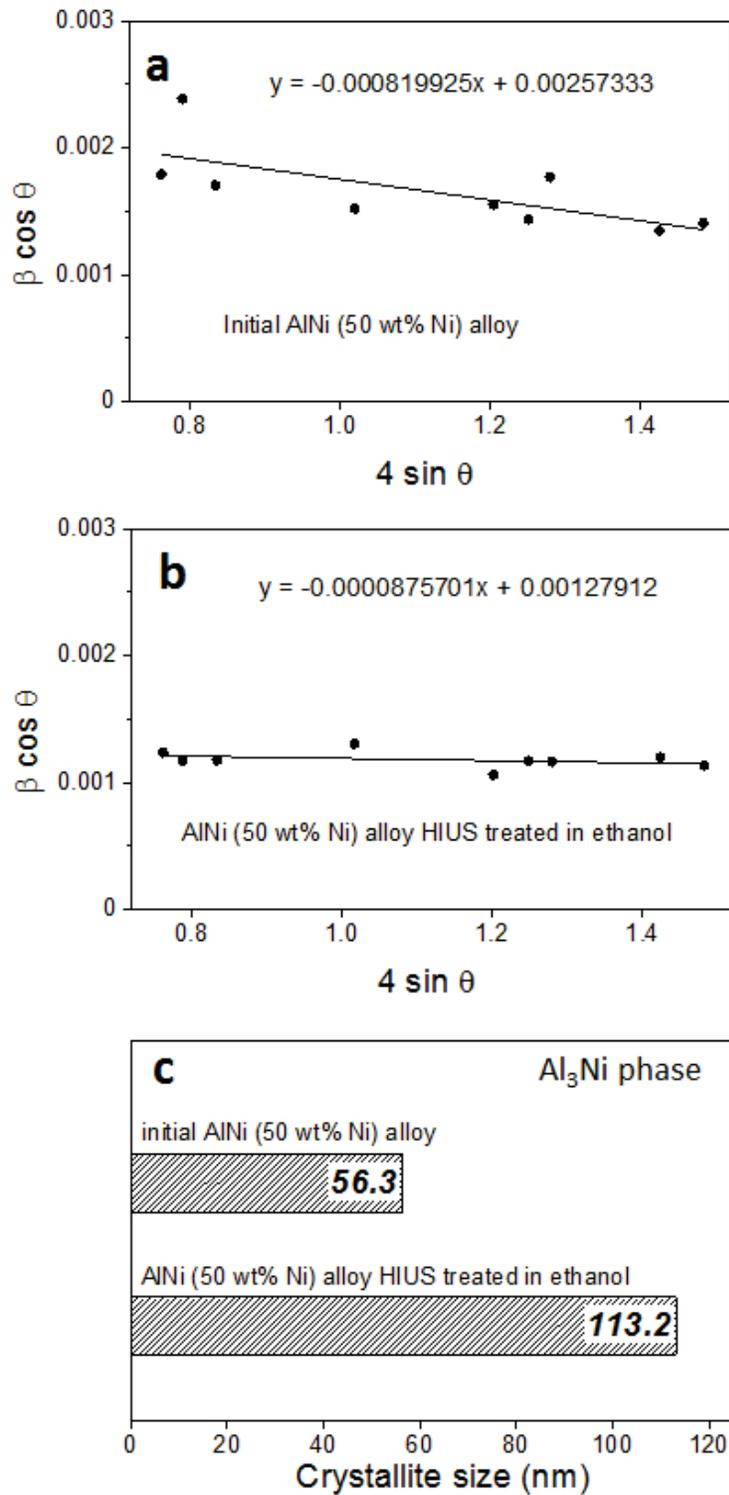
Fig. 4.4: *The Williamson – Hall analysis of **Al₃Ni** intermetallic phase present in initial and HIUS treated in ethanol AlNi (50 wt.% Ni) alloys assuming UDM. Fit to the data, the strain (ε) is extracted from the slope and the crystallite size D is extracted from the y – intercept of the fit (a, b). Bar plot of **Al₃Ni** intermetallic crystallite size (c).*

Detailed evaluation of XRD patterns using Scherrer and WH method showed that acoustic cavitation and associated with it sonomechanical effects (shock waves, interparticles' collisions) lead to growth of the presented crystallites. According to hot spot theory cavitation bubbles are filled with plasma with temperature up to thousands of Kelvins and pressure up to hundreds of atmospheres [17-20]. It has been reported that temperature in solid / liquid interface in cavitated suspensions of metal particle can reach the values of up to 2400 K [7]. This temperature values are much higher than the liquidus temperature of AlNi (50 wt.% of Ni) alloy that is 1673 K. HIUS can serve as a thermodynamic driving force for a grain boundary reduction. Using our data on the crystallite size change we could estimate that grain boundary area is changed for the experimental time (60 min) in AlNi system to approx. 2×10^{-18} m^2/s. This value doesn't exceed the reported diffusivity values for the same material estimated at 1373 K [21, 22]. Thus, via sonication it is possible to significantly accelerate atomic diffusion in metals and alloys while macroscopically the reaction temperature remains 298 K. Since relatively strong attraction was measured for Al-Ni atoms in comparison to attractions between Al-Al and Ni-Ni atoms diffusion leads to clustering of the intermetallic phases. Thus, ultrasonically treated AlNi tends to form larger clusters of Al$_3$Ni and Al$_3$Ni$_2$ phases due to grain boundary area reduction.

4.4   Conclusions

Here we reported on the effect of high intensity ultrasound on crystal structure of AlNi alloy (50 wt.% of Ni). Upon analysis of the crystallite sizes of Al$_3$Ni and Al$_3$Ni$_2$ intermetallic phases using Scherrer and Williamson–Hall methods we observed that ultrasonic treatment of metal particles suspensions led to an increase in crystallites' sizes and reduction of microstrain in the system. After 60 min of HIUS modification the size of the crystallites increased by a factor of 2. Thus, intensive sonication of solid particles can enhance the process of atomic diffusion. In AlNi particles atomic diffusion led to the clustering and phase separation of intermetallics. In the future, it will be interesting to investigate the diffusion processes depending on the duration and intensity of sonication as well as sonication medium.

Acknowledgments

References

[1] M. Raney, USA Patent, in, 1925.

[2] P. Gallezot, P.J. Cerino, B. Blanc, G. Fleche, P. Fuertes, Glucose hydrogenation on promoted Raney - Nickel catalysts, J. Catal., 146 (1994) 93-102.

[3] B.W. Hoffer, E. Crezee, F. Devred, P.R.M. Mooijman, W.G. Sloof, P. Kooyman, A.D. van Langeveld, F. Kapteijn, J.A. Moulijn, The role of the active phase of Raney-type Ni catalysts in the selective hydrogenation of D-glucose to D-sorbitol, Appl. Catal. A-Gen., 253 (2003) 437-452.

[4] J. Dulle, S. Nemeth, E.V. Skorb, T. Irrgang, J. Senker, R. Kempe, A. Fery, D.V. Andreeva, Sonochemical Activation of Al/Ni Hydrogenation Catalyst, Adv. Funct. Mater., 22 (2012) 3128-3135.

[5] E.V. Skorb, H. Mohwald, T. Irrgang, A. Fery, D.V. Andreeva, Ultrasound-assisted design of metal nanocomposites, Chem. Commun., 46 (2010) 7897-7899.

[6] S.B. Jung, Y. Minamino, T. Yamane, S. Saji, Reaction-diffusion and formation of AL3NI AND AL3NI2 phases in the Al-Ni system J. Mater. Sci. Lett., 12 (1993) 1684-1686.

[7] B. Hinnemann, P.G. Moses, J. Bonde, K.P. Jorgensen, J.H. Nielsen, S. Horch, I. Chorkendorff, J.K. Norskov, Biornimetic hydrogen evolution: MoS2 nanoparticles as catalyst for hydrogen evolution, J. Am. Chem. Soc., 127 (2005) 5308-5309.

[8] T.F. Jaramillo, K.P. Jorgensen, J. Bonde, J.H. Nielsen, S. Horch, I. Chorkendorff, Identification of active edge sites for electrochemical H-2 evolution from MoS2 nanocatalysts, Science, 317 (2007) 100-102.

[9] D. Voiry, H. Yamaguchi, J.W. Li, R. Silva, D.C.B. Alves, T. Fujita, M.W. Chen, T. Asefa, V.B. Shenoy, G. Eda, M. Chhowalla, Enhanced catalytic activity in strained chemically exfoliated WS2 nanosheets for hydrogen evolution, Nat. Mater., 12 (2013) 850-855.

[10] S.J. Doktycz, K.S. Suslick, Interparticle Collisions Driven By Ultrasound, Science, 247 (1990) 1067-1069.

[11] A.W. Burton, K. Ong, T. Rea, I.Y. Chan, On the estimation of average crystallite size of zeolites from the Scherrer equation: A critical evaluation of its application to zeolites with one-dimensional pore systems, Microporous Mesoporous Mat., 117 (2009) 75-90.

[12] J.I. Langford, A.J.C. Wilson, Scherrer after 60 years - survey and some new results in determination of crystallite size, J. Appl. Crystallogr., 11 (1978) 102-113.

[13] T. Ungar, A. Revesz, A. Borbely, Dislocations and grain size in electrodeposited nanocrystalline Ni determined by the modified Williamson-Hall and Warren-Averbach procedures, J. Appl. Crystallogr., 31 (1998) 554-558.

[14] K. Venkateswarlu, A.C. Bose, N. Rameshbabu, X-ray peak broadening studies of nanocrystalline hydroxyapatite by Williamson-Hall analysis, Physica B, 405 (2010) 4256-4261.

[15] A.K. Zak, W.H.A. Majid, M.E. Abrishami, R. Yousefi, X-ray analysis of ZnO nanoparticles by Williamson-Hall and size-strain plot methods, Solid State Sci., 13 (2011) 251-256.

[16] J.W. Phillis, A.Y. Estevez, M.H. O'Regan, Protective effects of the free radical scavengers, dimethyl sulfoxide and ethanol, in cerebral ischemia in gerbils, Neurosci. Lett., 244 (1998) 109-111.

[17] E.A. Neppiras, B.E. Noltingk, Cavitation produced by ultrasonics - theoretical conditions for the onset of cavitation, Proceedings of the Physical Society of London Section B, 64 (1951) 1032-1038.

[18] B.E. Noltingk, E.A. Neppiras, Cavitation produced by ultrasonics, Proceedings of the Physical Society of London Section B, 63 (1950) 674-685.

[19] E. Ciawi, J. Rae, M. Ashokkumar, F. Grieser, Determination of temperatures within acoustically generated bubbles in aqueous solutions at different ultrasound frequencies, J. Phys. Chem. B, 110 (2006) 13656-13660.

[20] J. Rae, M. Ashokkumar, O. Eulaerts, C. von Sonntag, J. Reisse, F. Grieser, Estimation of ultrasound induced cavitation bubble temperatures in aqueous solutions, Ultrasonics Sonochemistry, 12 (2005) 325-329.

[21] Y. Minamino, Y. Koizumi, N. Tsuji, T. Yamada, T. Takahashi, Interdiffusion in Co solid solutions of Co-Al-Cr-Ni system at 1423 K, Mater. Trans., 44 (2003) 63-71.

[22] S. Shankar, L.L. Seigle, Interdiffusion and intrinsic diffusion in NiAl (delta) phase of Al-Ni system, Metallurgical Transactions a-Physical Metallurgy and Materials Science, 9 (1978) 1467-1476.

5 Up to which temperature can ultrasound heat the particle?

Pavel V. Cherepanov*, Anna Kollath, and Daria V. Andreeva

Physical Chemistry II, University of Bayreuth, DE-95440 Bayreuth, Germany

*Corresponding author e-mail: pavel.cherepanov@uni-bayreuth.de

Abstract

Crystallographic property such as crystallite size has been used for evaluation of the temperature up to which high intensity ultrasound can heat metal particles depending on physical properties of sonication medium and particle concentration. We used > 100 μm metal particles as an in situ indicator for ultrasonically induced temperature in the particle interior. Based on powder X-ray diffraction monitoring of Al_3Ni_2 crystallite sizes after ultrasound treatment the average minimum temperature ($\bar{T}_{particle}^{min}$) of sonicated particles in various sonication media was estimated. Additionally, it was found that crystallite size in ultrasonically treated metal particle depends on the frequency of interparticle collision. Through the adjustment of particle concentration, it is possible to either accelerate the atomic diffusion or force the melting and recrystallization processes. Overall, the energy released from collapsing cavitation bubble can be controllably transferred to the sonication matter through the appropriate choice of sonication medium and the adjustment of particle concentration.

5.1 Introduction

The cavitation phenomenon has been intensively studied for several decades unraveling the details on the mechanism of cavitation bubble formation, oscillating growth, and consequent collapse [1, 2]. Great number of research work has been dedicated to investigation of cavitation bubble physical properties such as internal temperature and pressure [3]. Experimentally measured values of temperature inside cavitation bubble were reported in the range of ~5000 K depending on vapor pressure of the liquid that is being ultrasonicated [4, 5].

The acoustically generated "hot spots" – localized areas of extremely high temperatures and pressures [6] can release significant amount of energy to initiate various bottom-up synthesis of colloids at highly non-equilibrium conditions [7, 8]. For example amorphous iron, carbon and nanoalloys were sonochemically prepared from organometallic compounds that were decomposed inside the collapsing bubble [9-11].

Besides sonochemical processes that use collapsing bubble as a microreactor [12] for high-temperature synthesis, sonomechanical processes can also trigger highly non-equilibrium nanostructuring [13-17]. In suspensions of particles bubble collapse induces shock waves, intensive turbulent flow, and interparticle collisions. It was shown that in concentrated (20 wt.%) suspensions of ~10 μm particles the surfaces of sonicated particles can locally melt in the temperature range of 2600-3400 °C and form fused agglomerates of particles [18]. However, which temperature is inside ultrasonically treated particles is still unknown. Weather acoustic cavitation can affect microstructure of both the surface and the interior of μm-sized particles and can be used for top-down synthesis of nanomaterials is an interesting question.

Energy release/transfer from collapsing cavitation bubble depends on sonication medium [1, 2]. Varying sonication medium it is possible to adjust ultrasonic conditions for a particular synthesis. For instance, the thermal impact of continuously imploding cavitation bubbles on the surrounding liquid or sonicated matter itself depends on the physical properties of sonication medium such as vapor pressure or viscosity [19]. The main obstacle in precise evaluation of energy transfer from collapsed bubble is the absence of reliable characterization methods or a material which would serve as an indicator for such transition.

Recently, we showed that high intensity ultrasound (HIUS) treatment of AlNi (50 wt.% Ni) alloy particles suspension in ethanol led to noticeable changes in crystallographic properties [20]. Specifically, we observed present in AlNi alloy Al_3Ni_2 intermetallic crystallite growth and microstrain reduction due to thermally accelerated atomic diffusion. As oppose to metallurgical industry where temperature forced grain growth is leading to undesirable metal materials softening [21], in catalysis, for example, growth of crystallites may be quiet beneficial [22].

Since it is undoubtedly clear that grain boundary reduction is forced thermally, induced by temperature gradient crystallite growth to a particular value requires a defined amount of energy, thus, the crystallite size may serve as an indicator of the energy transfer efficiency from collapsing cavitation bubble with respect to sonication medium. In other words, we suggest that through powder X-ray diffraction (PXRD) based monitoring of the crystallite size in metal

particles it is possible to estimate the average minimum temperature ($\bar{T}_{particle}^{min}$) to which metal particles can be heated in the cavitated medium. These findings might be of a great interest in the areas of sonochemical synthesis, ultrasonic food processing, or ultrasonically induced nanostructuring for various applications.

In present study we report on the temperature effect of acoustic cavitation during HIUS treatment of Al_3Ni_2 phase in AlNi (50 wt.% Ni) alloy particles depending on physical properties of sonication medium. Based on PXRD monitoring of Al_3Ni_2 intermetallic crystallite sizes after ultrasound treatment we made an attempt to estimate the average minimum temperature ($\bar{T}_{particle}^{min}$) of sonicated AlNi alloy particles in various sonication media. Al_3Ni_2 intermetallic phase identification was performed by Rietveld refinement of PXRD patterns. Crystallographic parameter such as crystallite size was evaluated using uniform deformation model (UDM) based Williamson – Hall (WH) method [23-25]. Keeping in mind that pressure can influence the crystal structure of solids; we plan to address the aspects of ultrasonically induced pressure effects on metal particle in our ongoing studies.

5.2   Experimental section

Aluminum – Nickel (50 wt.% Ni) alloy powder with average particle size of 140 μm was purchased from Fluka. Anhydrous ethanol, ethylene glycol, and decane were purchased from Sigma Aldrich. All chemicals were the highest purity grade available and were used as received without further purification. The water was purified before use in a three stage Milipore Milli-Q Plus 185 purification system.

0.1 g ml^{-1} Al/Ni alloy powder was sonicated in ethanol, ethylene glycol, decane, or ethanol/water and ethylene glycol/water mixtures for 60 min with a Hielscher UIP1000hd, (Hielscher Ultrasonics GmbH, Germany) operated at 20 kHz with a maximum output power of 1000 W. The apparatus was equipped with an ultrasonic horn BS2d22 (head area of 3.8 cm^2) and a booster B2-1.8. The maximum intensity was calculated to be 140 W cm^{-2} at mechanical amplitude of 106 μm. To avoid overheating during sonication the experiment was carried in a homemade thermostatic cell connected to a thermostat (Huber GmbH, Germany). The temperature was monitored during the treatment and kept at 333 K After HIUS treatment metal particles were separated from supernatant by centrifugation at a speed of 10 000 rpm for 1 hour and washed with absolute ethanol followed by drying under vacuum at room temperature. To investigate the effect of particle concentration, various amounts (0.025-0.125 g ml^{-1}) of AlNi

particles were sonicated in decane for 60 min. For evaluation of ultrasonic irradiation time effect, 4 g of AlNi particle suspensions in decane were ultrasonically treated during 5, 10, 15, 20, 25, 30, 40, 60, and 90 minutes. As a reference experiment, to ensure the effect of acoustic cavitation on crystallographic properties, AlNi particle suspension was subject to 60 min of intensive stirring (13 000 rpm). No change in crystallographic parameters was observed.

For the annealing procedure 4 g of AlNi (50 wt.% Ni) alloy powder was placed in the preheated to required temperature muffle oven (Heraeus, Germany)for two hours and kept there for 60 min. The procedure was carried for six AlNi alloy powder samples at the following temperatures: 500, 550, 600, 650, 700 and 1000 °C.

Powder X – ray diffraction (PXRD) analysis of the samples was performed using Stoe STADI P X – ray transmission diffractometer (CuKα radiation from the copper target using an in built nickel filter, λ = 1.54056 Å).

Crystallographic parameter such as crystallite size was calculated using Scherrer and Williamson-Hall methods [20]. Present in AlNi alloy particles Al_3Ni phase was not used for the calculations since it can be easily oxidized in aqueous sonication medium [22].

Scherrer method relies on utilizing the following equation:

$$D = \frac{k\,\lambda}{\beta_D \cos\theta} \qquad (1)$$

where k is shape factor (a constant equals to 0.94), λ is the X-ray wavelength (1.54056 Å for CuK_α radiation), β_D is the instrumental corrected peak width at half-maximum intensity, θ is the peak position, and D is the effective crystallite size normalized to the reflecting planes. It is important to note that to avoid any misleading; only not overlapping peaks were chosen for data processing.

According to WH method strain-induced broadening arising from crystal imperfections and distortion are related by:

$$\varepsilon \approx \frac{\beta_s}{\tan\theta} \qquad (2)$$

Assuming that the size and strain contributions to the line broadening are independent of each other, the observed line breadth can be written as the sum of the two terms:

$$\beta_{hkl} = \beta_s + \beta_D \qquad (3)$$

Substitution of Eq. (1) and Eq. (2) into Eq. (3) results in the following:

$$\beta_{hkl} = \left(\frac{k\lambda}{D\cos\theta}\right) + (4\varepsilon \tan\theta) \qquad (4)$$

After rearranging, Eq.(4) becomes:

$$\beta_{hkl}cos\theta = \left(\frac{k\lambda}{D}\right) + (4\varepsilon sin\theta) \qquad (5)$$

The WH equation represents uniform deformation model (UDM) where the strain is assumed to be uniform in all crystallographic directions, thus considering the isotropic nature of the crystals, where all the material properties are independent of the direction along which they are measured. Plotting values of $\beta_{hkl}cos\theta$ as a function of $4\varepsilon sin\theta$ allows estimating microstrain ε (slope of the fitted line) and the average crystallite size D (y-intercept of the fitted line).

5.3   Results and discussion

Fig. 5.1 schematically represents Al_3Ni_2 crystallites growth in AlNi (diameter is approx. 140 μm, 50 wt.% Ni) alloy particles that is induced by temperature gradient. In 10 wt.% suspensions of metal particles cavitation induced shock waves and interparticle collisions can create the temperature gradient [26] that propagates in a particle and forces crystal growth. Since it is known that intensity of cavitation depends on sonication medium, different crystallite size can be expected in different sonication media. Thus, change in crystallographic properties might serve as an indicator of energy transfer between collapsing cavitation bubbles and sonicated matter. To provide the information on the heat transfer from collapsing cavitation bubbles to the sonicated matter we used sonication media with various physical properties – vapor pressure and viscosity. Namely, we treated AlNi alloy particles with HIUS in water / ethanol and water / ethylene glycol mixtures and in decane.

In order to calibrate thermal effect of acoustic cavitation on crystallographic property such as crystallite size we annealed the metal particles for 1 hour at various temperatures: 500, 550, 600, 650, 700, and 1000 °C. The chosen annealing duration is equivalent to the HIUS treatment time. Using annealing procedure we simulate thermal effect of HIUS. **Fig. 5.2a** shows dependence of Al_3Ni_2 intermetallic crystallite size on the annealing temperature. We calculated the crystallite sizes of the samples by applying Williamson-Hall approach for the PXRD data analysis. It can be seen, that in the temperature ranges between 500 °C and 700 °C the size of crystallites in Al_3Ni_2 phase increases with temperature increase and reaches its maximum value of 250 nm at approx. 700 °C. Annealing of the samples at the temperature above 1000 °C does not lead to the formation of the crystallites larger than 250 nm. We use the obtained crystallite size vs. temperature dependence as a calibration curve for the estimation of the possible temperature up to which HIUS can heat metal particles. Using crystallite size data for the annealed samples as

the reference allowed us to estimate minimum average temperature of metal particles ($\bar{T}_{particle}^{min}$) after 1 hour of US treatment depending on sonication medium.
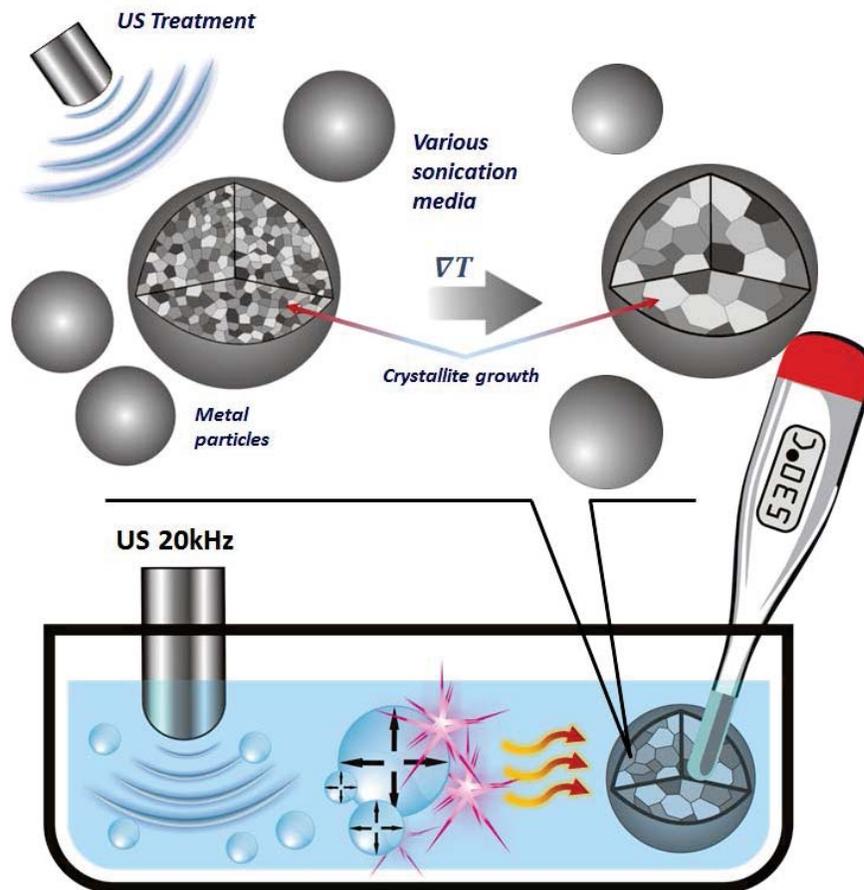
Figure 5.1: *Schematic representation of Al$_3$Ni$_2$ crystallites change in AlNi particles upon HIUS treatment and energy transfer between collapsing cavitation bubbles and sonicated matter.*

Upon PXRD based Al$_3$Ni$_2$ crystallites size calculations we revealed that atomic diffusion was being accelerated depending on sonication medium. As it can be seen in **Fig. 5.2b** crystallite size of the 1-hour-sonicated Al$_3$Ni$_2$ intermetallic phase is increasing in the row: 95 nm (ethylene glycol) < 130 nm (ethanol) < 200 nm (water) < 225 nm (decane). Crystallite size of the untreated powder is approximately 90 nm. Previously [20], using our data on the crystallite size change we could estimate average grain boundary sliding for the experimental time of 1 hour in AlNi system to approx. 2×10^{-18} m^2/s. This value indicates the event of solid-state diffusion. Thus, we posit that acoustic cavitation reveals itself in creating temperature gradient that is responsible for solid-state atomic diffusion and crystal growth in metal particles.

As we can see from the **Fig. 5.2b** the largest crystallites were obtained for the samples sonicated in decane. Calculated value for the Al_3Ni_2 crystallite size of the 1-hour-sonicated in decane sample indicates that the particles were continuously heated by collapsing cavitation bubbles to a temperature of ~ 580 °C (**Fig. 5.2c**). Thus continuous collapse of cavitation bubbles in decane generated enough energy to create temperature gradient sufficient for acceleration of the atomic diffusion in the metal particles as if they were annealed at 580 °C.
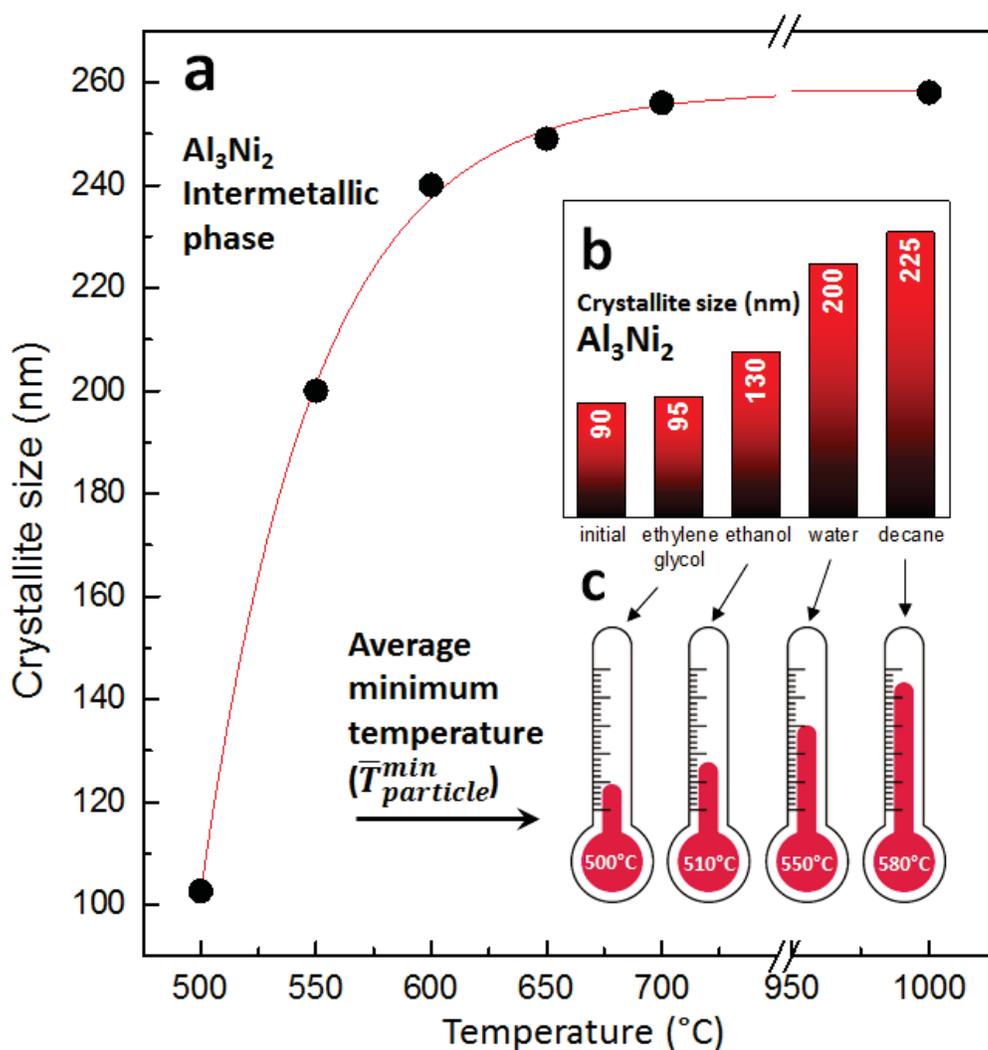
Figure 5.2: *Al$_3$Ni$_2$ intermetallic phase crystallite size after annealing AlNi particles for 1 hour at different temperature (a). Al$_3$Ni$_2$ intermetallic phase crystallite size after 1 hour of HIUS treatment (b) and estimated ($\bar{T}^{min}_{particle}$) (c) in various sonication media.*

Interestingly, ($\bar{T}^{min}_{particle}$) varies depending on the sonication medium and increases in the row ethylene glycol < ethanol < water < decane. Knowing the initial temperature and

determined ($\bar{T}_{particle}^{min}$) after sonication it is possible to compare the efficiency of energy transfer from collapsing cavitation bubbles to metal particles using the following equation [27]:

$$Heat_{(transferred)} = m \times \varDelta T \times Cp \qquad (6)$$

Where m is the mass of sonicated sample, $\varDelta T$ is the temperature difference before and after sonication, and Cp is the heat capacity of the sample. Since the mass and heat capacity of the sample are constant we can estimate the difference in energy transfer efficiency for two sonication media:

$$\frac{Heat_{(transferred)}\ solvent\ 1}{Heat_{(transferred)}\ solvent\ 2} = \frac{\varDelta T\ solvent\ 1}{\varDelta T\ solvent\ 2} \qquad (7)$$

According to the Eq.7 greater temperature difference would result in higher efficiency of the energy transfer. For example, using this equation we estimated that energy transfer between collapsing cavitation bubble and AlNi alloy particles is ~ 17 % more efficient in decane than in ethylene glycol and ~ 13 % than in ethanol.

In order to explain the difference in energy transfer efficiency and ($\bar{T}_{particle}^{min}$) values, a closer look should be given to the effect of cavitation depending on the physical properties of sonication media. It has been reported before that temperature inside the cavitation bubble and strength of the bubble collapse to a high extent depends on vapor pressure of the sonication medium [4, 19]. Higher vapor pressure of the medium results in lower temperature inside the cavitation bubble and weaker collapse. In our case it would mean less efficient energy transfer to the HIUS treated metal particles and, accordingly, lower ($\bar{T}_{particle}^{min}$) values.

In order to investigate the effect of vapor pressure of medium on energy transfer efficiency we sonicated metal particles in the media of various vapor pressures – water / ethanol mixtures and calculated ($\bar{T}_{particle}^{min}$) values using Al_3Ni_2 intermetallic crystallite size (**Fig. 5.3a** (inset)) as an indicator of the temperature change (**Fig. 5.3a**). Indeed, we observed gradual decrease in ($\bar{T}_{particle}^{min}$) values upon vapor pressure increase.
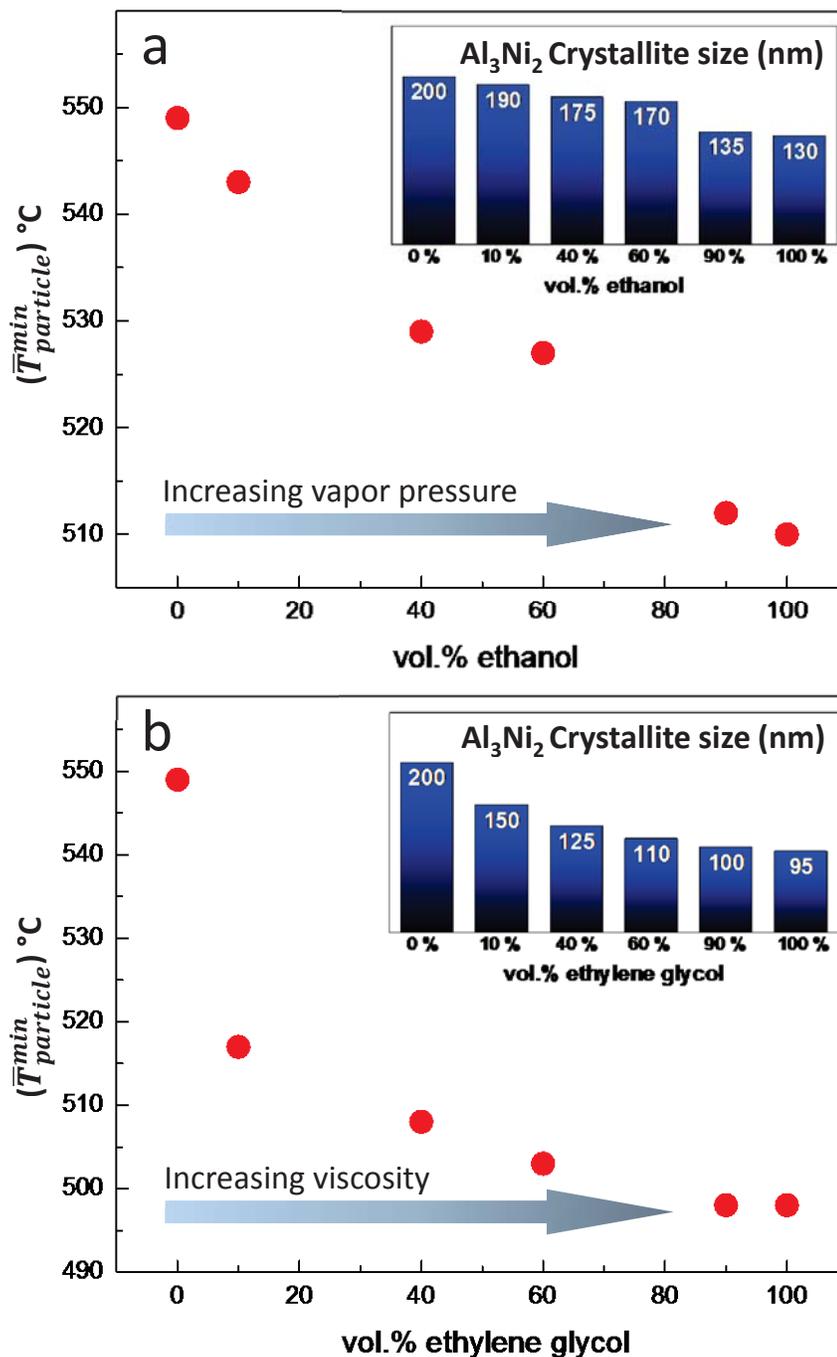
Figure 5.3: *Estimated $(\bar{T}_{particle}^{min})$ of the particles HIUS treated in sonication media with variable volume percent of ethanol in ethanol/water mixtures (a) and ethylene glycol in ethylene glycol/water mixtures (b), as well as used for the temperature estimation their corresponding Al_3Ni_2 intermetallic phase crystallite sizes (insets).*

Another physical property that could influence the efficiency of energy transfer to sonicated matter is viscosity. Higher viscosity of the sonication medium hinders interparticle collisions and thus might inhibit the energy propagation from collapsing cavitation bubble. For

this reason we treated the particles with HIUS in the media of various viscosity – water / ethylene glycol mixtures. As expected, upon monitoring Al_3Ni_2 intermetallic crystallite size (**Fig. 5.3b** (inset)) and correlating it with ($\bar{T}^{min}_{particle}$) we observed (**Fig. 5.3b**) that by increasing viscosity of sonication medium the efficiency of energy transfer to the sonication matter is decreasing which is resulting in lower ($\bar{T}^{min}_{particle}$) values.

Additional important parameter that can influence interparticle collisions ($\bar{T}^{min}_{particle}$) is the particle concentration of the HIUS treated suspensions. To evaluate the effect of concentration we ultrasonicated the different quantities of particles in decane and monitored the Al_3Ni_2 intermetallic crystallite size change (**Fig. 5.4**). Crystallites in the 1-hour-sonicated samples were larger for the more concentrated suspensions. The maximum size of the crystallites (approx. 225 nm) was observed at 10 wt.% concentration of particles. Thus, in more concentrated suspensions more frequent interparticle collisions lead to higher temperature in an ultrasonically treated particle.
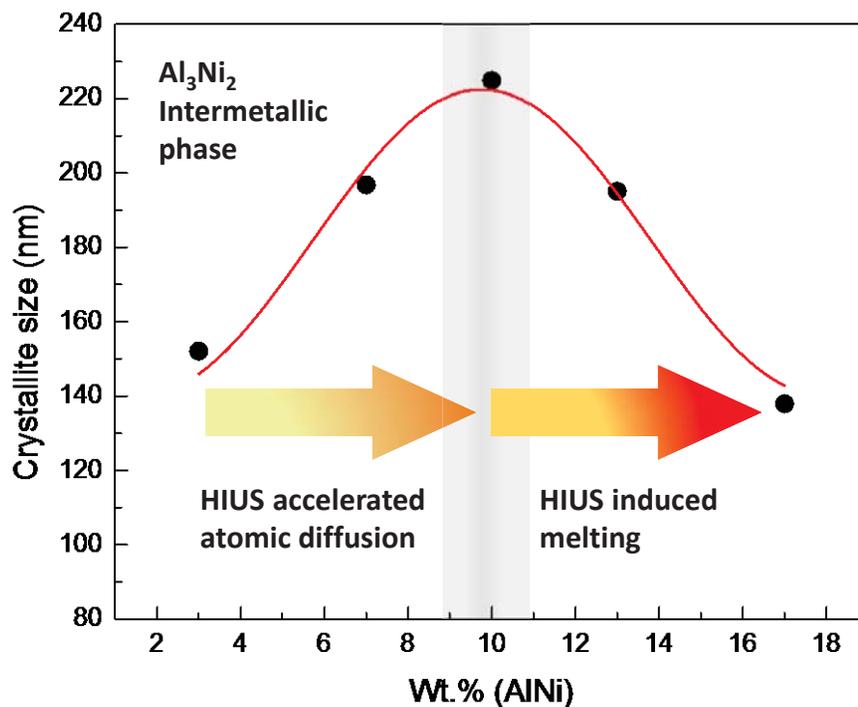
Figure 5.4: *Plot of Al_3Ni_2 intermetallic phase crystallite size depending on the concentration of AlNi particles in decane suspensions for HIUS treatment.*

Interestingly, we observed decrease in crystallite size when metal particle loadings exceeds 10 wt.%. Thermodynamically the process of crystallite reduction can only occur upon

re-melting and following solidification. Moreover, in order to produce smaller grains the melt must be solidified extremely fast limiting the time, which is necessary for crystallite growth to a particular size [28]. Thus, HIUS treatment of the concentrate suspensions (> 10 wt.%) results in the significant increase of $(\bar{T}_{particle}^{min})$ that even exceeds the melting point of the phases in AlNi alloys (1638 °C). Our results are in a good agreement with earlier reports which showed that metal particles could weld together due to frequent and strong interparticle collisions caused by cavitation [18, 29]. Though, in case of suspensions with lower particle content interparticle collisions are less frequent and released upon cavitation bubble collapse energy is spent to accelerate the atomic diffusion. Using crystallite size vs. temperature calibration curve for the annealed samples we estimated that in the region with particle loadings from 3 up to 10 wt.% the temperature change is 58 °C yielding an increase in $(\bar{T}_{particle}^{min})$ of ~ 8 °C with each wt.% of particles added to sonicated decane suspension.

Another proof of possible re-melting of AlNi particles was revealed when decane suspensions of AlNi particles were subject to variable ultrasonic treatment duration (**Fig. 5.5**).
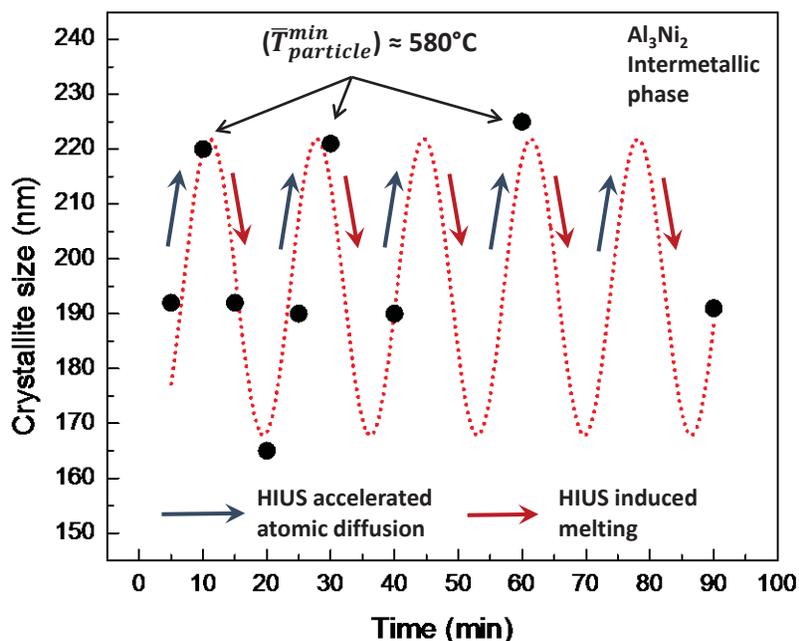
Figure 5.5: *Plot of Al$_3$Ni$_2$ intermetallic phase crystallite size depending on duration of HIUS treatment of 10 wt.% AlNi particles suspension in decane.*

Namely, based on crystallite size evaluation we observed repeating of accelerated atomic diffusion / re-melting cycles depending on the time of HIUS treatment. Thus, on one hand we confirmed that the average minimum temperature $(\bar{T}_{particle}^{min})$ can reach the value of ~ 580 °C

during ultrasound treatment and repeatedly exceed it up to the value of 1638 °C or higher. On the other hand, **Fig. 5.5** confirmed the periodic nature of cavitation bubbles collapse [2] where energy must be repeatedly spent on accumulation of significant number of cavitation bubbles until reaching its critical value. Overall, the energy released from collapsed cavitation bubble can be controllably transferred to the sonication matter through the appropriate choice of sonication medium based on its physical properties such as viscosity and vapor pressure as well as through the adjustment of particle concentration and sonication time to either accelerate the atomic diffusion or force the melting processes.

5.4   Conclusions

Here we reported on applying PXRD based crystallographic properties evaluation method as a tool for providing information about energy transfer between collapsing cavitation bubbles and sonicated matter. We revealed that during HIUS treatment average minimum temperature ($\bar{T}_{particle}^{min}$) depends on physical properties of the sonication medium such as vapor pressure and viscosity and increasing in the row ethylene glycol < ethanol < water < decane. Based on the obtained data we estimated that energy transfer from collapsing cavitation bubble to sonicated particle is ~ 17 % more efficient in decane than in ethylene glycol. Additionally, we showed the influence of particle concentration during ultrasonication. Thus, for suspensions with 10 wt.% particle loading or less we only observed the process of atomic diffusion, while HIUS treatment of more concentrated suspensions (>10 wt.%) led to re-melting processes indicating that ($\bar{T}_{particle}^{min}$) is exceeding the particle melting point.

References

[1] O.V. Abramov, High-Intensity Ultrasound, Gordon and Breach Science Publishers, 1998.

[2] M.A. Margulis, Sonochemistry and Cavitation, Gordon and Breach Publishers, 1995.

[3] J.P. Lorimer, T.J. Mason, Sonochemistry. Part 1-The physical aspects, Chem. Soc. Rev., 16 (1987) 239-274.

[4] J. Rae, M. Ashokkumar, O. Eulaerts, C. von Sonntag, J. Reisse, F. Grieser, Estimation of ultrasound induced cavitation bubble temperatures in aqueous solutions, Ultrason. Sonochem., 12 (2005) 325-329.

[5] V. Misik, N. Miyoshi, P. Riesz, EPR Spin-Trapping Study of the Sonolysis of H2O/D2O Mixtures: Probing the Temperatures of Cavitation Regions, J. Phys. Chem., 99 (1995) 3605-3611.

[6] K.S. Suslick, D.A. Hammerton, R.E. Cline, Sonochemical hot spot, J. Am. Chem. Soc., 108 (1986) 5641-5642.

[7] S. Ramesh, Y. Koltypin, R. Prozorov, A. Gedanken, Sonochemical deposition and characterization of nanophasic amorphous nickel on silica microspheres, Chem. Mat., 9 (1997) 546-551.

[8] R.A. Caruso, M. Ashokkumar, F. Grieser, Sonochemical formation of colloidal platinum, Colloid Surf. A-Physicochem. Eng. Asp., 169 (2000) 219-225.

[9] K.S. Suslick, S.B. Choe, A.A. Cichowlas, M.W. Grinstaff, Sonochemical synthesis of amorphous iron, Nature, 353 (1991) 414-416.

[10] K. Shafi, A. Gedanken, R. Prozorov, Sonochemical preparation and characterization of nanosized amorphous Co-Ni alloy powders, J. Mater. Chem., 8 (1998) 769-773.

[11] R. Katoh, Y. Tasaka, E. Sekreta, M. Yumura, F. Ikazaki, Y. Kakudate, S. Fujiwara, Sonochemical production of a carbon nanotube, Ultrason. Sonochem., 6 (1999) 185-187.

[12] D.G. Shchukin, H. Mohwald, Sonochemical nanosynthesis at the engineered interface of a cavitation microbubble, Phys. Chem. Chem. Phys., 8 (2006) 3496-3506.

[13] N. Pazos-Perez, J. Schaferhans, E.V. Skorb, A. Fery, D.V. Andreeva, Ultrasound driven formation of metal-supported nanocatalysts, Microporous Mesoporous Mat., 154 (2012) 164-169.
[14] E.V. Skorb, H. Mohwald, T. Irrgang, A. Fery, D.V. Andreeva, Ultrasound-assisted design of metal nanocomposites, Chem. Commun., 46 (2010) 7897-7899.

[15] J. Schaferhans, S. Gomez-Quero, D.V. Andreeva, G. Rothenberg, Novel and Effective Copper-Aluminum Propane Dehydrogenation Catalysts, Chem.-Eur. J., 17 (2011) 12254-12256.

[16] J. Dulle, K. Thirunavukkarasu, M.C. Mittelmeijer-Hazeleger, D.V. Andreeva, N.R. Shiju, G. Rothenberg, Efficient three-component coupling catalysed by mesoporous copper-aluminum based nanocomposites, Green Chem., 15 (2013) 1238-1243.

[17] K.S. Suslick, T.W. Hyeon, M.M. Fang, Nanostructured materials generated by high-intensity ultrasound: Sonochemical synthesis and catalytic studies, Chem. Mat., 8 (1996) 2172-2179.

[18] S.J. Doktycz, K.S. Suslick, Interparticle collisions driven by ultrasound, Science, 247 (1990) 1067-1069.

[19] M. Ashokkumar, T. Mason, Sonochemistry, in: Kirk-Othmer Encylcopedia of Chemical Technology, John Wiley & Sons, 2007.

[20] P.V. Cherepanov, I. Melnyk, D.V. Andreeva, Effect of high intensity ultrasound on Al_3Ni_2, Al_3Ni crystallite size in binary AlNi (50 wt% of Ni) alloy, Ultrason. Sonochem., 23 (2015) 26-30.

[21] H. Conrad, J. Narayan, On the grain size softening in nanocrystalline materials, Scr. Mater., 42 (2000) 1025-1030.

[22] P.V. Cherepanov, M. Ashokkumar, D.V. Andreeva, Ultrasound assisted formation of Al-Ni electrocatalyst for hydrogen evolution, Ultrason. Sonochem., 23 (2015) 142-147.

[23] T. Ungar, A. Revesz, A. Borbely, Dislocations and grain size in electrodeposited nanocrystalline Ni determined by the modified Williamson-Hall and Warren-Averbach procedures, J. Appl. Crystallogr., 31 (1998) 554-558.

[24] K. Venkateswarlu, A.C. Bose, N. Rameshbabu, X-ray peak broadening studies of nanocrystalline hydroxyapatite by Williamson-Hall analysis, Physica B, 405 (2010) 4256-4261.

[25] A.K. Zak, W.H.A. Majid, M.E. Abrishami, R. Yousefi, X-ray analysis of ZnO nanoparticles by Williamson-Hall and size-strain plot methods, Solid State Sci., 13 (2011) 251-256.

[26] P.V. Cherepanov, I. Melnyk, E.V. Skorb, P. Fratzl, E. Zolotoyabko, N. Dubrovinskaia, L. Dubrovinsky, Y.S. Avadhut, J. Senker, L. Leppert, S. Kuemmel, D.V. Andreeva, The use of ultrasonic cavitation for near-surface structuring of robust and low-cost AlNi catalysts for hydrogen production, Green Chem, 17 (2015) 2745-2749.

[27] D. Ebbing, S.D. Gammon, General Chemistry, Ninth Edition ed., Houghton Mifflin, 2007.

[28] A. Ilbagi, P.D. Khatibi, I.P. Swainson, G. Reinhart, H. Henein, Microstructural analysis of rapidly solidified aluminium-nickel alloys, Can. Metall. Q., 50 (2011) 295-302.

[29] T. Prozorov, R. Prozorov, K.S. Suslick, High velocity interparticle collisions driven by ultrasound, J. Am. Chem. Soc., 126 (2004) 13890-13891.

6   The use of ultrasonic cavitation for near-surface structuring of robust and low-cost AlNi catalysts for hydrogen production

Pavel V. Cherepanov,[a] Inga Melnyk,[a] Ekaterina V. Skorb,[b] Peter Fratzl,[b] Emil Zolotoyabko,[c] Natalia Dubrovinskaia,[d] Leonid Dubrovinsky,[e] Yamini S. Avadhut,[f] Juergen Senker,[f] Linn Leppert,[g] Stephan Kuemmel,[g] and Daria V. Andreeva [a]*

[a]Physical Chemistry II, University of Bayreuth, DE-95440 Bayreuth, Germany

[b]Max Planck Institute of Colloids and Interfaces, DE-14424 Potsdam, Germany

[c]Department of Materials Science and Engineering, Technion – Israel Institute of Technology, 32000 Haifa, Israel

[d]Materials Physics and Technology at Extreme Conditions, Laboratory of Crystallography, University of Bayreuth, DE-95440 Bayreuth, Germany

[e]Bayrisches Geoinstitut, University of Bayreuth, DE-95440 Bayreuth, Germany

[f]Inorganic Chemistry III, University of Bayreuth, DE-95440 Bayreuth, Germany

[g]Theoretical Physics IV, University of Bayreuth, DE-95440 Bayreuth, Germany.

*Corresponding author e-mail: daria.andreeva@uni-bayreuth.de
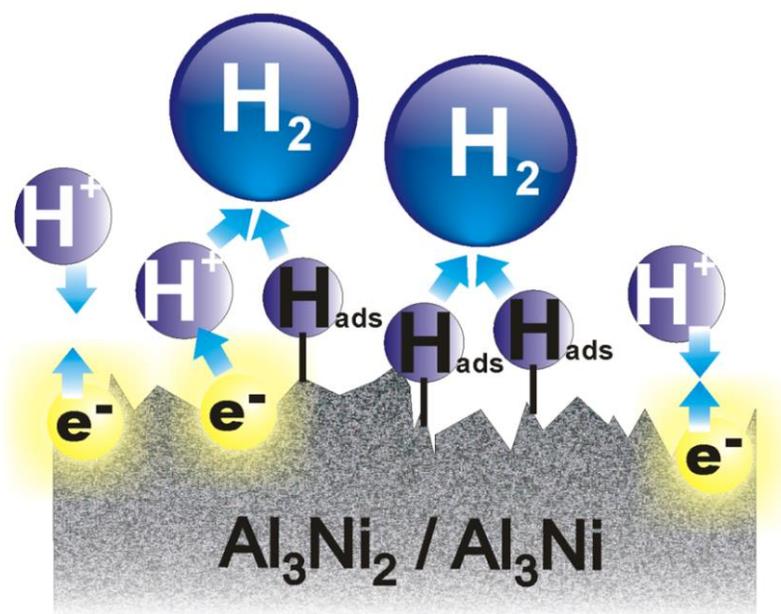
Abstract

Ultrasonically induced shock waves stimulate intensive interparticle collisions in suspensions and create large local temperature gradients in AlNi particles. These trigger phase transformations at the surface rather than in the particle interior. We show that ultrasonic processing is an effective approach for developing the desired compositional gradients in nm-thick interfacial regions of metal alloys and formation of effective catalysts toward the hydrogen evolution reaction.

6.1   Introduction

The hydrogen evolution reaction (HER) is an important technological process for the production of molecular hydrogen through water splitting.[1] Catalysts for the HER reversibly bind hydrogen to their surface.[2] Rapid HER kinetics was observed when utilizing expensive metal catalysts.[3–5] Recently, it was shown that near-surface and surface alloys potentially can have excellent catalytic properties for hydrogen production.[6,7] However, up to now such alloys were prepared by time and energy consuming deposition–annealing procedures using transition metals and the Pt(111) surface.[7,8] In this paper, we propose a novel and efficient ultrasound-assisted approach to the manipulation of the metal alloy surface at the atomic level. We use shock impact of billions of collapsing cavitation bubbles during ultrasonic processing for near-surface phase transformation in AlNi particles, the transformation which can hardly be achieved by conventional methods.

6.2   Results and Disscussion

According to Nørskov *et al.*,[2] the free energy of hydrogen adsorption (ΔG_{H*}) on a catalyst surface is a reliable descriptor of catalytic activity for a variety of compounds. The value of ΔG_{H*} close to zero indicates that hydrogen intermediates are bound neither too strongly nor too weakly to the catalyst surface. In order to disclose which intermetallic phase in AlNi alloys could potentially be active in HER, we calculated the free energy of hydrogen adsorption for AlNi intermetallics (see the ESI† for details of our density functional theory (DFT) calculations).

Fig. 6.1 demonstrates that the HER can proceed nearly thermo-neutrally at the (100)-planes of Al_3Ni_2. In contrast, a value of ΔG_{H*} for the Al_3Ni (010) surface plane is more negative due to pronounced surface reconstruction upon hydrogen adsorption and, hence, this plane can be considered equally inactive as pure Ni.
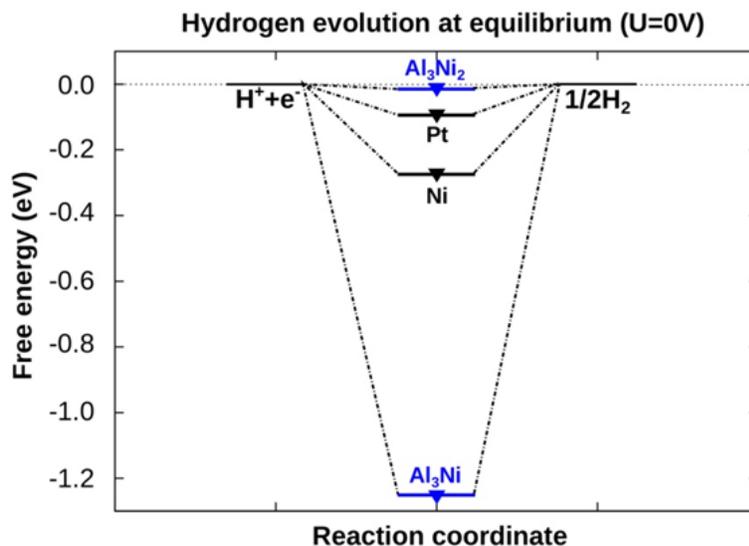

Fig. 6.1: *Calculated free energy diagram for hydrogen evolution at a potential U = 0 relative to the standard hydrogen electrode at pH = 0. Values for Pt and Ni are taken from ref. 33. $Al_3Ni_2(100)$ shows a high potential for the hydrogen evolution reaction.*

The obtained results, therefore, indicate that the $Al_3Ni_2(100)$ phase in our intermetallic system is expected to be the most active for electrocatalysis. By measuring the particles' activity in HER, we can evaluate how accessible the surface of the $Al_3Ni_2(100)$ phase is for H-adsorption.

In order to experimentally evaluate the predicted activity of the intermetallics during water splitting, we tested the functioning of bulk commercial Al_3Ni_2 and Al_3Ni compounds in HER. The HER current/potential profiles are shown in **Fig. 6.2a**.

It is well known that hydrogen production at the surface of efficient electrocatalysts must be characterized with closer to zero overpotential and high current density output. As predicted by our DFT calculations, our experimental results clearly show that the beneficial phase for water splitting is Al_3Ni_2, whereas the Al_3Ni phase binds H too strongly. However, the measured electrocatalytic characteristics of the unstructured bulk Al_3Ni_2 are not as spectacular as predicted by DFT calculations, probably due to the low accessibility of the active $Al_3Ni_2(100)$ planes for hydrogen adsorption. Therefore, the decisive question is whether it is possible to find an efficient method for structuring of the Al_3Ni_2 phase.
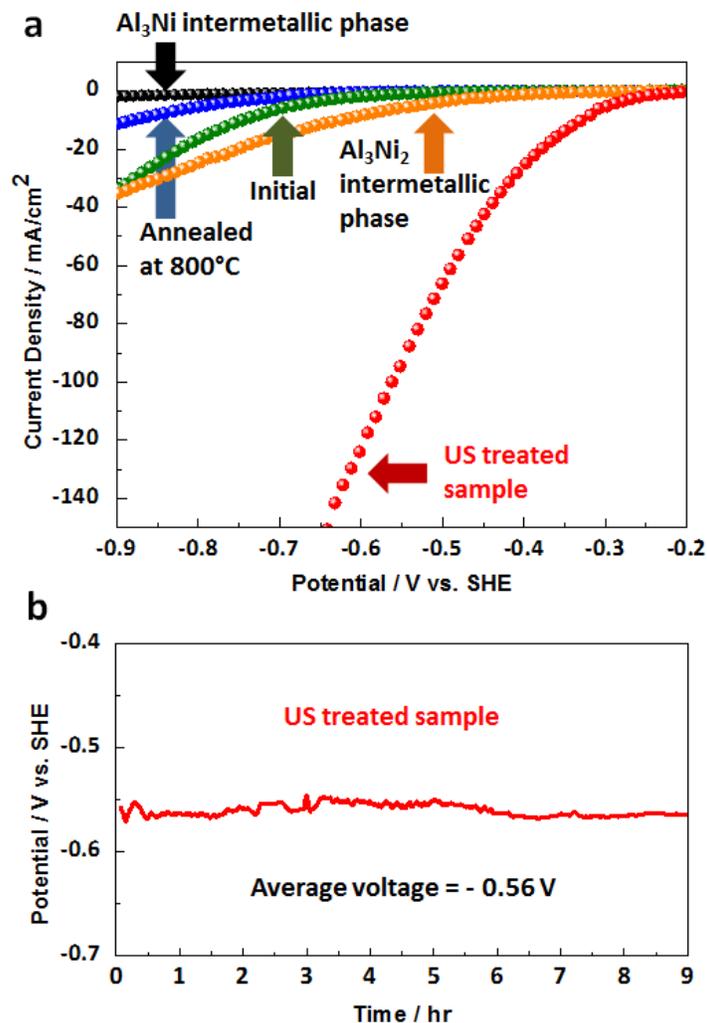
Fig. 6.2: *HER current–potential profiles for the initial and ultrasonically modified AlNi (50 wt.% Ni) alloys, bulk commercial Al$_3$Ni and Al$_3$Ni$_2$ phases, as well as AlNi alloy annealed at 1173 K (a). Galvanostatic HER profile for ultrasonically modified AlNi (50 wt.% Ni) alloy (b).*

Recently, it has been argued that structuring of near-surface regions in metal alloys is of great importance for achieving enhanced catalytic activities of intermetallic compounds.[6] High electrocatalytic activity was observed[7,8] for structured compounds with enhanced accessibility of potentially active crystal planes. Thus, the relatively poor (higher onset overpotential and lower apparent current density values) electrocatalytic behavior of Al$_3$Ni$_2$ can be enhanced by structuring of the AlNi alloys containing the Al$_3$Ni$_2$ hexagonal phase. Upon controlled structuring of intermetallic phases in the AlNi alloy, we do achieve preferential orientation of the

(100) hexagonal crystal planes[9] at the surface and, thus, the enhancement of the Al_3Ni_2 activity toward HER.

According to the AlNi binary phase diagram[10] (**Fig. S1**, ESI†) and the previous work on electrocatalytic application of AlNi compounds[11–14] the best AlNi candidates for the catalyst preparation are AlNi alloys with nearly 50 wt.% of Ni. The Rietveld refinement of the powder X-ray diffraction (PXRD) patterns of the investigated samples showed that this alloy is a mixture of Al (2 wt.%), Al_3Ni (43 wt.%), and Al_3Ni_2 (55 wt.%). However, during alloy preparation from melt, the desirable clustering of Al_3Ni_2 at the surface of Al_3Ni is kinetically restricted due to the preferable nucleation of the Al_3Ni phase on the surface of the already formed Al_3Ni_2 phase. At the same time, the formation enthalpies are $\Delta H \approx -65$ kJ mol^{-1} and $\Delta H \approx -45$ kJ mol^{-1} for Al_3Ni_2 and Al_3Ni, respectively.[15] This means that the Al_3Ni_2 phase is thermodynamically more stable than the Al_3Ni phase. Indeed, according to the equilibrium phase diagram at 1124 K, the Al_3Ni phase can be transformed into the Al_3Ni_2 phase ($\mathbf{Al_3Ni} \xrightarrow{\mathbf{1124K}} \mathbf{Al_3Ni_2 + L_{15,3\ at.\ \%\ Ni}}$).[10] Thus, in principle, it should be possible to trigger the desirable phase transformation by conventional heating. However, the obtained product is not electrochemically active (**Fig. 6.2a**, blue curve), since the highly active surface planes of the (100)-type remain undeveloped. Therefore, a novel technological solution is required for dedicated near-surface phase transformations in AlNi particles.[16–18]

Technologically fast and controllable local heating of a surface can be achieved by the impact of micron-size high-energy cavitation bubbles.[19] Collapsing of cavitation bubbles that are generated in ethanol by high power ultrasound (HPUS) at 20 kHz induces shock waves and intensive turbulent flow.[20–22] In suspensions cavitation triggers intensive interparticle collisions that result in an extremely rapid local rise of the surface temperature of the sonicated particles followed by quenching down to the surrounding medium temperature of 333 K. In this paper, we investigate the HPUS-induced structuring of the intermetallic phases by using ~ 140 μm particles of AlNi alloys suspended in ethanol (for details see ESI†). The catalyst preparation route *via* ultrasonication is sketched in **Fig. 6.3** and explained in the ESI,† **Fig. S3**.
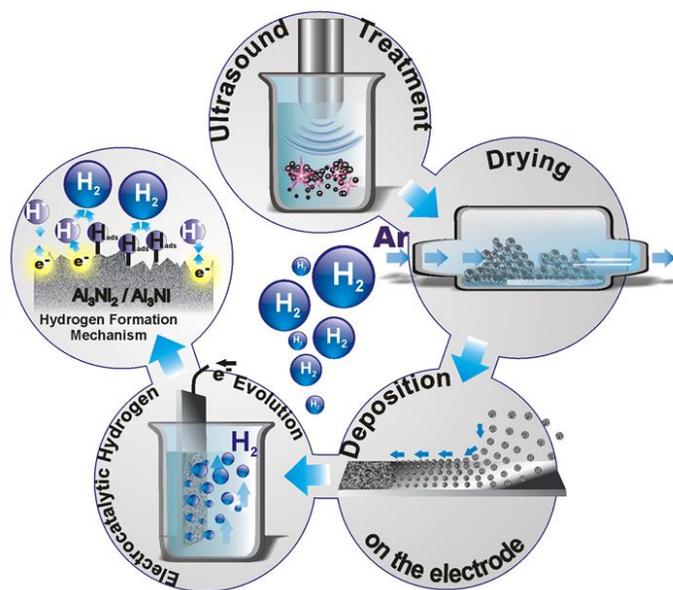
Fig. 6.3: *Schematic illustration of the catalyst preparation procedure. First 10 wt.% suspensions of alloy particles (~ 140 μm) are sonicated in ethanol at a frequency of 20 kHz and an intensity of 140 W cm^{-2} for 1 h. This processing results in the activation of the catalyst surface (change in the crystal structure, phase composition, and morphology). After that the modified particles are centrifuged and dried in an Ar atmosphere. The dried particles are deposited on a substrate and their electrocatalytic activity is evaluated.*

Indeed, the HPUS treatment of AlNi particles causes remarkable modification of the morphology and surface composition in the AlNi alloys. The compositional and morphological changes are clearly visible, when comparing the energy-dispersive X-ray spectroscopy (EDS) results, the ^{27}Al solid state nuclear magnetic resonance (NMR) spectra, X-ray photoelectron spectroscopy (XPS) data and the scanning electron microscopy (SEM) images. The SEM pictures (**Fig. 6.4b**) show the surface roughening after the HPUS treatment. This surface modification is clearly revealed in comparison with the relatively smooth particle surface before the treatment (**Fig. 6.4a**). Furthermore, EDS analysis of the surface composition of the particles before and after sonication shows a mixture of phases near the surface of pristine particles (**Table S2**, ESI†). In contrast, after the HPUS treatment (**Fig. 6.4c** and **d**), EDS detects the presence of a solitary Al_3Ni_2-phase at the surface. Additional evidence of the microstructure refinement in the alloys after the HPUS treatment is provided by selected area electron diffraction (SAED) (see inserts in **Fig. 6.4a** and **b**). The ultrasonically induced clustering of intermetallic phases in the modified AlNi particles is also schematically illustrated in **Fig. 6.4a** and **b**.
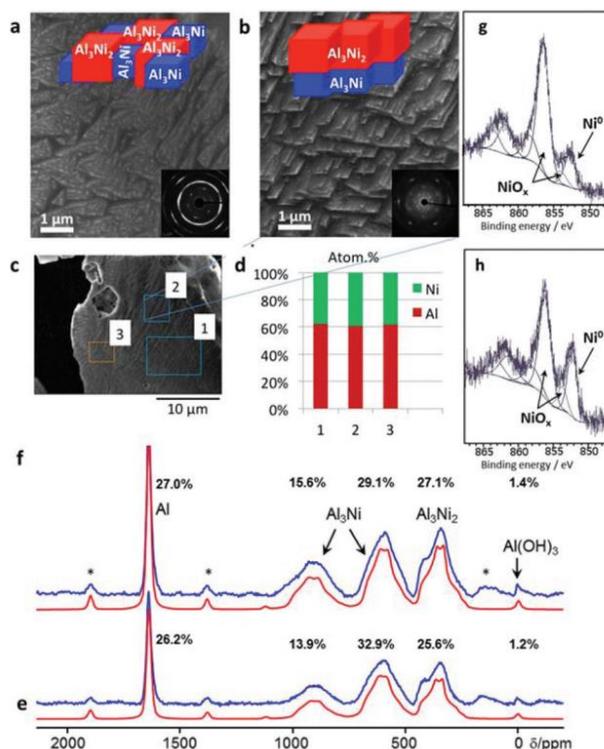
Fig. 6.4: *Scanning electron microscopy images taken from the surface of AlNi (50 wt.% Ni) before (a) and after (b) ultrasonication. The inserts show selected area electron diffraction patterns, which demonstrate the tendency to form larger intermetallic crystals after the HPUS treatment. The sketches illustrate the random phase distribution in the initial AlNi particles and the preferential clustering of the Al_3Ni_2 phase upon the HPUS treatment. Energy dispersive X-ray analysis of the metal surface after ultrasonication proves the formation of Al_3Ni_2 at the surface, where aluminum to nickel ratio is 3 : 2 (c, d). ^{27}Al MAS NMR spectra (blue) of the sample sonicated in ethanol (f) as well as pristine AlNi (e) and their corresponding simulated spectra (red) are shown below, respectively. In addition, the relative intensities of each resonance are indicated (see also Table S1, ESI†). The asterisks denote spinning sidebands. X-ray photoelectron spectra of the initial (g) and modified samples (h).*

The EDS results, as well as the ^{27}Al solid state NMR spectra (**Fig. 6.4e** and **f**) and XPS surface analysis (**Fig. 6.4g** and **h**), provide clear evidence of the spatial re-distribution of the phases within metallic particles after the treatment. Due to the skin effect (see ESI†) the penetration depth of rf fields into conducting and magnetic materials is limited. Thus the ^{27}Al NMR spectra (**Fig. 6.4e** and **f**) enhance the surface content of the AlNi alloy before and after ultrasonication. Both materials exhibit five different resonances (**Fig. 6.4e** and **f**) which are assigned on the basis of the observed chemical shift. The main contribution arises from metallic Al (5.7/5.9 wt.%), Al_3Ni (52.6/50.1 wt.%), Al_3Ni_2 (40.9/43.1 wt.%), and $Al(OH)_3$ (0.8/0.9 wt.%) before and after sonication. While the Al as well as Al_3Ni ratios are slightly higher compared to the results of the

PXRD analysis, the Al_3Ni_2 ratio is lower. This indicates a slight enrichment of Al and Al_3Ni at the surfaces of the alloy particles compared to the bulk composition. Interestingly, sonication increases the surface content of Al_3Ni_2 from 41 to 43 wt.%. In parallel the percentage of Al_3Ni decreases from 52.6 to 50.1 wt.% leading to a decreased Al_3Ni/Al_3Ni_2 ratio from 1.3 to 1.15. This finding supports the hypothesis that Al_3Ni transforms slowly in Al_3Ni_2 during sonication. In contrast, the PXRD patterns showed that the sonication negligibly affected the bulk ratio of the phases in the samples. Furthermore, XPS surface analysis showed the increased concentration of Ni^0 at the surface (**Fig. 6.4h**) upon sonication of AlNi alloy particles in ethanol that also might confirm the formation of the more Ni-enriched Al_3Ni_2 phase compared to Al_3Ni that covers the unmodified surface (**Fig. 6.4g**).

The formation of the Al_3Ni_2 phase on the alloy surface is possible if cavitation bubbles can heat the surface to above 1124 K. At this temperature the catalytically inactive Al_3Ni phase is transferred into the beneficial Al_3Ni_2 phase. The spectroscopic surface analysis before and after the HPUS treatment reveals the formation of the Al_3Ni_2 phase and, thus, proves local surface heating up to ~ 1124 K.

The development of the ultrasonically induced temperature gradient within the particles can stimulate additional crystal growth. We analyzed the PXRD patterns (**Fig. S4**, ESI†) and calculated the crystallite sizes before and after the HPUS treatment using the Williamson–Hall (W–H) method[23–25] (for details, see ESI†). According to our estimations, the Al_3Ni_2 and Al_3Ni crystallites in the HPUS-treated AlNi are nearly twice as large (131 nm for Al_3Ni_2; 113 nm for Al_3Ni) as pristine particles (87 nm for Al_3Ni_2; 56 nm for Al_3Ni). By assuming diffusion-controlled crystal growth during the treatment period (1 h), we estimate the diffusion rate in the AlNi (50 wt.% of Ni) to be about $2 \times 10^{-18}\,\mathrm{m^2\,s^{-1}}$. The reference experiments (heating the particles in an oven for 1 h at different temperatures (for details see **Fig. S5**, ESI†)) showed that the observed atomic diffusion proceeds at an average temperature in the particle interior that is about $T \approx 823$ K.

Surface structuring *via* ultrasonication increases the accessibility of the DFT-predicted beneficial $Al_3Ni_2(100)$ phase for H adsorption, which in turn should enhance the catalytic efficiency toward HER. In fact, we did observe outstanding improvement of the electrocatalytic properties (**Fig. 6.2a**) of AlNi particles after ultrasonication. The onset overpotential *vs.* SHE is significantly lowered to −0.25 V as compared to −0.65 V for pristine AlNi alloy particles. At the same time, the apparent current density values are strongly enhanced. For example, a drastic (more than 200-fold) increase in the current density was observed at an onset overpotential value

of -0.4 V and was found to be 28.19 mA cm^{-2} (HPUS-treated) as compared to 0.13 mA cm^{-2} (initial).

Another very important parameter for evaluating the material's electrocatalytic performance is the exchange current density (i0), which reflects the intrinsic rate of electron transfer between the electrocatalyst's surface and the analyte. Therefore, we replotted the HER current/potential profiles in the Tafel coordinates and calculated i0-values for both the pristine and the HPUS-treated AlNi alloy particles. The calculated i0-value of 17.37 mA cm^{-2} for the HPUS-modified alloy particles is three orders of magnitude higher than for the untreated ones (0.016 mA cm^{-2}). All in all, our study shows that HPUS is a unique technological approach for producing the low-cost and efficient AlNi catalyst for water splitting. The ultrasonically generated AlNi catalyst is very robust and exhibits excellent stability in electrochemical use (**Fig. 6.2b**).

6.2   Conclusions

Using density functional theory, we first predicted that the Al_3Ni_2 phase is potentially effective in the hydrogen evolution reaction. However, bulk unstructured Al_3Ni_2 compounds demonstrated relatively low efficiency due to the low accessibility of the favorable (100) atomic plane. We propose structuring of AlNi alloys containing the Al_3Ni_2 phase as an efficient and low cost technological approach for enhancing the accessibility of the Al_3Ni_2(100) planes that are active in hydrogen adsorption. The formation of the Al_3Ni_2 phase on the surface of AlNi alloys is kinetically restricted, but we demonstrate that processing of the metal surface by ultrasonically generated cavitation bubbles creates large local temperature gradients in the metal particles. These stimulate the desired phase transformations at the surface rather than in the particle interior. In particular, we show that collapsing cavitation bubbles heat the surface above 1124 K, thus triggering the near-surface transformation of the catalytically inactive Al_3Ni phase into beneficial Al_3Ni_2. In the particle interior, the estimated mean temperature reaches 824 K, which is well below the phase transition temperature, but still enough for substantial solid-state diffusion and crystal growth. This simple, fast, and effective ultrasonic approach toward directed surface modification can be extended to other intermetallic systems for sustainable energy generation.

6.3   Experimental

The AlNi (50 wt.% Ni) alloy was prepared by melting Al (99.99 % purity grade) and nickel (99.99 % purity grade) foils (purchased from Sigma-Aldrich) using a Mini ARC melting device MAM-1 (Edmund Bühler Gmbh), TIG 180 DC. The HPUS treatment of AlNi alloy particles was performed using a Hielscher UIP1000hd, (Hielscher Ultrasonics GmbH, Germany) at an operating frequency of 20 kHz. Electrochemical characterization was accomplished in a three electrode cell using a 510 V10 Potentiostat/Galvanostat in the 1 M H_2SO_4 electrolyte. PXRD accompanied by Rietveld refinement, SEM and energy-dispersive EDS and solid state ^{27}Al NMR[26] were employed to verify the phase composition of the prepared AlNi alloys. TEM was used to obtain SAED patterns. DFT calculations were performed using the Vienna ab-initio Simulation Package.[27–32] Detailed information regarding sample preparation, ultrasound treatment, characterization methods, and calculations is available in the ESI.†

Notes and references

1. A. Züttel, A. Borgschulte and L. Schlapbach, *Hydrogen as a future energy carrier*, Wiley-VCH, Weinheim, Germany, 2008

2. E. Skulason, V. Tripkovic, M. E. Björketun, S. Gudmundsdottir, G. Karlberg, J. Rossmeisl, T. Bligaard, H. Jonsson and J. K. Nørskov, *J. Phys. Chem. C*, 2010, **114**, 18182

3. B. Hinnemann, P. G. Moses, J. Bonde, K. P. Jorgensen, J. H. Nielsen, S. Horch, I. Chorkendorff and J. K. Nørskov, *J. Am. Chem. Soc.*, 2005, **127**, 5308

4. T. F. Jaramillo, K. P. Jørgensen, J. Bonde, J. H. Nielsen, S. Horch and I. Chorkendorff, *Science*, 2007, **317**, 100

5. M. S. Faber and S. Jin, *Energy Environ. Sci.*, 2014, **7**, 3519

6. J. Greeley and M. Mavrikakis, *Nat. Mater.*, 2004, **3**, 810

7. A. S. Bandarenka, A. S. Valera, M. Karamad, F. Calle-Vallejo, L. Bech, F. J. Perez-Alonso, J. Rossmeisl, I. E. L. Stephens and I. Cherkendorff, *Angew. Chem., Int. Ed.*, 2012, **51**, 11845 J. Knudsen, A. U. Nilekar, R. T. Vang, J. Schnadt, E. D. L. Kunkes, J. A. Dumesic, M. Mavrikakis and F. Nesenbacher, *J. Am. Chem. Soc.*, 2007, **129**, 6485

8. P. V. Cherepanov, I. Melnyk and D. V. Andreeva, *Ultrason. Sonochem.*, 2015, **23**, 26

9. D. Batalu, G. Cosmeliata and A. Aloman, *Metal. Int.*, 2006, **11**, 36

10. P. V. Cherepanov, M. Ashokkumar and D. V. Andreeva, *Ultrason. Sonochem.*, 2015, **23**, 142

11. D. Miousse and A. Lasia, *J. Appl. Electrochem.*, 1995, **25**, 592

12. P. Los, A. Rami and A. Lasia, *J. Appl. Electrochem.*, 1993, **23**, 135

13. A. Rami and A. Lasia, *J. Appl. Electrochem.*, 1992, **22**, 376

14. D. Shi, B. Wen, R. Melnik, S. Yao and T. Li, *J. Solid State Chem.*, 2009, **182**, 2664

15. A. Ilbagi, P. D. Khatibi, H. Henein, R. Lengsdorf and D. M. Herlach, *J. Phys.: Conf. Ser.*, 2011, **327**,1

16. D. M. Herlach, *Phase transformation in multicomponent melts*, John Wiley & Sons Ltd, 2009

17. J. Dulle, S. Nemeth, E. V. Skorb, T. Irrgang, J. Senker, R. Kempe, A. Fery and D. V. Andreeva, *Adv. Funct. Mater.*, 2012, **22**, 3128

18. B. J. H. Bang and K. S. Suslick, *Adv. Mater.*, 2010, **22**, 1039

19. K. S. Suslick, *Science*, 1990, **247**, 1939

20. S. J. Doktycz and K. S. Suslick, *Science*, 1990, **247**, 1067

21. W. B. McNamara, Y. T. Didenko and K. S. Suslick, *Nature*, 1999, **401**, 772

22. T. Ungar, A. Revesz and A. Borbely, *J. Appl. Crystallogr.*, 1998, **31**, 554

23. K. Venkateswarlu, A. C. Bose and N. Rameshbabu, *Physica B*, 2010, **405**, 4256

24. A. K. Zak, W. H. A. Majid, M. E. Abrishami and R. Yousefi, *Solid State Sci.*, 2011, **13**, 251

25. R. Bhattacharyya, B. Key, H. Chen, A. S. Best, A. F. Hollenkamp and C. P. Grey, *Nat. Mater.*, 2010, **9**, 504

26. G. Kresse and J. Furthmüller, *Comput. Mater. Sci.*, 1990, **6**, 15

27. G. Kresse and J. Furthmüller, *Phys. Rev. B: Condens. Matter*, 1996, **54**, 11169

28. P. E. Blöchl, *Phys. Rev. B: Condens. Matter*, 1994, **50**, 17953

29. J. K. Nørskov, T. Bligaard, A. Logadottir, J. R. Kitchin, J. G. Chen, S. Pandelov and U. Stimming, *J. Electrochem. Soc.*, 2005, **152**, J23

30. H. J. Monkhorst and J. D. Pack, *Phys. Rev. B: Solid State*, 1976, **13**, 5188

31. B. Hammer, L. B. Hansen and J. K. Nørskov, *Phys. Rev. B: Condens. Matter*, 1999, **46**, 7413

32. J. Greeley, T. F. Jaramillo, J. Bonde, I. B. Chorkendorff and J. K. Nørskov, *Nat. Mater.*, 2006, **5**, 909

6.4   Supporting Information

I.   Aluminum-Nickel binary phase diagram

Fig. S1 shows the aluminum-nickel binary phase diagram (Al-Ni BPD). The used composition is 50:50 wt.% (shown by the gray line).
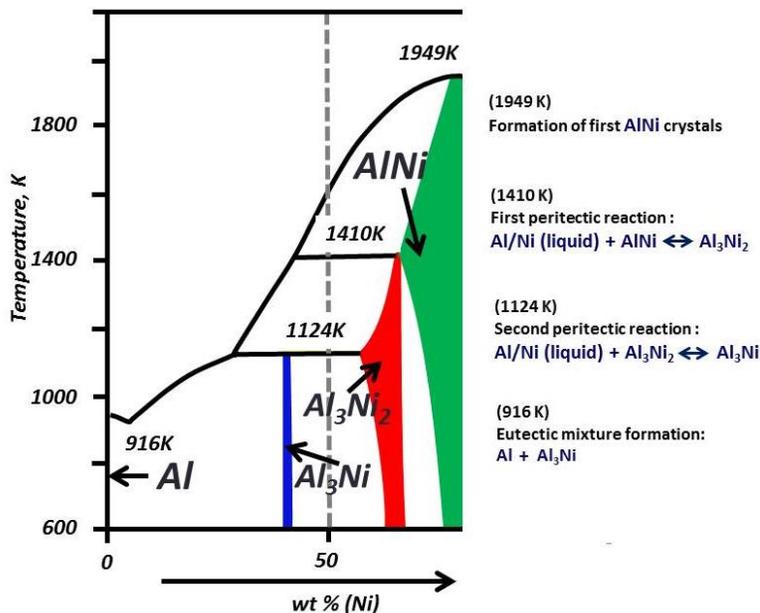
Fig. S1: *Aluminum-nickel binary phase diagram (Ni weight percent ranging from 0 to about 70 wt.%) adopted from Ref.[1]*

II.   Sample preparation

Preparation of metal alloys

Before melting, aluminum and nickel foils (1.0 mm thick, 99.999 % trace metals basis, Aldrich, Germany) of required weight were folded together and pressed into a rectangle-shaped pellet. Upon cooling of the melt, newly prepared alloy was pressed into a plate and folded back to the rectangular shape followed by re-melting. The entire procedure was repeated four times to ensure that aluminum and nickel have been completely mixed. Melting and cooling steps in alloy preparation were performed in argon atmosphere to prevent oxidation. The final alloy plate was processed in the milling machine (Rotormühle Fritsch Pulverisette 14) and meshed towards

obtaining an alloy powder with an average particle size of ~140 μm. The pure intermetallic phases, Al_3Ni_2 and Al_3Ni (~150 μm), have been supplied by Goodfellow GmbH (Germany). The powder X-ray diffractions (PXRD) of the pure phases are shown in **Fig. S2**.
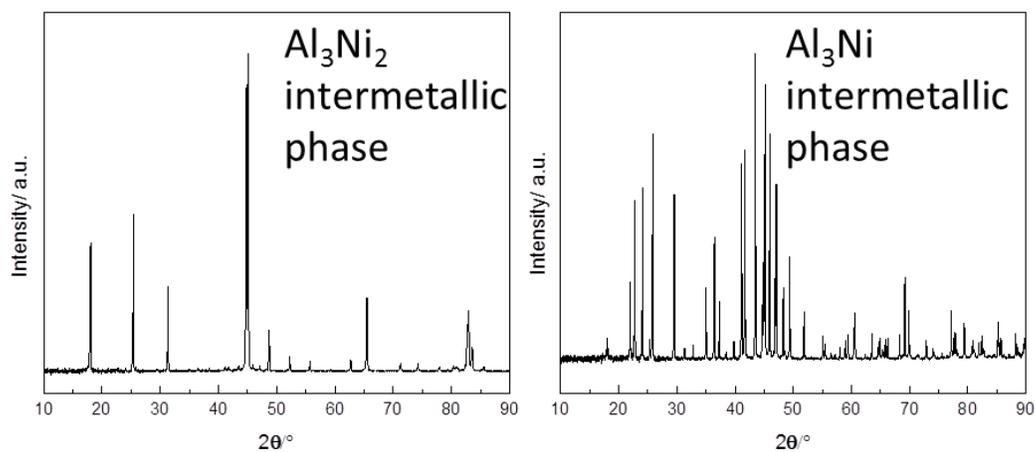
Fig.S2: *PXRD patterns of the pure phases.*

High Power Ultrasound (HPUS) treatment of metal alloys

The sonication cell is shown in **Fig. S3**.
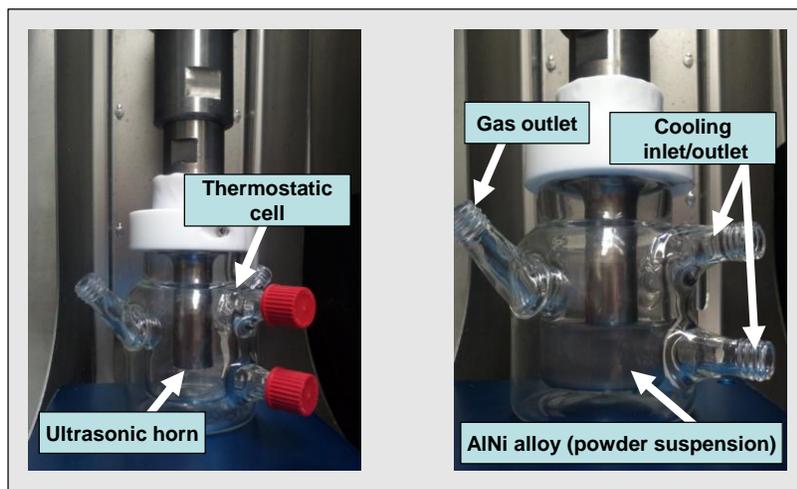
Fig. S3: *Photograph of the cell for HPUS treatment of the AlNi powdered alloys.*

AlNi powder (4 g) was dispersed in 40 mL ethanol and sonicated for 60 min with a Hielscher UIP1000hd, (Hielscher Ultrasonics GmbH, Germany) operated at 20 kHz with a maximum output power of 1000 W. The apparatus is equipped with an ultrasonic horn BS2d22 (head area of 3.8 cm^2) and a booster B2-1.8. The maximum intensity was calculated to be 140 W cm^{-2} at mechanical amplitude of 140 μm. To avoid overheating during sonication the experiment was carried out in a homemade thermostatic cell connected to a thermostat (Huber GmbH, Germany). The temperature was monitored during the treatment and kept at 298 K. After the HPUS treatment, the metal particles were separated from the supernatant by centrifugation at a speed of 10 000 rpm for 1 hour and washed with absolute ethanol followed by drying in vacuum at room temperature.[2]

III.   Sample characterization

Electrochemical characterization

For electrochemical measurements a three-electrode cell consisting of Ag/AgCl/ (saturated KCl) reference electrode (potential was converted to standard hydrogen electrode (SHE)), the Pt foil (6 cm^2) counter electrode, and paraffin impregnated graphite electrode (PIGE) as a working electrode was employed. HIUS modified AlNi alloy particles were immobilized on PIGE with use of Nafion as a binder solution. Linear Sweep Voltammetry (LSV) measurements were performed on a 510 V10 Potentiostat/Galvanostat (MaterialMates, Italy) in the potential region -0.2V to-0.9V with a scan rate of 50mV/s and use of 1M H_2SO_4 as a supporting electrolyte.

To determine lifetime performance of the ultrasonically treated catalyst for HER, galvanostatic responses were recorded at 60 mA/cm^2 for 9 consecutive hours.

^{27}Al Magic Angle Spinning Nuclear Magnetic Resonance (MAS NMR)

The solid state ^{27}Al NMR spectra were recorded on a Bruker AvanceII 300 tuned to a resonance frequency of 78.2 (7.04 T). All magic angle spinning (MAS) NMR experiments were carried out with a commercial 2.5 mm triple resonance MAS probe operating with spinning speed of 20 kHz. The chemical shifts are reported with respect to a solution of $AlCl_3$ adjusted to a pH of 1 with HCl (δ_{iso} = 0 ppm). All spectra were acquired using a single pulse excitation with a pulse length of 1.5 μs and a recycle delay of 0.2 s. To assure a selective excitation of the

central transition, the corresponding nutation frequency was adjusted to 16.7 kHz based on the AlCl$_3$ reference solution.

^{27}Al MAS NMR spectroscopy was used to identify the individual intermetallic phases near the surfaces of the AlNi nanoparticles. The sensitivity towards the surfaces arises from the skin effect.[3] It describes the ability of the radio-frequency (rf) field to penetrate into conducting and magnetic material, respectively. The skin depth, d, is proportional to $\nu_0^{-1/2}$, $\mu_r^{-1/2}$ and $\rho^{1/2}$ with ν_0 being the Lamor frequency, μ_r being the relative permeability and ρ being the electric resistance. While ν_0 is constant for all experiments, ρ and μ_r might vary for the individual Al$_x$Ni$_y$ phases studied here. In particular, μ_r is 2-3orders of magnitude higher for ferromagnetic materials, as compared to Pauli paramagnets, such as metallic aluminum. However, due to the gradual changes observed for the pristine and sonicated materials no strong influence on the skin depth is expected rendering ^{27}Al NMR into a semi-quantitative technique in this case. Thus a tentative interpretation of the spectral intensities in terms of phase composition should be possible.

While metallic Al depicts a sharp resonance at 1640 ppm, Al$_3$Ni is characterized by two broad peaks at 940 ppm and 640 ppm with an intensity ratio of 1:2. Al$_3$Ni$_2$ exhibits single resonance at 340 ppm. All three resonances depict a line shape typical for a second order quadrupolar broadening (**Fig. 4e, f**). The experimental ^{27}Al isotropic chemical shift (δ_{iso}), nuclear quadrupole coupling constants (C_q), anisotropy (η_q), and the individual contributions from each AlNi phases in atomic percentage are tabulated in the **Table S1**.

Table. S1: *^{27}Al NMR chemical shift, nuclear quadrupole coupling constants (C_q), anisotropy (η_q) and the individual contributions (at%) from each phase of AlNi alloy.*

AlNi(50/50)	Parameters	Metallic Al	Al$_3$Ni-site 1	Al$_3$Ni-site 2	Al$_3$Ni$_2$	Al(OH)$_3$
	δ_{iso} / ppm	1638.0	940.0	641.0	340.0	0.0
	C_q / kHz	--	9151.73	9026.70	8822.00	--
	η_q	--	0.55	0.59	0.67	--
Initial	at%	26.23 %	13.9 %	32.94 %	25.65 %	1.23 %
	C_q / kHz	--	9787.72	8948.54	8956.11	--
	η_q	--	0.57	0.60	0.69	--
Sonicated	at.%	27.01 %	15.57 %	29.01%	27.05 %	1.37 %

Electron microscopy

Transmission electron microscopy (TEM) and selected area electron diffractions (SAED) were performed with a LEO 922 EFTEM instrument operating at 200 kV.

Scanning electron microscopy (SEM) and energy dispersive X-ray spectroscopy (EDS) measurements were carried outwith a Gemini Leo 1550 instrument at an operating voltage of 3 keV. The results of surface chemical analysis for the pristine AlNi alloy (50 wt.% of Ni) are shown in **Table S2**.

Table S2. *EDS analysis of the surface of the initial AlNi (50 wt.% Ni) particles.*

Elements, atom.%	Al	Ni	Al:Ni
Analyzed area 1	21.40	28.10	1:1.3
Analyzed area 2	32.70	22.87	3:2
Analyzed area 3	28.75	44.65	2:3

Powder X-ray-diffraction

Powder X-ray diffraction (PXRD) measurements with intermetallic samples were carried out by the aid of a Stoe STADI P X-ray transmission diffractometer, equipped with a Cu sealed tube and built-in Ni filter (Cu Kα radiation, λ = 1.54056 Å). The phase composition was estimated using Rietveld refinement.

The PXRD profiles, as functions of double Bragg angle, 2θ are shown in **Fig. S4**. For extracting important crystallographic information, i.e. crystallite size, D, and average microstrain fluctuations, ε, we used the standard Williamson – Hall (W-H) approach.[4-6]

In the W-H method, the measured widths, β_{hkl}, of diffraction peaks with Miller indices, *hkl*, (after applying instrumental correction), are presented in the following form:

$$\beta_{hkl}\cos\theta = \left(\frac{k\lambda}{D}\right) + (4\varepsilon\sin\theta)$$

where shape factor k = 0.94. It is worth to mention that only non-overlapping diffraction peaks were used by us for this analysis. The classical W-H equation assumes that the microstrain fluctuations, ε, are independent of crystallographic direction.
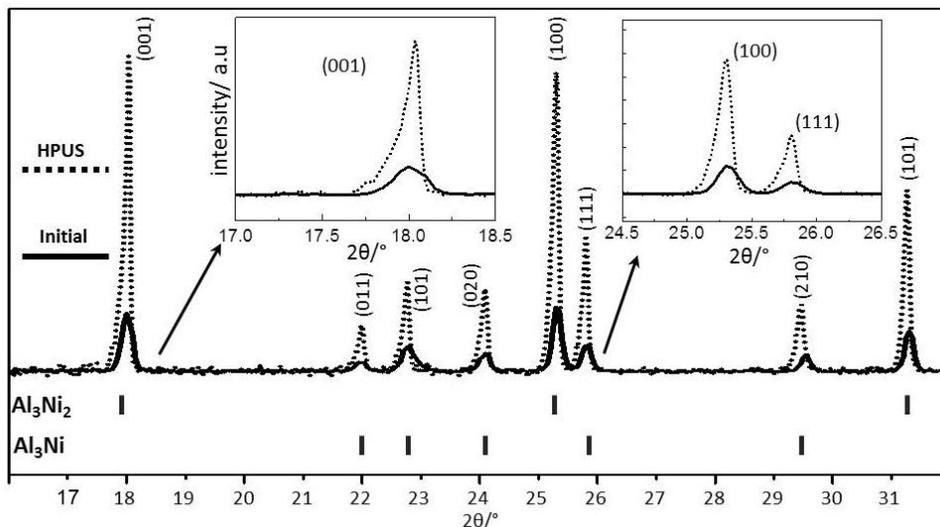

Fig. S4: *Powder X-ray diffraction patterns of the initial (solid line) and ultrasonically modified (dashed line) AlNi (Ni$_{50\,wt.\%}$) with evidence for peak narrowing (insets).*

The temperature effect on crystal size of the intermetallics in AlNi particles

Fig. S5 shows the dependence of the crystal sizes of Al$_3$Ni$_2$ and Al$_3$Ni phases in the samples that were heated in oven for 1 h at different temperatures. We see that up to 700 °C the size of the crystals strongly depends on the applied temperature, while above this temperature some kind of saturation is reached. Placing the crystal size of the sonicated samples on this plot, we can estimate the effective temperature that is achieved within metal particles upon HPUS. Thus estimated average effective temperature in the sonicated particles was found to be about ~550 °C (823 K).

As is seen in the right-hand panel in Figure S5, above 800 °C (1073 K) the Al$_3$Ni phase is disappeared, i.e. is transformed into the Al$_3$Ni$_2$ phase. Thus, ultrasonication is able to selectively convert the catalytically ineffective Al$_3$Ni phase into beneficial Al$_3$Ni$_2$ phase in the interfacial region of the AlNi particles.
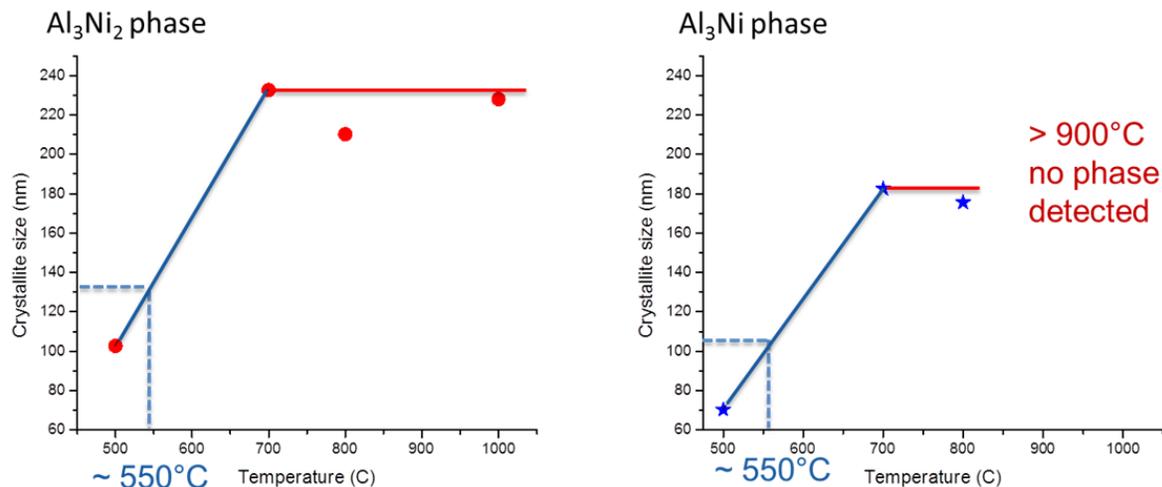
Fig. S5: *Crystal size vs. particle temperature: the samples were heated at selected temperatures for 1 h. Duration of the heat treatment in the oven is equal to that for the particle treatment by HPUS. The crystal sizes for Al₃Ni₂ and Al₃Ni phases, indicated by dashed lines, correspond to those measured by PXRD in the HPUS treated samples.*

DFT Calculations

We performed density functional theory calculations using the Vienna ab-initio Simulation Package (VASP).[7] Ionic cores were described within the projector augmented waves formalism.[8] As we want to compare our free energies of hydrogen adsorption to literature values we used a similar setup and computational parameters as in Ref.[9, 10] With this we obtain a free energy of -0.08 eV for hydrogen adsorption on Pt(111) which agrees with the literature value[9] within 0.01 eV. We used a kinetic energy cutoff of 400 eV and 4x4x1 Monkhorst-Pack k-point meshes[11] in all calculations. Hydrogen adsorption energies were calculated using a periodically repeated surface slab model. To minimize spurious interactions, the vacuum region between neighboring supercells was chosen to be 20 Å. Additionally, dipole corrections were used. All energies were calculated self-consistently using the RPBE exchange-correlation functional.[12] We tested all possible hydrogen adsorption positions both on the Al₃Ni(010) surface (both sides of the slab are equivalent) and on both sides of the Al₃Ni₂(100) surface. A local geometry optimization was performed in all cases. Optimizations were considered as converged when the forces on all atoms were smaller than 0.02 eV/Å. For both compounds the surface cell was repeated twice in the directions parallel to the surface and three times in the direction normal to the surface. In each case, the positions of the atoms in the bottom two surface layers were kept

fixed while the top layer was allowed to relax. We checked that letting the top two layers relax changes the hydrogen adsorption energy by less than 0.01 eV. The hydrogen adsorption energy was calculated as $\Delta E_H = E(surf+H) - E(surf) - 1/2E(H_2)$. For both compounds the energetically most favorable hydrogen position is on top of the highest lying Al atom of the surface cell. To obtain the free energy diagram shown in Fig. 1, we followed Ref.[8] and calculated the free energy of the adsorbed state as $\Delta G_{H*} = \Delta E_H + \Delta E_{ZPE} - T\,\Delta S_H$, where ΔE_{ZPE} is the difference of zero point energies between the adsorbed state and the gas phase state. The vibrational entropy of the adsorbed state is considered small so that $\Delta S_H \cong -0.5 \cdot S^0_{H_2}$, which is the entropy of H_2 in the gas phase at standard conditions (see Ref.[9] and references therein). The vibrational frequencies of H adsorbed on Al_3Ni_2 are 1816 cm^{-1}, 454 cm^{-1} and 367 cm^{-1}, which leads to a ΔE_{ZPE} of 0.03 eV and thus $\Delta G_{H*} = \Delta E_H + 0.23$ eV. This value is also taken for hydrogen adsorption on Al_3Ni.[9,10]

References

1. D. Batalu, G. Cosmeliata, A. Aloman, *Metalurgia Inter.* 2006, **11**, 36.
2. J. Dulle, S. Nemeth, E. V. Skorb, T. Irrgang, J. Senker, R. Kempe, A. Fery, D. V. Andreeva, *Adv. Func. Mater.* 2012, **22**, 3128.
3. R. Bhattacharyya, B. Key, H. Chen, A. S. Best, A. F. Hollenkamp, C. P. Grey, *Nat. Mater.* 2010, **9**, 504.
4. T. Ungar, A. Revesz, A. Borbely, *J. Appl. Crystallogr.* 1998, **31**, 554.
5. K. Venkateswarlu, A. C. Bose, N. Rameshbabu, *Physica* 2010, **B405**, 4256.
6. A. K. Zak, W. H. A. Majid, M. E. Abrishami, R. Yousefi, *Solid State Sci.* 2011, **13**, 251.
7. (a) G. Kresse, J. Furthmüller, *Comput. Mater. Sci.* **1990**, *6*, 15; (b) G. Kresse, J. Furthmüller, *Phys. Rev.* 1996, **B54**, 11169.
8. P. E. Blöchl, *Phys. Rev.* 1994, **B50**, 17953.
9. J. K. Nørskov, T. Bligaard, A. Logadottir, J. R. Kitchin, J. G. Chen, S. Pandelov, U. Stimming, *J. Electrochem. Soc.* 2005, **152**, J23.
10. B. Hinnemann, P. G. Moses, J. Bonde, K. P. Jorgensen, J. H. Nielsen, S. Horch, I. Chorkendorff, J. K. Nørskov, *J. Am. Chem. Soc.* 2005, **127**, 5308.
11. H. J. Monkhorst, J. D. Pack, *Phys. Rev.* 1976, **B13**, 5188.
12. B. Hammer, L. B. Hansen, J. K. Nørskov, *Phys. Rev.* 1999, **B46**, 7413.

7 Ultrasound assisted formation of Al-Ni electrocatalyst for hydrogen evolution

Pavel V. Cherepanov,[a]* Muthupandian Ashokkumar,[b] and Daria V. Andreeva[a]

[a]Physical Chemistry II, University of Bayreuth, DE-95440 Bayreuth, Germany

[b]The School of Chemistry, University of Melbourne, Melbourne, Victoria 3010, Australia

*Corresponding author e-mail: pavel.cherepanov@uni-bayreuth.de

Abstract

High intensity ultrasound treatment has been used to generate electrocatalytically active (towards hydrogen evolution) surface on AlNi (50 wt.% Ni) alloy particles. Acoustic cavitation is responsible for the initiation of redox processes on the catalyst surface leading to changes in its composition. Cavitation impact on the surface composition of the metal alloy could be controlled by manipulating the sonication medium during ultrasound treatment. Evaluation of electrocatalytic performance, as well as surface composition studies of ultrasonically generated catalysts showed the advantageous use of sonication medium with reducing ability and high vapor pressure for the generation of highly efficient interface on Al-Ni alloy particles for water splitting reaction.

7.1 Introduction

Hydrogen is the simplest molecule in our universe, yet it has the largest energy density over any other fuel [1] and is considered to be an excellent energy carrier [2, 3]. Over the last few decades it was successfully used as a fuel for propelling space ships and rockets into orbit. One of the biggest advantages of using hydrogen as a fuel is its non-contaminating nature – the only product during combustion reaction is water, which can be collected and used where necessary. Apart from rocket fuel and hydrogen fuel cells [4, 5], it is also widely used for

ammonia production [6] which is later converted into fertilizers for agricultural needs. The majority (~95 %) of hydrogen is produced today by steam reforming of fossil fuel [7] such as natural gas, petroleum, and coal. The second most popular method of hydrogen production is electrolytic water splitting [8] which accounts only for about ~4 % of the total production, due to the high overpotential (-1.48 V) of hydrogen evolution reaction (HER) [9]. Currently, the only material that can reduce such a large overpotential is platinum [10, 11]. Nevertheless, there have been extensive studies among researchers all over the world on the subject of finding less expensive catalyst than platinum, which could efficiently catalyze the process of HER [12-14]. One of the non-noble metal alternatives is Ni [15].

It has been shown that nickel, nickel-based alloys, as well as aluminum-nickel intermetallic compounds are very promising electrocatalytic materials [12, 16, 17]. Although, quite often methods used for AlNi electrocatalyst formation or activation, namely sintering of metal powders at high temperatures and pressure [18], composite electrodeposition, and plasma spraying [19] of nickel powders are lengthy and complex. Laisa et al. [17-19] have shown that heating of AlNi powders above melting point of Al increased the electrocatalytic activity of the samples due to stimulation of diffusion of Al into Ni. It has been also reported [17] that the large surface roughness, grain sizes, and enrichment of Al_3Ni_2 phases in the activated AlNi alloys could be responsible for the formation of efficient AlNi-based electrocatalyst.

Among all methods used for formation of efficient electrocatalysts, there have been no reports on use of high intensity ultrasound (HIUS) for creation of electrocatalytically active materials towards HER. Previously we had shown that ultrasonically treated metal alloy particles in water can be used as an efficient hydrogenation/dehydrogenation catalyst [20, 21]. HIUS modification resulted in the development of high surface area and phase redistribution [22] on the particle surface due to sonochemical and sonomechanical effects of acoustic cavitation [23]. We have also shown that HIUS treatment of metal particles in water resulted in the continuous surface oxidation of metals by the acoustic cavitation generated OH radicals. Formation of a metal oxide phase may have a positive influence on the formation of composites with high surface area and the high catalytic activity and the stability of the AlNi catalysts [22, 24]. However, for HER the oxide phase deactivates the surface of the AlNi catalyst.

Recently, we have demonstrated [25] that HIUS treatment of AlNi particles in ethanol, which is known as a reducing agent and a scavenger of OH radicals [26], changes the crystal

morphology of the intermetallic phases but does not trigger oxidation of metal and, thus, passivation of electrode's surface. In order to reveal the effect of reducing and oxidative ability of media on the ultrasonically driven activation of the metal surface we modified AlNi particles using various sonication media such as water, water-ethanol mixtures, and ethanol. We should note that all used in the present work sonication media possess different vapor pressures with water being the lowest and ethanol being the highest. Even though redox processes play definitely a key role in the modification pathways of metal surfaces we should not exclude an influence of vapor pressure of the sonication medium on the modification process. It has been reported that the use of sonication medium with higher vapor pressure results in a lower temperature inside the cavitation bubble and the collapse intensity is weaker [27, 28]. In addition, organic solutes react with OH radicals (generated in aqueous medium) leading to the generation of secondary reducing radicals.

The aim of present study was to investigate effect of reducing / oxidative ability of the sonication medium during US treatment affects the efficiency of an inexpensive electrocatalyst AlNi (50 wt.% Ni) alloy particles towards HER . In order to control the properties of the sonication medium during high intensity US treatment, ethanol, water, and ethanol − water mixtures were used. Evaluation of electrocatalytic activity was performed by linear sweep voltammetry. Influence of the solvent during HIUS treatment on bulk compositional content of modified AlNi particles was analyzed by powder X-ray diffraction, while surface morphology and composition were investigated using scanning electron microscopy and X-ray photoelectron spectroscopy.

7.2   Experimental section

Aluminum − Nickel (50 wt.% Ni) alloy powder with average particle size of ~140 μm was purchased from Fluka as well as anhydrous ethanol. All chemicals were the highest purity grade available and were used as received without further purification.

AlNi alloy powder (4 g) was dispersed in 40 mL of ethanol, water, or ethanol/water mixtures and sonicated for 60 min with a Hielscher UIP1000hd, (Hielscher Ultrasonics GmbH, Germany) operated at 20 kHz with a maximum output power of 1000 W. The apparatus was equipped with an ultrasonic horn BS2d22 (tip surface area of 3.8 cm^2) and a booster B2-1.8. The

maximum intensity was calculated to be 140 W cm^{-2} at mechanical amplitude of 106 μm. To avoid overheating during sonication the experiment was carried in a homemade thermostatic cell connected to a thermostat (Huber GmbH, Germany). The temperature was monitored during the treatment and did not exceed 338 K. After HIUS treatment metal particles were separated from the solution by centrifugation at a speed of 10 000 rpm for 1hr and washed with absolute ethanol followed by drying under vacuum at room temperature.

Powder X–ray diffraction (PXRD) analysis of the samples was performed using Stoe STADI P X – ray transmission diffractometer (CuKα radiation from the copper target using an in built nickel filter, λ = 1.54056 Å)

Scanning electron microscopy (SEM) measurements were carried out with a Gemini Leo 1550 instrument at an operating voltage of 3 keV.

For electrochemical measurements a three-electrode cell consisting of Ag/AgCl/ (saturated KCl) reference electrode, the Pt foil (6 cm^2) counter electrode, and paraffin impregnated graphite electrode (PIGE) as a working electrode was employed. HIUS modified AlNi alloy particles were immobilized on PIGE with use of Nafion as a binder solution. Linear Sweep Voltammetry (LSV) measurements were performed on a 510 V10 Potentiostat/Galvanostat (MaterialMates, Italy) in the potential region -0.4 V to -1.1 V with a scan rate of 50 mV/s and use of 1M H_2SO_4 as a supporting electrolyte.

BET analysis**.** The specific surface area of the samples was determined with Micromeritics ASAP 2000 surface area analyzer. All samples were evacuated at 120 °C for 8 hours before nitrogen adsorption.

XPS analyses were carried out using a M-probe apparatus (Surface Science Instruments). The source was monochromatic Al-Kα radiation (1486.6 eV)

7.3   Results and discussion

7.3.1. Electrochemical performance

Fig. 7.1 shows the current – potential HER profiles for AlNi (50 wt.% Ni) alloy particles modified with high intensity ultrasound in various sonication media: ethanol, water, and ethanol – water mixtures. The sonication times were 60 min for all experiments. Flat regions of the

curves show the absence of electron flow in the catalyst/electrolyte interface. Once the sufficient onset overpotential is reached, current increase is observed indicating initiation of electrocatalytic hydrogen formation process. Clearly, lower overpotential values for electrocatalyst are preferable. For the sample treated in ethanol we observed noticeable current increase when the potential reached about -0.7 V with formation of the first hydrogen bubble at as low as -0.6 V. Thus, HIUS treatment in ethanol has significantly lowered the overpotential required to initiate HER comparing to untreated AlNi alloy particles.
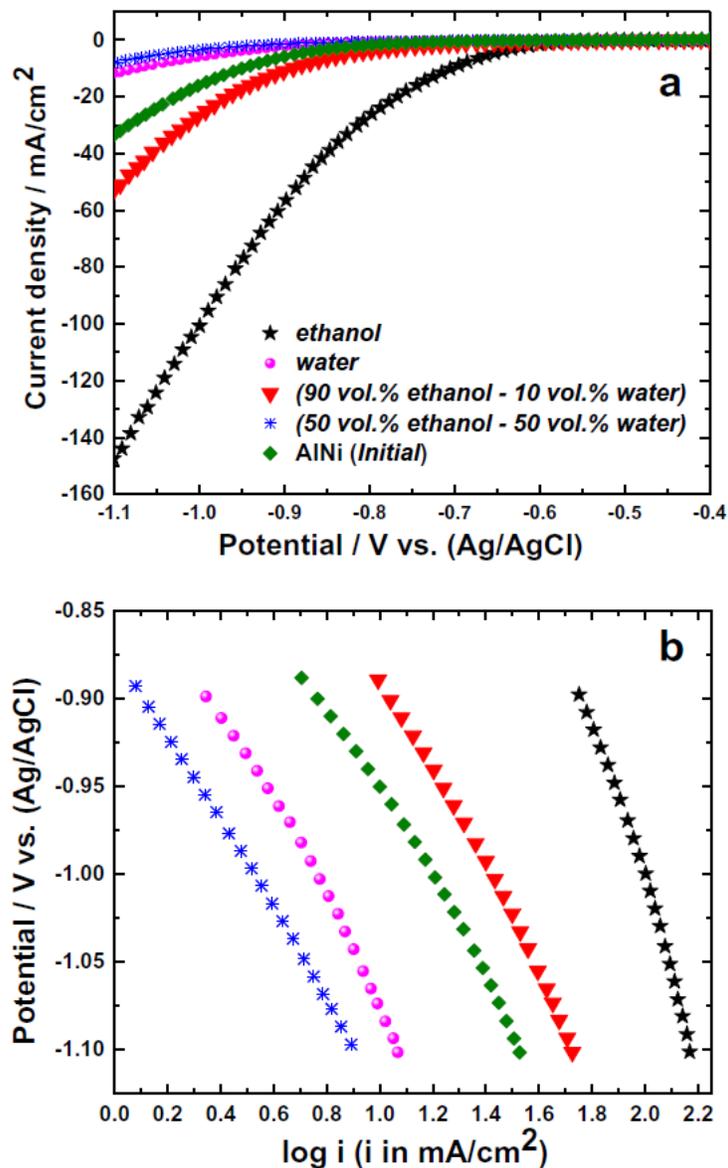
Figure 7.1: *HER current-potential profiles (a) and Tafel plots (b) for the initial and HIUS treated in different sonication media AlNi (50 wt. % Ni) alloy particles. (Legend is valid for both: (a) and (b) parts of the figure).*

Table 7.1 summarizes the apparent current densities at selected potentials of -0.7 V and -1.1 V for the US treated in various sonication media AlNi alloy particles. We observed that electrocatalytic performance of the samples directly depends on sonication media used for AlNi alloy particles modification. More specifically, increase of the ethanol content in water – ethanol mixture leads to a significant enhancement of electrocatalytic properties. As it can be seen from **Fig. 7.1a**, use of solution that contains as little as 10 vol.% of water and 90 vol.% of ethanol during sonication drastically inhibits HER. Therefore, we realized that for creation of an efficient electrocatalyst pure ethanol should be used as a sonication medium and any water addition, which is responsible for the formation of electrocatalytically inactive $Al_2O_3 \cdot nH_2O$ phase, must be avoided.

Table 7.1: *Values for apparent current densities and exchange current densities for the initial and HIUS treated in different sonication media AlNi (50 wt.% Ni) alloy particles at selected potentials.*

Sonication medium	(-0.70 V) Apparent current (mA/cm^2)	(-1.10 V) Apparent current (mA/cm^2)	Exchange current density i_0 (mA/cm^2)
water	0.13	11.69	0.0078
water (50 vol.%) – ethanol (50 vol.%)	0.13	9.27	0.0020
water(10 vol.%) – ethanol (90 vol.%)	1.49	53.16	0.0427
ethanol	10.11	147.43	2.26
Initial AlNi alloy (without treatment)	0.47	33.67	0.0155

In order to evaluate electrocatalytic performance of modified AlNi particles further, we replotted HER profiles in Tafel coordinates (**Fig. 7.1b**) and calculated exchange current density (i_0) values (**Table 7.1**) which represent the intrinsic rate of electron transfer between analyte and electrocatalyst. The (i_0) value for untreated AlNi alloy particles was calculated to be 0.0155 mA/cm^2, which is relatively low for the electrocatalyst to be considered as an efficient one. Nevertheless, HIUS treatment of AlNi alloy particles in ethanol resulted in nearly 146-fold increase in (i_0) and was 2.26 mA/cm^2. On the other hand HIUS treatment in water decreased the (i_0) to almost half (0.0078 mA/cm^2). Overall, our study has revealed that use of ethanol as a sonication medium for creation of an electrocatalyst with significantly improved properties toward HER is extremely promising.

7.3.2. Effect of high intensity ultrasound on composition and morphology

In order to evaluate whether there have been compositional changes (responsible for the observed enhancement in the efficiency) in AlNi alloy particles upon US treatment and how they could affect electrocatalytic performance, we performed PXRD analysis of the sonicated samples.
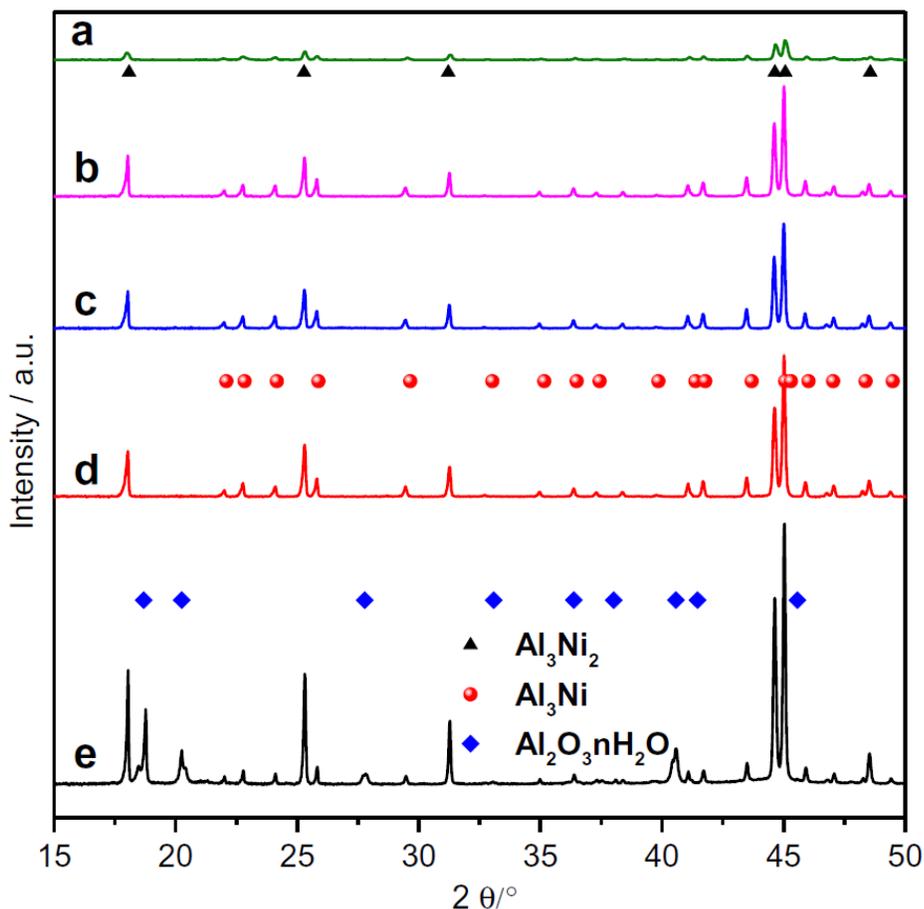
Figure 7.2: *The XRD patterns for the initial (a) and HIUS treated in different sonication media AlNi (50 wt.% Ni) alloy particles: ethanol (b); 90 vol.% ethanol / 10 vol.% water (c); 50 vol.% ethanol / 50 vol.% water (d); water (e).*

Fig. 7.2(a-e) shows the PXRD patterns for the AlNi alloy particles sonicated in various media. In all patterns, we observed peaks which could be identified either as Al_3Ni_2 or Al_3Ni intermetallic phases found in standard reference data (JCPDS: 00-014-0648) and (JCPDS: 00-002-0416) with only one exception for the sample US treated in water (**Fig. 7.2e**) where in addition to the two intermetallic phases, $Al_2O_3 \cdot nH_2O$ phase was also detected. Extremely poor electrocatalytic performance of AlNi alloy particles sonicated in water can be attributed to the non-conductive aluminum hydroxide phase formation. It can be suggested that aluminum

hydroxide phase is formed due to sonochemical aspect of cavitation, viz., the formation of highly oxidative OH radicals. Further, the addition of ethanol as a scavenger of OH radicals should decrease the amount of $Al_2O_3 \cdot nH_2O$. Indeed, $Al_2O_3 \cdot nH_2O$ was not detected in samples prepared in the presence of ethanol **Fig. 7.2(b-d)**.

Even though PXRD provides valuable information about bulk composition and such crystallographic properties as crystallite size and microstrain, additional surface analysis is needed. For this reason, we carried BET analysis to obtain information about surface area of the sonicated samples. **Table 7.2** lists the surface areas for all samples. It can be seen from the table that an increase of the amount of water content in ethanol / water mixture results in significantly higher surface area values. We propose that additionally to partial oxidation of metals in the aqueous medium and the formation of the porous metal oxide, physical properties of water might also affect the modification process. In water, due to relatively low vapor pressure, the cavitation bubble collapse intensity is strong leading to the formation of higher number of pits and hence an increased surface area. However, formation of the oxide layer is responsible for the poor electrochemical performance of the catalyst. In addition, it is probable that hydrogen gas is trapped inside the pores leading to a lower activity - large contact area of newly formed hydrogen bubble preventing it from detachment off the electrocatalyst surface and letting new hydrogen bubble to grow [15].

Table 7.2: *Surface composition and surface area values for the initial and HIUS treated in different sonication media AlNi (50 wt.% Ni) alloy particles.*

Sonication medium	Surface composition (at. %)				Surface area (m^2/g)
	Al	AlOx	Ni	NiOx	
water	-	36.52	-	-	125.1
water (50 vol.%) – ethanol (50 vol.%)	-	33.98	-	0.23	47.9
water(10 vol.%) – ethanol (90 vol.%)	-	30.06	-	0.66	0.3
ethanol	4.52	19.74	0.25	0.42	0.3
Initial AlNi alloy (without treatment)	-	16.67	0.08	0.73	0.2

According to the results summarized in **Table 7.2,** AlNi alloy particles HIUS modified in water (surface area 125 m^2/g) and in 50/50 vol. % ethanol / water mixture (surface area 48 m^2/g) would not be expected to posses enhanced electrocatalytic properties in comparison to initial (unmodified) AlNi alloy particles due to surface passivation by metal oxide. This is in good

agreement with HER experimental data. Moreover, **Fig. 7.3 (a-e)** provides SEM images of initial and HIUS modified alloy particles, which demonstrate relatively smooth surface morphology of the initial particles, and the HIUS treated in ethanol samples. In contrast, the samples treated in water exhibit rough surface morphology due to the formation of metal oxide phase.
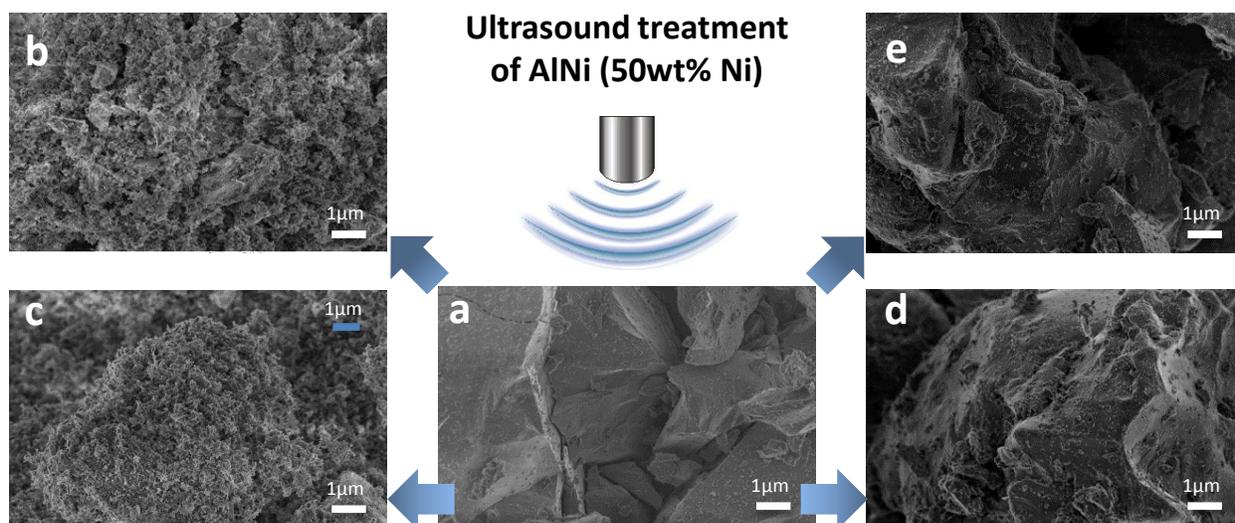

Figure 7.3: *SEM images for the initial (a) and HIUS treated in different sonication media AlNi (50 wt.% Ni) alloy particles: water (b); 50 vol.% ethanol / 50 vol.% water (c);90 vol.% ethanol / 10 vol.% water (d); ethanol (e).*

7.3.3. Effect of reducing / oxidative properties of sonication media

To further investigate how reducing / oxidative properties of sonication media affect the composition of the surface of the AlNi alloy particles, we examined XPS spectra for all samples (**Fig. 7.4(a-f)**). **Table 7.2** summarizes the surface compositional content of initial and modified alloy particles. Interestingly, the AlO_x content decreases as we move from pure water to pure ethanol inversely proportional to electrochemical performance of these samples. Thus, a decrease in AlO_x amount on the surface of the electrocatalyst improves its performance toward HER. In addition, we observed reduction of AlO_x to Al (**Fig. 7.4b**), as well as reduction of NiO_x to Ni (**Fig. 7.4e**) upon sonication of AlNi alloy particles in ethanol, which is known as s reducing agent. The concept of metal reduction during US treatment confirms previously reported data where reducing radicals generated during acoustic cavitation have been used to synthesize metal

nanoparticles [29]. We believe this is another possible reason that explains more efficient electrocatalytic performance toward HER.
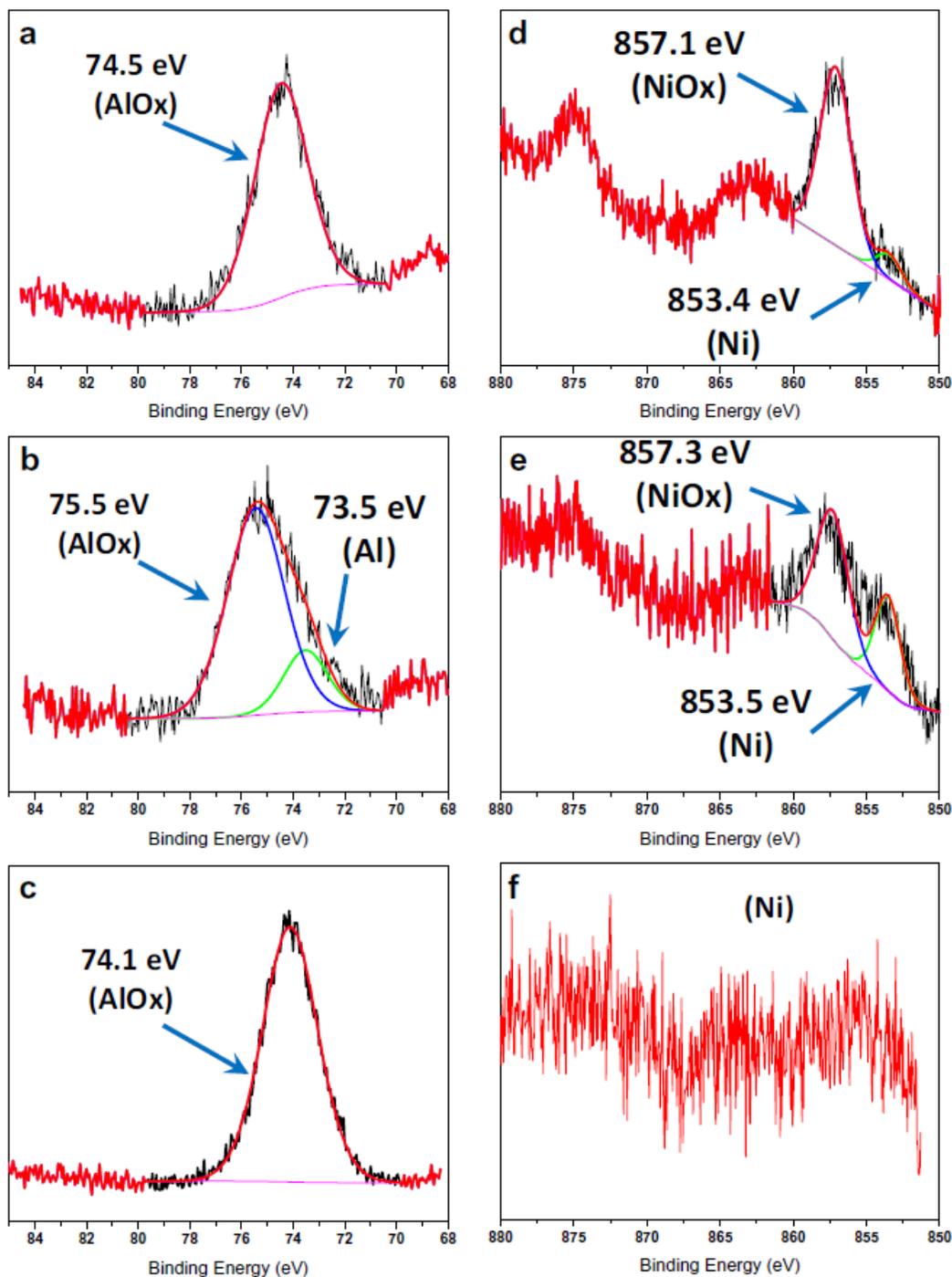
Figure 7.4: *The Ni 2p and Al 2p XPS spectra for the initial (a,d), HIUS treated in ethanol (b,e), and HIUS treated in water (c,f) AlNi (50 wt.% Ni) alloy particles.*

7.3.4. Effect of vapor pressure of sonication medium

Considering the above discussion on the effect of acoustic cavitation on the composition and morphology of HIUS treated AlNi alloy particles, it can be suggested that the effect strongly depends on the nature of the sonication medium. In particular, we believe that vapor pressure of the sonication medium plays a key role in controlling the overall effect. It has been reported that a higher cavitation bubble temperature is obtained in low vapor pressure liquids [28]. This can be understood from Equation 1 [30] and experimental data observed in the literature [31]. Equation 1, where T_0 is the ambient solution temperature, P_m is the pressure in the liquid (a sum the hydrostatic and acoustic pressures) $\gamma = c_p/c_v$ is the specific heat ratio of the gas-vapor mixture, and P_v is the pressure in the bubble at its maximum size, allows to calculate the maximum theoretical temperature within the bubble (T_{max}). A higher vapor pressure means weaker bubble collapse leading to a lower bubble temperature. In addition to increasing the pressure inside the bubble, the presence of a higher amount of solvent vapor would lead to the consumption of heat energy generated during bubble collapse. Both of these effects would lower the bubble temperature. In addition, a higher pressure inside the bubble would cushion the collapse of the bubble, resulting in lower collapse intensity and hence the associated physical effects (shear forces, microjet, etc.) would be weaker.

$$T_{max} = T_0 \left\{ \frac{P_m(\gamma - 1)}{P_v} \right\} \quad (1)$$

Temperature impact on AlNi particles during US treatment will be stronger in water than in ethanol. In addition, in water, the physical forces would be stronger. Thus, effect of cavitation in water results in a higher surface area of AlNi alloy particles and favors oxidation processes to occur, which, overall, is negatively affecting electrocatalytic properties. Also, oxidizing radicals are produced in water. Replacing water with high vapor pressure sonication medium such as ethanol allows reducing cavitation impact on high surface area development as well as favors beneficial for electrocatalyst surface metal reduction processes.

7.4   Conclusions

We have shown that the choice of a suitable sonication medium for high intensity US treatment of AlNi alloy particles is crucial for their application in electrocatalytic water splitting. While the use of water as a sonication medium allows creating efficient hydrogenation catalyst, switching to pure ethanol enables HIUS activation of the same AlNi alloy particles toward electrocatalytic HER with significantly improved electrocatalytic properties: reduced overpotential and improved exchange current density values. In particular, it has been shown that HIUS treatment in ethanol results in almost 146-fold increase in i_0 value compared to untreated alloy particles. In addition, we have provided fundamental information about effect of cavitation on metal alloy's surface composition and redox processes that occur during ultrasound treatment. In this work we mainly focused on the solutions with reducing / oxidative properties for HIUS treatment of AlNi alloy particles, although, the true effect of sonication media is rather complex and needs to be investigated further, for example, in terms of other physical properties.

Acknowledgments

References

[1] S. Dunn, Hydrogen futures: toward a sustainable energy system, Int. J. Hydrog. Energy, 27 (2002) 235-264.

[2] N. Armaroli, V. Balzani, The future of energy supply: Challenges and opportunities, Angew. Chem.-Int. Edit., 46 (2007) 52-66.

[3] L. Barreto, A. Makihira, K. Riahi, The hydrogen economy in the 21st century: a sustainable development scenario, Int. J. Hydrog. Energy, 28 (2003) 267-284.

[4] K.D. Kreuer, On the development of proton conducting polymer membranes for hydrogen and methanol fuel cells, J. Membr. Sci., 185 (2001) 29-39.

[5] T. Rostrup-Nielsen, Manufacture of hydrogen, Catal. Today, 106 (2005) 293-296.

[6] A. Klerke, C.H. Christensen, J.K. Norskov, T. Vegge, Ammonia for hydrogen storage: challenges and opportunities, J. Mater. Chem., 18 (2008) 2304-2310.

[7] J.D. Holladay, J. Hu, D.L. King, Y. Wang, An overview of hydrogen production technologies, Catal. Today, 139 (2009) 244-260.

[8] M. Carmo, D.L. Fritz, J. Merge, D. Stolten, A comprehensive review on PEM water electrolysis, Int. J. Hydrog. Energy, 38 (2013) 4901-4934.

[9] J.M. Ogden, Prospects for building a hydrogen energy infrastructure, Annu. Rev. Energ. Environ., 24 (1999) 227-279.

[10] B.E. Conway, B.V. Tilak, Interfacial processes involving electrocatalytic evolution and oxidation of H-2, and the role of chemisorbed H, Electrochim. Acta, 47 (2002) 3571-3594.

[11] W.C. Sheng, H.A. Gasteiger, Y. Shao-Horn, Hydrogen Oxidation and Evolution Reaction Kinetics on Platinum: Acid vs Alkaline Electrolytes, J. Electrochem. Soc., 157 (2010) B1529-B1536.

[12] J. Greeley, T.F. Jaramillo, J. Bonde, I.B. Chorkendorff, J.K. Norskov, Computational high-throughput screening of electrocatalytic materials for hydrogen evolution, Nat. Mater., 5 (2006) 909-913.

[13] F. Harnisch, G. Sievers, U. Schroder, Tungsten carbide as electrocatalyst for the hydrogen evolution reaction in pH neutral electrolyte solutions, Appl. Catal. B-Environ., 89 (2009) 455-458.

[14] B. Hinnemann, P.G. Moses, J. Bonde, K.P. Jorgensen, J.H. Nielsen, S. Horch, I. Chorkendorff, J.K. Norskov, Biornimetic hydrogen evolution: MoS2 nanoparticles as catalyst for hydrogen evolution, J. Am. Chem. Soc., 127 (2005) 5308-5309.

[15] P.C. Chen, Y.M. Chang, P.W. Wu, Y.F. Chiu, Fabrication of Ni nanowires for hydrogen evolution reaction in a neutral electrolyte, Int. J. Hydrog. Energy, 34 (2009) 6596-6602.

[16] H.X. Dong, T. Lei, Y.H. He, N.P. Xu, B.Y. Huang, C.T. Liu, Electrochemical performance of porous Ni3Al electrodes for hydrogen evolution reaction, Int. J. Hydrog. Energy, 36 (2011) 12112-12120.

[17] P. Los, A. Rami, A. Lasia, Hydrogen evolution reaction on Ni-Al electrodes, J. Appl. Electrochem., 23 (1993) 135-140.

[18] A. Rami, A. Lasia, Kinetics of hydrogen evolution on Ni-Al alloy electrodes, J. Appl. Electrochem., 22 (1992) 376-382.

[19] D. Miousse, A. Lasia, V. Borck, Hydrogen evolution reaction on Ni-Al-Mo and Ni-Al electrodes prepared by low-pressure plasma spraying, J. Appl. Electrochem., 25 (1995) 592-602.

[20] J. Dulle, S. Nemeth, E.V. Skorb, T. Irrgang, J. Senker, R. Kempe, A. Fery, D.V. Andreeva, Sonochemical Activation of Al/Ni Hydrogenation Catalyst, Adv. Funct. Mater., 22 (2012) 3128-3135.

[21] J. Schaferhans, S. Gomez-Quero, D.V. Andreeva, G. Rothenberg, Novel and Effective Copper-Aluminum Propane Dehydrogenation Catalysts, Chem.-Eur. J., 17 (2011) 12254-12256.

[22] E.V. Skorb, H. Mohwald, T. Irrgang, A. Fery, D.V. Andreeva, Ultrasound-assisted design of metal nanocomposites, Chem. Commun., 46 (2010) 7897-7899.

[23] S.J. Doktycz, K.S. Suslick, Interparticle collisions driven by ultrasound, Science, 247 (1990) 1067-1069.

[24] N. Pazos-Perez, J. Schaferhans, E.V. Skorb, A. Fery, D.V. Andreeva, Ultrasound driven formation of metal-supported nanocatalysts, Microporous Mesoporous Mat., 154 (2012) 164-169.

[25] P.V. Cherepanov, I. Melnyk, D.V. Andreeva, Effect of high intensity ultrasound on Al_3Ni_2, Al_3Ni crystallite size in binary AlNi (50 wt.% of Ni) alloy, Ultrasonics Sonochemistry, 10.1016/j.ultsonch.2014.07.022 (2014).

[26] J.W. Phillis, A.Y. Estevez, M.H. O'Regan, Protective effects of the free radical scavengers, dimethyl sulfoxide and ethanol, in cerebral ischemia in gerbils, Neurosci. Lett., 244 (1998) 109-111.

[27] E. Ciawi, J. Rae, M. Ashokkumar, F. Grieser, Determination of temperatures within acoustically generated bubbles in aqueous solutions at different ultrasound frequencies, J. Phys. Chem. B, 110 (2006) 13656-13660.

[28] J. Rae, M. Ashokkumar, O. Eulaerts, C. von Sonntag, J. Reisse, F. Grieser, Estimation of ultrasound induced cavitation bubble temperatures in aqueous solutions, Ultrasonics Sonochemistry, 12 (2005) 325-329.

[29] M. Ashokkumar, Sonochemical synthesis of inorganic nanoparticles, in: P.D. Cozzoli (Ed.) Advanced Wet-Chemical Synthetic Approaches to Inorganic Nanostructures, Transworld Research Network, 2008, pp. 107-131.

[30] M. Ashokkumar, T. Mason, Sonochemistry, in: Kirk-Othmer Encylcopedia of Chemical Technology, John Wiley & Sons, 2007.

[31] R. Tronson, M. Ashokkumar, F. Grieser, Comparison of the effects of water-soluble solutes on multibubble sonoluminescence generated in aqueous solutions by 20-and 515-kHz pulsed ultrasound, J. Phys. Chem. B, 106 (2002) 11064-11068.

Acknowledgements

(Eidesstattliche) Versicherungen und Erklärungen

(§ 5 Nr. 4 PromO)

Hiermit erkläre ich, dass keine Tatsachen vorliegen, die mich nach den gesetzlichen Bestimmungen über die Führung akademischer Grade zur Führung eines Doktorgrades unwürdig erscheinen lassen.

(§ 8 S. 2 Nr. 5 PromO)

Hiermit erkläre ich mich damit einverstanden, dass die elektronische Fassung meiner Dissertation unter Wahrung meiner Urheberrechte und des Datenschutzes einer gesonderten Überprüfung hinsichtlich der eigenständigen Anfertigung der Dissertation unterzogen werden kann.

(§ 8 S. 2 Nr. 7 PromO)

Hiermit erkläre ich eidesstattlich, dass ich die Dissertation selbständig verfasst und keine anderen als die von mir angegebenen Quellen und Hilfsmittel benutzt habe.

(§ 8 S. 2 Nr. 8 PromO)

Ich habe die Dissertation nicht bereits zur Erlangung eines akademischen Grades anderweitig eingereicht und habe auch nicht bereits diese oder eine gleichartige Doktorprüfung endgültig nicht bestanden.

(§ 8 S. 2 Nr. 9 PromO)

Hiermit erkläre ich, dass ich keine Hilfe von gewerblichen Promotionsberatern bzw. -vermittlern in Anspruch genommen habe und auch künftig nicht nehmen werde.

…………………………………………………………………………………….
Ort, Datum, Unterschrift